PhD Thesis

Modeling and Development of a Biosensor Based on Optical Detection of the Rotational Dynamics of Hybrid Nanoparticles

Bielefeld University

AIT Austrian Institute of Technology

Stefan Schrittwieser

March 31, 2014

Declaration

I wrote this thesis by myself and used none but the indicated resources.

Vienna, March 31, 2014

Stefan Schrittwieser

Reviewers:

Univ.Prof. Dr. Andreas Hütten
Univ.Doz. Dr. Hubert Brückl

Date of submission: March 31, 2014

"Ever tried. Ever failed. No matter. Try again. Fail again. Fail better."

Samuel Beckett

Contents

List of Figures

1. Motivation

In the year 2012, an estimated number of 3.45 million incidences of cancer has been reported for Europe, with 1.75 million people have died from cancer. Herein, the most common type of cancer cases is female breast cancer with an incidence number of 464,000. Together with colorectal, lung and prostate cancer, breast cancer represents the majority of new cancer cases. Female breast cancer is the major burden of cancer concerning incidence among both overall diagnosed cancer cases (28.8 %) and mortality (16.8 %).[1]

It has been shown that mortality can be reduced by efficient breast cancer screening, so that diagnosis is crucial for a successful therapy.[2] State of the art technologies applied for breast cancer screening are imaging methods like mammography, ultrasound and magnetic resonance imaging. Diagnosis by imaging technologies depends on the size of the tumor, the experience of the professionals interpreting the obtained results and on the actual status of the patient's menstrual cycle.[2] Therefore, new innovative approaches that do not suffer from the above mentioned disadvantages have to be found to improve the current diagnostic methods. A suitable method to replace imaging technologies is the detection of cancer biomarkers in body fluids like serum, which enables a diagnosis at the very early stage of a malignant process development. Point-of-Care (POC) testing by fast, low cost and easy to use instruments can improve the screening process and is of interest for diagnosis as well as for treatment monitoring. Generally, the term "POC diagnostics" describes biomedical testing outside of clinical laboratories, which includes biosensing at the patient's home, at the doctor's office, in mobile laboratories and bed side monitoring. Thus, automated and robust analysis systems that display specific and sensitive results in a comprehensive format within a short time are required.[3]

Further prominent examples of POC testing applications are pregnancy, diabetes, sepsis, malaria, tuberculosis, and HIV.[3] For this purpose, immunoassays that detect a target molecule (antigen) through the use of an antibody are already widely used. While an assay is generally defined as the detection of an analyte substance, an immunoassay mimics the principle of the immune system to identify a target molecule through an interaction with an antibody. Among those, heterogeneous immunoassays have to be distinguished from homogeneous assay principles.

The enzyme-linked immunosorbent assay (ELISA) is a prominent representative of heterogeneous assays that are currently state of the art techniques used for immunodiagnostics. Although heterogeneous assays offer the advantage of low background, wide dynamic range, and high sensitivity,[4] the disadvantages (labor

intensive multiple incubation and washing cycles[5]) hinder the widespread use for POC testing.

For this reason, homogeneous immunoassays that use simple "mix and measure" techniques are advantageous and increase their applicability for POC testing. Here, the binding of an analyte to its respective partner molecule within the whole sample solution is used for signal generation.[6] Additionally, label-free assays that directly detect a change of the measurement signal upon analyte binding minimize the sample preparation procedure. Thus, in principle, homogeneous label-free assays circumvent the need of the numerous preliminary preparation steps usually done for heterogeneous assays, which allows to shorten or even entirely skip sample preparation procedures.[7] Due to the fast three-dimensional diffusion of the analyte molecules and the capture probes within the sample solution, faster transition to equilibrium can be accomplished compared to heterogeneous assays, which rely on a two-dimensional diffusion of the analyte to the capture surface. Moreover, heterogeneous assays suffer from the steric hindrance of analyte molecules binding to flat surfaces. In summary, it can be stated that homogeneous assays are more suitable for POC testing applications.

A biosensing method that combines the advantages of POC testing systems with the advantages of homogeneous label-free immunoassays is of great interest for the improvement of POC immunoassays in general, and for breast cancer screening in particular. In this thesis a novel measurement principle fulfilling these requirements will be presented.

2. Introduction

The fundamental principle of a homogeneous label-free immunoassay relies on the direct change of the measurement signal upon binding of analyte molecules to a probe. These binding events of target molecules change the physical properties of the probe.

The approach presented here for homogeneous real-time molecular detection is based on nanoparticles as probes, and the generated signal originates from changes of the hydrodynamic nanoparticle volume.[8–11] The latter describes the volume of a particle when immersed in a fluid. Functionalized nanoparticles, which will be denoted as nanoprobes in the following, are applied and excited in an external magnetic field. The measurement signal is generated by anisotropic excitations of the conduction electrons (plasmon resonances) within the nanoprobes without the need of an additional label. This technique is called "PlasMag" and requires multicomponent nanoparticles that combine both anisotropic magnetic and optical properties.

A particle type that would be suitable for the PlasMag measurement method comprises magnetic and optical structural components like an elongated core-shell structure with a magnetic core and a noble metal shell. While the magnetic core with fixed magnetic moment direction enables manipulation of the nanoprobe alignment by an external magnetic field, the noble metal shell allows optical detection of the actual nanoprobe orientation by light extinction or scattering measurements. Here, the orientation-dependent excitation of the longitudinal plasmon mode of the nanoparticle's anisotropic noble metal shell in polarized light is used. Liz-Marzán et al. demonstrated the orientation dependent extinction of bare gold (Au) nanorods.[12] The noble metal shell possesses different additional functionalities, i.e. a protection of the magnetic core against oxidation, and the possibility of serving as a substrate layer for further nanoparticle functionalization by specific antibodies against the target molecules

The measurement mode for applying the PlasMag method uses a rotating magnetic field for alignment control of the nanoparticles. Fig. 2.1 shows the rotating magnetic field measurement mode in a principal sketch. The signal of interest is the phase lag φ of the mean nanoprobe alignment with respect to the rotating magnetic field, which is a measure of the hydrodynamic drag of the nanoprobes in the sample solution. Binding events of analyte molecules result in an increase of the hydrodynamic nanoparticle volume and, hence, in an increased hydrodynamic drag that directly translates to an increased phase lag. The actual nanoprobe orientation is measured in transmission geometry by employing linearly polarized light and a photodetector that measures the intensity of the transmitted light por-

tion. The latter depends on the angle α between the direction of light polarization and the orientation of the long nanoparticle axis. Comparison of the actual magnetic field direction with the evolution of the angle α over time allows to directly monitor changes in the hydrodynamic drag that are displayed by an altered angle φ.[10,11]

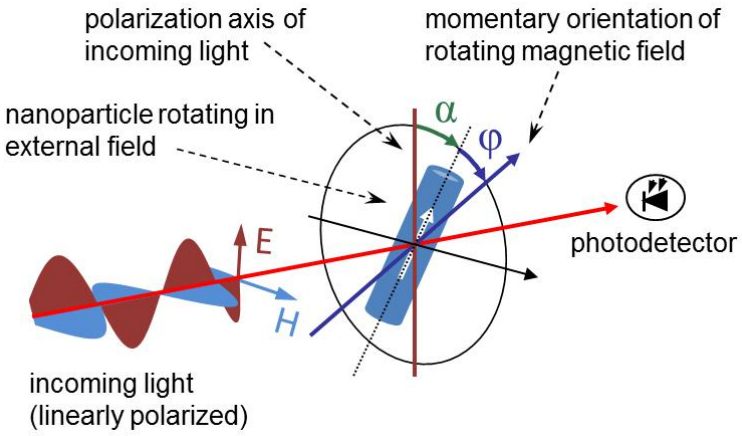

Figure 2.1.: Illustration of the PlasMag measurement principle applying a rotating magnetic field. The anisotropic magnetic nanoparticle follows the external rotating magnetic field but experiences a drag torque that results in a phase lag φ, which depends on the nanoparticle's hydrodynamic volume. By applying linearly polarized light, the detected transmission depends on the actual orientation of the nanoparticle with respect to the polarization direction, which is determined by the angle α. By comparing the momentary orientation of the rotating magnetic field to the measured transmission, the angle φ can be determined.[10,11]

The PlasMag concept has some advantages in comparison to methods based on similar concepts such as magnetorelaxation (MRX) or ac magnetometry-based assays.[13–15] Among those are, for example, the magnetic relaxation immunoassay (MARIA) or the immunomagnetic reduction assay (IMR).[16,17] Here, time-varying external magnetic fields are used in a comparable way to the PlasMag method for particle excitation. However, the signal detection is realized via magnetic methods by measuring the total magnetic field generated by the particles. As the magnetic field strength drops off rapidly with distance, relatively large concentrations of magnetic particles have to be employed as long as easy to handle magnetic sensor systems such as fluxgate senors are used.[13] Higher sensitivities beyond the nanomolar range can only be reached if more sophisticated and complex SQUID (superconducting quantum-interference device) based sensors are applied.[17] However, this sensor technology is not suitable for POC testing applications as it requires extensive cooling by liquid nitrogen.

Another example for a comparable measurement method is the magneto-optical

relaxation of ferrofluids (MORFF), which is based on relaxation measurements by using the Cotton-Mouton effect of magnetic nanoparticles.[18,19] The MORFF technique uses a separation of the magnetic excitation signal from the optical detection signal comparable to the PlasMag principle, but suffers from the low magnitude of the Cotton-Mouton effect, which results again in the need for high nanoparticle concentrations in the nanomolar range.[18] Consequently, the achievable sensitivities are lowered.

The group of Menno Prins at the Eindhoven University of Technology uses an approach similar to PlasMag comprising a magnetic excitation in an external rotating magnetic field and optical detection of magnetic particle rotation.[20] In contrast to PlasMag, which requires elongated particles, their system is based on spherical particles which are linked together by analyte molecules. Thus, particle chains are formed which induce the required optical anisotropy. However, this method is restricted to analyte molecules with at least two binding sites.

Methods that employ the plasmon resonance behavior of noble metal nanoparticles alone use two different ways of signal generation. Either the spectral shift caused by the specific adhesion of analyte molecules onto the noble metal is detected, or the spectral shift originating from a particle agglomeration caused by analyte molecules is measured.[21,22] In order to detect the small magnitude of the spectral shift, a complex instrumentation is required, and therefore, the applicability for POC measurements is reduced.

As mentioned before, nanoparticles that combine both optical and magnetic anisotropic behavior are required for the PlasMag measurement method. At the beginning of the PlasMag project, bare cobalt (Co) nanorods dissolved in organic solvents have been available and were tested. These single-crystalline Co nanorods with a fixed diameter of approximately 6 nm and adjustable length are fabricated with precise shape and size control from organometallic precursors, and they serve as ideal core particles for the aspired core-shell nanorods. Here, the anisotropic polarizability of rod-shaped particles allows to employ even bare magnetic nanorods as probes for PlasMag measurements. Initial measurements with an external rotating magnetic field gave proof of the basic measurement principle of the PlasMag system (see chapter 5.4.1). However, due to the lack of a protective noble metal shell, these particles could not be transferred to aqueous solutions without being oxidized, which results in a loss of the required magnetic behavior.

Intermediate particles have been used as a second step to bridge the unavailability of noble metal shell coated nanorods. Nickel (Ni) nanorods synthesized by electrochemical methods have been used. These nanorods offer the advantage of being dispersable in aqueous media. The Ni nanorods have been used to show that binding of target molecules alters the measurement signal and that the phase lag increases as predicted by theory. Unspecific protein binding using bovine serum albumin (BSA) has been shown, and the amount of bound protein has been validated by alternative measurement methods (see chapter 5.4.2).

New fabrication procedures enabled the synthesis of Co core particles with a Pt/Au noble metal shell that successfully protects the core from being oxidized.

Subsequently, particle transfer from organic solvents to aqueous media is made possible. Together with a particle dispersion stabilization technique that makes use of an amphiphilic polymer, these nanorods can be stabilized and functionalized in aqueous buffer solutions. With these nanoprobes biotin-streptavidin model binding assays have been realized to give a first proof of specific binding detection. For the final proof of principle, nanoprobes with antibody functionalization have been prepared in order to carry out measurements to detect a breast cancer biomarker (see chapter 5.4.3).

The cancer biomarker of choice is the HER2 (human epidermal growth factor receptor 2) protein, which is a protein belonging to the epidermal growth factor receptor family that has the function of controlling cell growth and division.[23] In case of breast cancer, approximately 25% of the patients show elevated levels of the HER2 protein, which is due to an overexpression of the associated HER2 gene.[24] HER2 is a cell transmembrane protein consisting of a part anchored to the cell membrane and an extracellular domain that can be released from the rest and shed into the blood stream, which results in soluble HER2 protein fragments that can be detected in serum (sHER2).[23] Fig. 2.2 shows a healthy cell with normal levels of the HER2 gene expression, and a cancer cell with overexpression of the HER2 gene, which results in overproduction of the HER2 protein and fastens cancer cell growth. The clinically relevant cutoff concentration is around 15 ng/ml (or approximately 140 pM with an average molecular weight of sHER2 of 105 kDa).[23,25] Siemens already offers an instrument that measures serum levels of sHER2, the ADVIA Centaur, that uses two antibodies in a sandwich type immunoassay and the chemiluminescence technique for the measurement.[26] This instrument is designed for a broad range scanning of multiple biomarkers including markers for breast cancer, infectious disease, cardiovascular disease, etc. Due to its large size, the instrument is not applicable for POC testing.

Generally, the PlasMag biosensing method is not restricted to breast cancer but can be applied to any disease that can be correlated to concentration changes of a biomarker as long as a specific partner molecule for binding is known. Therefore, the sensor principle offers a wide range of applications. Compared to already existing methods, it combines the advantages of being sensitive, easy to handle and fast. Thus, it is well suited for POC testing applications.

In this thesis, an overview of the fundamental principles of the PlasMag biosensing platform and an experimental proof of principle are presented. The intention of this study is to provide a foundation of the basic principles that are used for executing, understanding and interpreting the obtained measurement results as well as initial measurements demonstrating the potential of the PlasMag system for biosensing. First, the general applicability of the PlasMag technique for biosensing will be introduced and second, an experimental validation for the measurement of the rotational behavior of anisotropic hybrid nanoparticles will be presented, which made possible the detection of a specific breast cancer biomarker.

A basic introduction into the measurement principle and a comparison to established similar methods has been given within this chapter. Theoretical con-

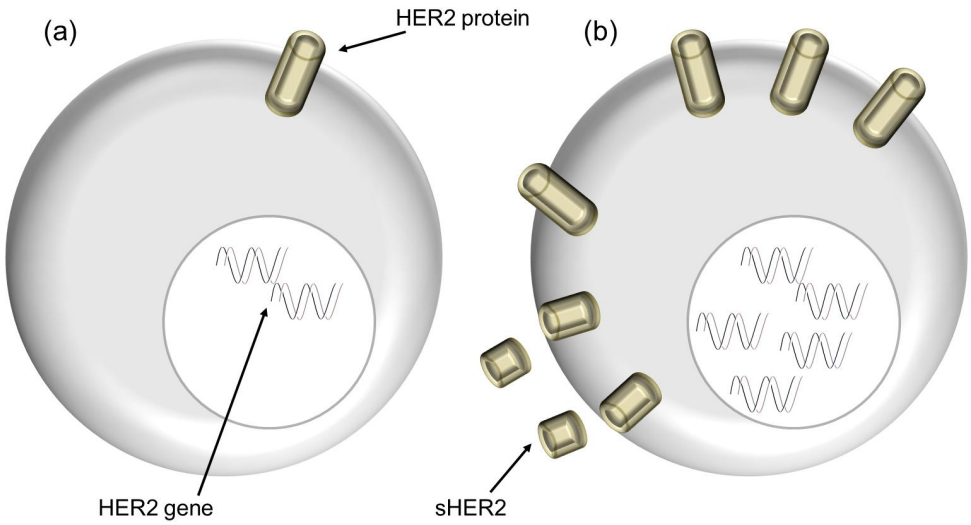

Figure 2.2.: Her2 expression of healthy cells (a) and of cancer cells (b). The HER2 gene is overexpressed in cancer cells, which leads to an increased number of associated HER2 transmembrane proteins. The extracellular domain of the HER2 protein can be released from the cell membrane and shed into the blood stream (sHER2).

siderations on fundamental nanoparticle characteristics used to understand the measurement principle and experimental results are discussed in chapter 3.

The experimental setup is presented in detail in chapter 4. Next, in chapter 5, the obtained results are discussed. The results of both the theoretical considerations and the experimental measurements are shown there. This involves simulation and modeling of the expected measurement signal as well as measurements with the proposed sensing principle. Starting from a first proof of principle, the measurement method is validated and improved step by step. Finally, the successful detection of a breast cancer biomarker is presented.

The thesis is concluded by an outlook on future possibilities for the further optimization and development of the measurement method.

3. Fundamentals

The National Nanotechnology Initiative of the United States of America defines nanotechnology as: "*Nanotechnology is not simply working at ever smaller dimensions; rather, working at the nanoscale enables scientists to utilize the unique physical, chemical, mechanical, and optical properties of materials that naturally occur at that scale*". Moreover, the nanoscale is the "*scale at which much of biology occurs*" and "*at which surfaces and interfaces play a large role in materials properties and interactions*".[27]

One of the most prominent characteristics at the nanoscale is the surface to volume ratio of a nanoparticle, which increases with decreasing particle size. In case of Au nanoparticles with a given unit cell parameter and given crystal structure, the ratio of surface to volume atoms of spherical (black line) and cylindrical (red line) particles in dependence of the particle diameter is shown in Fig. 3.1. By neglecting the end caps of the cylinder, the ratio gets independent of the cylinder length. By considering the end caps of the cylinder, the obtained surface to volume ratio of cylinders stays below the one of spheres as long as the diameter does not exceed the length of the nanoparticle. Generally, spherical particles have an increased surface to volume ratio compared to cylindrical particles.[28–30]

In the following chapters, the main properties of particles at the nanoscale are discussed to the extent as they are of importance for this thesis. This includes the magnetic, optical and hydrodynamic behavior of nanoparticles. Moreover, each chapter on specific nanoparticle characteristics is commented on its ability for biomedical applications with a focus on sensing techniques.

3.1. Magnetic Nanoparticles

3.1.1. Properties of Magnetic Nanoparticles

Magnetic Properties

Different properties of bulk magnetic matter are defined via the specific material they are composed of, the crystal structure, environmental parameters like temperature or applied magnetic fields and even the history of applied external conditions. In the nanometer regime new magnetic properties occur due to the size and the shape of the magnetic nanoparticles. The most relevant properties of magnetic nanoparticles used for biosensing applications and for the experiments in the present work, are discussed in the following paragraphs.

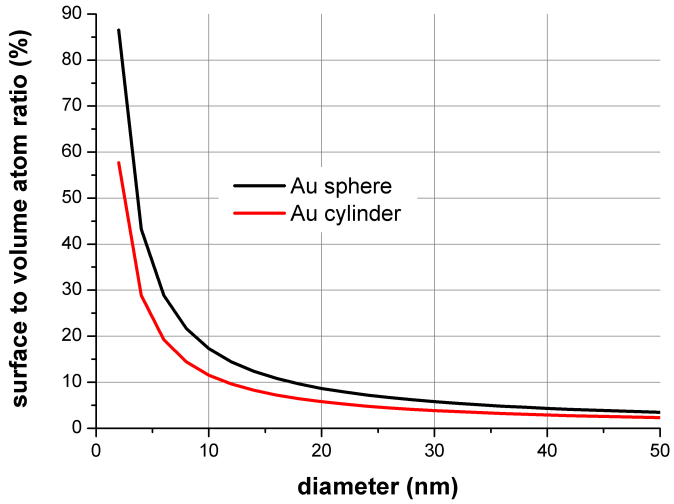

Figure 3.1.: Percentage of surface to volume atoms for Au spheres (black) and cylinders (red) in dependence of the diameter. Here, the end caps of the cylinder are not considered.

As soon as there is at least one dimension of the magnetic material in the nanometer range, new magnetic properties appear. These are for example superparamagnetism, remanence enhancement, the giant magnetoresistance or ferromagnetism of superconducting nanoparticles.[31,32]

In general, magnetic nanoparticles can be divided into single-domain and multi-domain particles (see Fig. 3.2 for the dependence of the intrinsic coercivity on the particle diameter). Above a certain critical size, magnetic nanoparticles build up different magnetic domains, which is caused by a minimization of magnetostatic energy.[33] Below this size limit, nanoparticles exist in a single-domain state.[31,33] Single-domain particles possess a saturated magnetization state with a distinct magnetization direction, whereas multi-domain nanoparticles possess a magnetization below its saturation value and multiple disordered domain magnetization directions.[33] The latter can be brought to their saturated magnetization state by an external applied magnetic field larger than the demagnetizing field.[33] The coercivity value reaches a maximum at the critical size limit between single-domain and multi-domain particles and is reduced with increasing as well as with decreasing particle size.[31,33] By further decreasing the particle size of a single-domain particle below another critical value, superparamagnetism occurs.[33] In this superparamagnetic state, the thermal energy exceeds the energy barrier for magnetic reversal and, therefore, reverses the magnetization direction of the particle, which leads to spontaneous fluctuations (flips) in the magnetization direction.[31,33,34] The coercivity in this size regime is zero and no hysteresis occurs in the magnetization curve of such an ensemble of particles.[34] Below a certain temperature which is

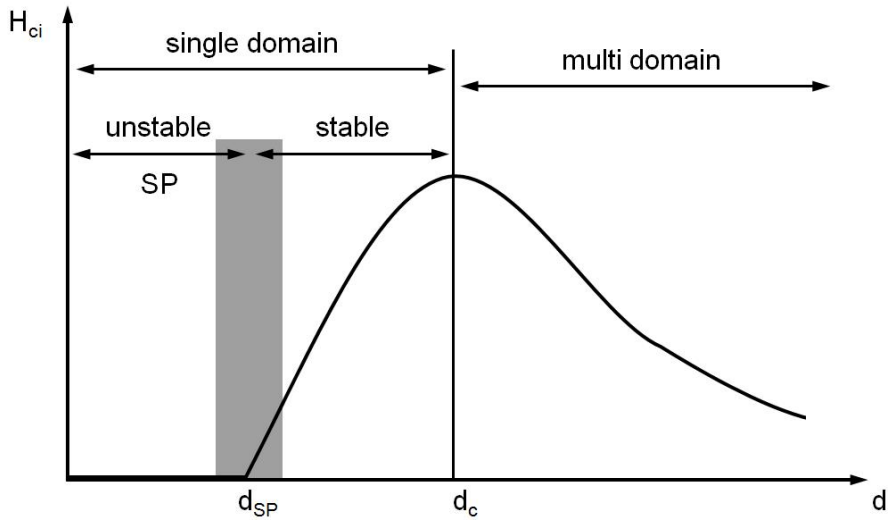

Figure 3.2.: Dependence of the intrinsic coercivity H_{ci} on the nanoparticle diameter d. The critical diameter d_c separates the multi-domain state from the single-domain one. Single domain particles can be further divided into particles possessing a stable or an unstable magnetization direction. Particles with unstable magnetization directions are called superparamagnetic (SP) nanoparticles with a diameter corresponding to this transition called d_{SP}. The transition between the different regimes is not sharp and depends on the measurement methods.[33]

called the blocking temperature, superparamagnetic particles exhibit stable magnetization again.[31,33]

The magnetization of a small magnetic nanoparticle is in a ferromagnetic state below its blocking temperature, in a superparamagnetic state between its blocking temperature and the Curie temperature and in a paramagnetic state above its Curie temperature.[31] This is illustrated in Fig. 3.3.

The inverse flipping frequency of the magnetization is called Néel relaxation time and can be expressed in the absence of external fields as

$$\tau_N = \tau_0 \cdot exp\left(\frac{K \cdot V}{k_B \cdot T}\right), \tag{3.1}$$

where τ_0 is usually taken as 10^{-9} s, V is the particle volume, K the magnetic anisotropy constant of the particle, k_B the Boltzmann constant and T the temperature.[31] No general absolute value for the Néel relaxation time exists defining whether a magnetization is stable or not. Instead it is considered to be stable if τ_N is in the range of time which is needed to execute magnetic measurements.[31,34]

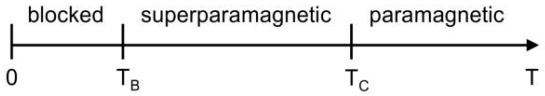

Figure 3.3.: Temperature dependence of the magnetization state of superparamagnetic particles. These small ferromagnetic nanoparticles show stable, blocked magnetization when cooled down below the blocking temperature T_B and behave paramagnetic when heated up above the Curie temperature T_C.[31]

The particles used in this work are all ferromagnetic and single-domain, i.e. they show permanent magnetization fixed in one distinct direction (for elongated particles this is normally the direction of the long particle axis due to the shape anisotropy and crystal structure of the involved materials).

Colloidal Stability

An important aspect for magnetic particles in general and especially for ferromagnetic particles is colloidal stability in solution. The interparticle forces which have to be considered here are magnetic interactions, van der Waals forces and, due to the possible presence of electric charges on the surfaces of the nanoparticles, electrostatic interactions. Generally, a particle suspension is considered to be stable if the sum of all positive (particle attracting) and negative (particle repelling) interactions is smaller than the thermal energy.[35,36]

The most sensitive task in stabilization of magnetic nanoparticles in suspension is to overcome attracting magnetic interactions. The attracting magnetic forces between two nanoparticles originate mainly from dipole-dipole interactions. In case of cylindrical particles two different geometric configurations can be found.

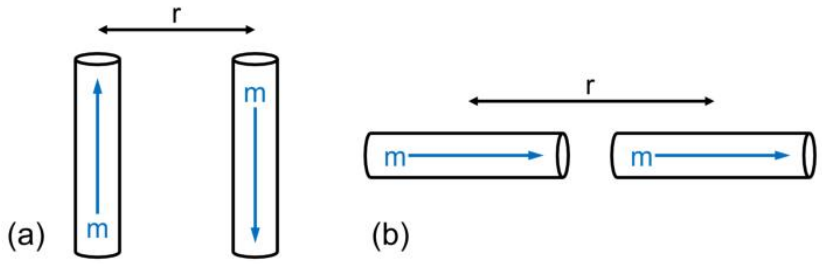

Figure 3.4.: Possible nanorod alignments in case of cylindrical particles with fixed magnetization directions (m) acting as magnetic dipoles at a distance of r. (a) Preferred parallel nanorod alignment with magnetization directions antiparallel to each other due to a minimization of dipole-dipole energy. (b) Tip-to-end nanorod configuration with magnetizations pointing in the same direction.[35]

Fig. 3.4(a) shows a parallel configuration of two nanorods with magnetization directions antiparallel to each other and in Fig. 3.4(b), a configuration with the two particles aligned tip-to-end with magnetization pointing in the same direction.[35] The dipole-dipole energy of the parallel configuration is smaller than the one for the tip-to-end configuration and is, therefore, preferred during agglomeration.[35] In case of nanorods with the same absolute value of the magnetic moment and antiparallel configuration, the dipole-dipole energy amounts to

$$U_{dd} = -\frac{m^2 \cdot \mu_0}{4 \cdot \pi \cdot r^3}, \tag{3.2}$$

where μ_0 is the magnetic permeability and r is the distance between the two nanorods.[35]

For particle dispersions in solution, a method to overcome the attracting magnetic dipole-dipole interaction is the stabilization with electrostatic forces. Particles with the same sign of electrical charge repel each other. The origin of the surface charge can be attributed to attached charged groups or a naturally developed charged surface in a distinct medium.[37] For some particles used in this work, the latter case occurs due to oxidation of the metal nanoparticles and their subsequent hydroxylation in aqueous media.[37–39] Metal oxides behave amphoteric depending on whether the involved oxide behaves acidic or basic, which means that the surface charge depends on the pH value (see equ. 3.3).[39] In media with a high pH value the OH groups on the particle surface hydrolyze and the metal surface gets negatively charged.[37] Protonation happens in acidic media, so that OH_2^+ groups are created and the particle surface gets positively charged.[37] The concentration of ions in the surrounding media corresponding to a neutral surface charge of the nanoparticles is called point of zero charge.[37]

$$MOH_2^+ \xleftarrow{H^+} MOH \xrightarrow{OH^-} M(OH)_2^- \; = (MO^- + H_2O) \tag{3.3}$$

Once particles possess a surface charge density, an electrical double layer is created, which consists of counterions that balance the charge of the particle in solution near the surface (see Fig. 3.5).[38] The first layer (Stern layer) consists of counterions that have the opposite charge of the particle and is strongly fixed to the surface.[37,38] The potential at the end of the Stern layer is consistently called Stern potential and drops linearly with distance from the particle surface.[38] Around this first layer, a second layer of ions is present, the diffuse layer, which consists of fixed and weakly bound ions.[37,38] The potential associated with this layer U_{DL} drops exponentially with distance d and with the characteristic Debye-Hückel parameter κ:[37,38]

$$U_{DL}(d) = e^{-\kappa d}. \tag{3.4}$$

The inverse of κ, called Debye-Hückel length or Debye length, as it will be denoted in the rest of this work, is given by

$$\kappa^{-1} = \left(\frac{e_0^2}{\epsilon_r \cdot \epsilon_0 \cdot k_B \cdot T} \cdot \sum_i c_i \cdot z_i^2 \right)^{-\frac{1}{2}}, \tag{3.5}$$

where e_0 is the elementary charge, ϵ_r the relative permittivity of the medium, ϵ_0 the vacuum permittivity, k_B the Boltzmann constant, T the temperature, z_i the charge number and c_i the concentration of the charged species.[37] The sum in equation 3.5 is correlated to the ionic strength IS:[37]

$$IS = \frac{1}{2} \cdot \sum_i c_i \cdot z_i^2. \tag{3.6}$$

The zeta potential occurring at the slip plane (or surface of shear) is considered to arise near the particle surface and to contain stationary, immobile fluid which is bound to the particle when it moves.[37] The thickness of the electrical double layer (and consequently the Debye length) determines the range of electrostatic interaction between two particles in general electrolytes.[37] Electrostatic interaction strength between charged particles is determined by the surface charges which are attenuated by the electrical double layers.[38] In case of given ionic strength, the charge of the particle surface describes the electrostatic interaction.

Another force is the van der Waals interaction which has its origin in the polarization of electron clouds of two nuclei interacting with each other and acts solely on a very short range due to the strong distance dependence of r^{-6}.[38,40]

Three different forms of van der Waals interaction can be distinguished. The first one is the Keesom interaction which is the force between two permanent dipoles. The second one is the Debye force, which is the interaction of a permanent dipole with an induced one and the third one, the main component of van der Waals interaction, the London force between two polarizable molecules that is caused by spontaneous oscillations of electron clouds which induce temporary dipoles.[41] Van der Waals interaction is mostly an attractive force and proportional

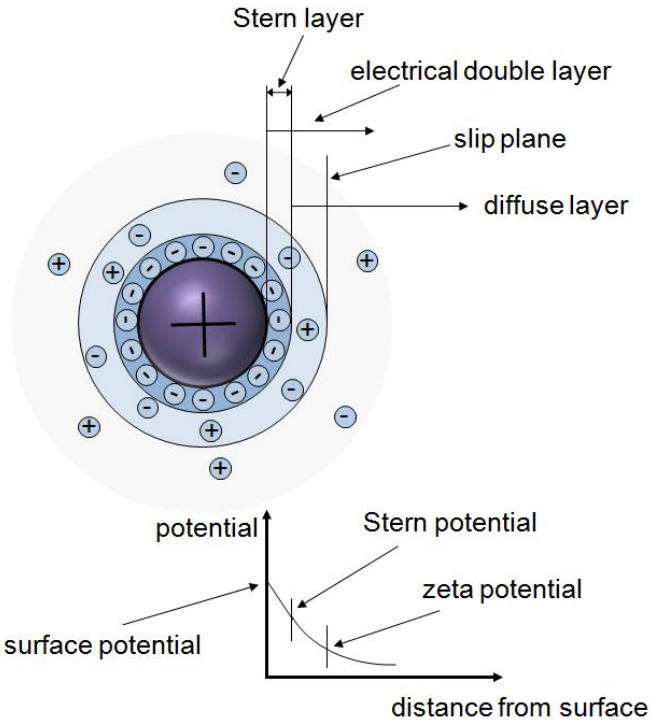

Figure 3.5.: Electrical double layer and potentials of a nanoparticle with positive surface charge. The first layer on the particle surface is the Stern layer with strongly fixed counterions while the second layer with fixed and weakly bound ions of positive and negative charges is called the diffuse layer. The slip plane, separating bound immobile ions from weakly bound ones, determines the zeta potential. Generally, the potential first drops linearly from the surface potential down to the Stern potential and then behaves exponentially with increasing distance from the particle surface.[38,39]

to the surface area of contact.[40] Due to its short range, it can be overcome with the help of steric hindrance.[38]

Steric stabilization of colloids is defined as the binding (adsorption or grafting) of non-ionic molecules to the particle surface and is mostly achieved by large molecules (e.g. polymers) attached to the surface of the nanoparticles, thus, preventing two particles from getting into close contact.[38,42] While electrostatic stabilization is mostly restricted to dilute particle dispersions and sensitive to electrolytes, steric stabilization offers the advantage of being applicable to high particle concentrations and of not being sensitive to electrolyte solutions.[38] Furthermore, steric stabilization is a thermodynamic stabilization method (contrary to the electrostatic one which is based on kinetic stabilization) and offers, therefore, easy redispersion of once agglomerated particles.[38,42,43] In most synthesis methods, steric stabilizing agents are added during particle synthesis. Widely used examples of agents forming the steric stabilizing layer are dextran, polyvinyl alcohol or different block copolymers, e.g. acrylic acid and N-isopropylacrylamide.[44]

A combination of electrostatic and steric (electrosteric) stabilization of nanoparticles is another possible approach to increase stability in solution and has been shown, for example, by Lourenco et al.[38,45]

An alternative approach similar to steric stabilization is stabilization by depletion. Here, a non-ionic polymer is dissolved in the particle solution and prevents agglomeration via depletion of the polymer concentration between two particles when they are in close contact with each other, which is energetically not preferred.[46]

Electrostatic repulsion and van der Waals interaction are combined to describe the stability of a dispersion within the DLVO theory (developed by Derjaguin, Landau, Verwey and Overbeek) which, despite its broad use, is limited due to the neglection of boundary conditions on the particle surface (i.e.: it assumes flat surfaces, uniform charge density with constant electric potential) and does not allow chemical reactions between the particles and the solvent.[35,38] The DLVO theory can be expanded by including steric and depletion interactions.[47]

Types of Synthesis

For the preparation of magnetic nanoparticles, a large variety of different synthesis approaches is available and reported in literature. Among them are coprecipitation, thermal decomposition of organometallic precursors, microemulsion, hydrothermal synthesis, physical condensation methods, sol-gel methods and electrochemical approaches.[48–51] Special attention has to be paid to the specific properties of magnetic nanoparticles used for biomedical applications, e.g. the ability to bind biologically and medically relevant molecules to the surface of the desired particles.[52,53] Furthermore, the surface modification of nanoparticles in biological applications has to enable particle dispersion in media of high salt concentration and at pH values near neutrality.[54] The synthesis routes of bare magnetic nanoparticles utilized for the measurements in the present work will be introduced

in the following.

In case of elongated magnetic nanoparticles, one of the most common synthesis routes is the template based approach. Pores in various templates like anodized alumina membranes, radiation track-etched polycarbonate or mica membranes and others are physically or chemically filled with the desired material leading to oriented or non-oriented nanowires and nanorods.[55,56] Magnetic materials that can be deposited in templates are Co, Ni, Fe and a wide variety of different alloys (e.g. Co-Pt, Cu-Fe, Fe-Ni or Ni-P).[57,58]

The thermal decomposition of organometallic precursors in high-boiling organic solvents containing stabilizing surfactants (e.g. oleic acid, trioctylphosphine oxide or hexadecylamine) is used to synthesize magnetic nanoparticles of Fe, Co and Ni.[48] It has been shown that the shape of magnetic nanocrystals can be influenced within this approach by adjusting temperature, pressure and time of synthesis leading to Ni or Co nanorods with the above mentioned stabilizing agents.[59–62]

3.1.2. Magnetic Nanoparticles in Biomedical Applications

Magnetic nanoparticles are already widely used in biomedical applications.[63–66] These particles are of special interest for magnetic resonance imaging,[67,68] drug delivery and targeting,[69] magnetic cell separation and tracking[70,71] and hyperthermia for cancer treatment.[72,73] Magnetic particle imaging relies on the nonlinearity of the magnetization curves of ferromagnetic nanoparticles in oscillating external magnetic fields and offers higher resolution in molecular imaging as it is provided now by magnetic resonance imaging.[74] Transfection of nucleic acids into cells, magnetofection, is another application of magnetic nanoparticles.[75] Biosensors, using magnetic nanoparticles to detect proteins, DNA, cancer cell markers and bacteria are other examples of biomedical applications of magnetic nanoparticles.[53,76–79] Magnetoresistive biosensors based on the giant, anisotropic or on the tunneling magnetoresistance effect utilizing magnetic nanoparticles as biomolecular labels promise high sensitivity using a versatile and low cost technology.[80,81]

Detecting the Brownian relaxation times of labeled magnetic nanoparticles is accomplished using magnetorelaxation[13] and ac magnetometry[14] based assays such as the magnetic relaxation immunoassay (MARIA)[16] or the immunomagnetic reduction assay (IMR).[17] Here, external magnetic fields are applied to excite the particles while their stray field is measured at a certain distance.

Magneto-optical effects can also be used for biomolecular detection, e.g. the magneto-optical relaxation of ferrofluids (MORFF).[16,18,82] Here, the magnetic nanoparticles are aligned in an external magnetic field perpendicular to the incident light path, which causes birefringence (Cotton-Mouton effect[83]). The relaxation of the nanoparticles can be measured by optically recording the birefringence after switching off the aligning magnetic field.[16,82]

3.2. Plasmonic Nanoparticles

3.2.1. General Introduction and Mie Theory

Colloidal solutions of small particles with sizes smaller than the wavelength of the incident light exhibit strong scattering properties and were first studied by Brücke (1852), Faraday (1857), Tyndall (from 1869 on) and Rayleigh (from 1871 on).[84] Mie described the colors of colloidal Au solutions by solving the Maxwell equations for light interacting with colloidal spherical metal particles and obtained an exact theory for the observed optical behavior.[84–86] Basically, by reducing the size of noble metal nanoparticles until the mean free path of the particle electrons gets smaller than the particle dimensions, strong extinction of incident light arises and induces coupling of the particles to the electromagnetic field of light.[87,88]

Plasmonics is defined as the study of light-matter interactions that occur if an electromagnetic field of light causes the conduction electrons of a nanostructure to collectively oscillate in this external field.[89] Two types of plasmons are known (see Fig. 3.6), namely the localized surface plasmon and the propagating surface plasmon (also called surface plasmon polariton).[89,90]

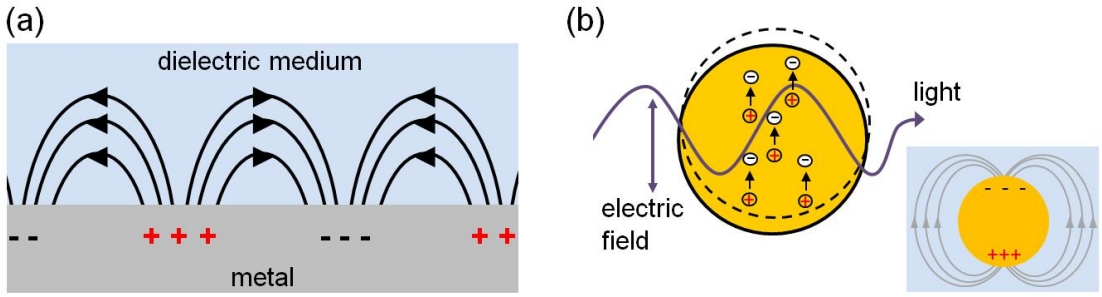

Figure 3.6.: Propagating (a) surface plasmon and localized (b) surface plasmon. The surface charge density is shown in both cases and indicated by the + and - signs. The electric field lines in (a) are curved to provide continuity of the field in the dielectric medium.[89,91] In (b), the electron cloud gets displaced under influence of the external electric field of incident light while the positive charges (atomic nuclei) are assumed to possess fixed positions, so that the particle gets polarized. The inset in (b) shows the surface charge density and the electrical field lines for the localized surface plasmon.[92]

Propagating surface plasmons are surface charge density waves propagating at a metal-dielectric interface and are, therefore, sensitive to changes in the surrounding dielectric medium, which obviously offers a biosensing applicability.[92,93] Here, plasmons propagate in the two dimensions parallel to the interface and decay exponentially in the direction perpendicular to the interface (evanescent wave).[89,91]

Localized surface plasmons are the collective oscillation of the free electrons in a metal nanoparticle caused by the electromagnetic waves of incident light.[94] As the

positive charges of the atomic cores are assumed to be fixed in their position and the negative charges of the conducting electrons are allowed to move inside the particle, the particle becomes polarized due to the displacement of the free electrons in an external electric field.[92,94] The displacement of the negative charges, which are enclosed in the geometric boundaries of the particle, causes a restoring force originating from the particle polarization. This results in the occurrence of resonant oscillations at distinct frequencies. For particles with anisotropic geometry, a specific plasmon resonance for every single axis is obtained (e.g. one transversal and one longitudinal plasmon resonance in case of a cylindrical particle shape).

The optical response of a spherical particle in a surrounding dielectric medium of dielectric constant ϵ_m to an electric field E_0 can be described by the polarizability α and the resulting electric dipole moment $p = \epsilon_m \alpha E_0$, where

$$\alpha = 4\pi R^3 \frac{\epsilon - \epsilon_m}{\epsilon + 2\epsilon_m}, \tag{3.7}$$

with the dielectric constant ϵ of the sphere of radius R (wavelength $\lambda \gg R$).[86,92,94] The condition $\lambda \gg R$ is needed for the assumption of the quasi-static regime, which means that retardation effects of the electromagnetic field across the particle diameter can be neglected with the result that only the time dependence but no spatial dependence of the field is kept.[94] Resonance behavior is then characterized by the condition $\epsilon + 2\epsilon_m = Minimum$ (a maximum of particle polarizability) which leads to

$$[\epsilon'(\omega) + 2\epsilon_m]^2 + [\epsilon''(\omega)]^2 = Minimum, \tag{3.8}$$

by assuming that ϵ_m is real and by splitting up the frequency dependent value of ϵ into its real ϵ' and imaginary part ϵ''.[94] If ϵ'' is small, it follows that

$$\epsilon' = -2\epsilon_m, \tag{3.9}$$

which means that the real part of the dielectric constant ϵ' possesses a negative value.[94]

By introducing the plasma frequency ω_p of the Drude model used to describe the optical response of free electrons as[94]

$$\epsilon' = 1 - \frac{\omega_p^2}{\omega^2}, \tag{3.10}$$

and by assuming vacuum in the surrounding with ϵ_m=1, it is found that the resonance frequency ω_{res} is defined as

$$\omega_{res} = \frac{\omega_p}{\sqrt{3}}, \tag{3.11}$$

which is known as the spherical dipolar surface plasmon frequency.[92,94] The Drude model is used to describe the macroscopic interaction of light with a metal under

the assumption of free movable electrons within the metal. These electrons directly react to an external force, i.e. an electric field. The response of a single electron to an external force is multiplied with the total number of free electrons. A result of the Drude model is the dielectric function given in equation 3.10. The parameters relevant for the plasmon resonance frequency are the shape, size, composition, orientation and dielectric environment of the nanostructure.[88–90,95,96] Localized surface plasmons are not only restricted to noble metals like silver and gold, but are also possible in a wide range of metals, alloys and semiconductors with a large negative real and a small imaginary dielectric constant value.[90]

The resonance behavior can also be illustrated by drawing the field lines of the energy flux density represented by the Poynting vector for a spherical metal particle at two different frequencies of planar wave excitation, schematically shown in Fig. 3.7. In Fig. 3.7(a) the frequency of the incident light is far off the resonance frequency of the nanoparticle and the energy flow is almost not affected, whereas in Fig. 3.7(b) the situation for light at the plasmon resonance frequency is shown, resulting in a strong convergence of field lines near the sphere, so that the absorption cross section is much higher than the geometrical cross section shown in Fig. 3.7(a).[86]

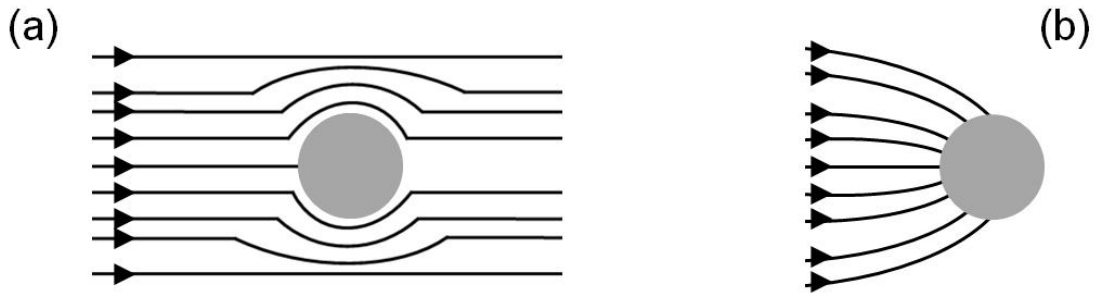

Figure 3.7.: Schematic illustration of the Poynting vector of a sphere given for two different frequencies of incident light. (a) The frequency of the incident light does not correspond to the plasmon resonance frequency and, thus, the energy flow is almost not affected and the absorption cross section is determined by the geometrical cross section. (b) In case of external light at the plasmon resonance frequency, the field lines strongly converge and an increased absorption cross section is obtained.[86]

The scattering and absorption cross sections of a nanoparticle, C_{sca} and C_{abs}, can be derived from the fraction of scattered and absorbed power to the incident power.[86,92] In general, the total scattered energy is equal to the incident energy falling on the area C_{sca} (the same is valid for the absorbed energy and C_{abs}).[84] For spherical particles, this is

$$C_{sca} = \frac{8\pi}{3} k^4 R^6 \left| \frac{\epsilon - \epsilon_m}{\epsilon + 2\epsilon_m} \right|^2 = \frac{k^4}{6\pi} |\alpha|^2 \tag{3.12}$$

and

$$C_{abs} = 4\pi k R^3 Im\left\{\frac{\epsilon - \epsilon_m}{\epsilon + 2\epsilon_m}\right\} = kIm\left\{\alpha\right\}, \tag{3.13}$$

with the particle radius R and the incident light wave vector magnitude $k = 2\pi/\lambda$.[86,92] The extinction is the sum of the power loss, thus, it is calculated as

$$C_{ext} = C_{sca} + C_{abs}. \tag{3.14}$$

For all cross sections, dimensionless efficiency factors can be defined together with the geometrical cross sections of the scattering object ($R^2\pi$ in case of spheres):

$$Q_{sca} = \frac{C_{sca}}{R^2\pi},\ Q_{abs} = \frac{C_{abs}}{R^2\pi}\ and\ Q_{ext} = \frac{C_{ext}}{R^2\pi}, \tag{3.15}$$

where $Q_{ext} = Q_{sca} + Q_{abs}$.[84,86]

The shape of the particle has a strong influence on the plasmon resonance, and the polarizability α gets anisotropic for geometries others than spheres. Therefore, α is a tensor defining different optical responses along different directions.[92] For an ellipsoidal particle, the polarizability for field directions in x, y and z in the quasi-static regime is

$$\alpha_{x,y,z} = \frac{4}{3}\pi L_x L_y L_z \frac{\epsilon - \epsilon_m}{\epsilon_m + P_{x,y,z}(\epsilon - \epsilon_m)}, \tag{3.16}$$

with the depolarization factors $P_{x,y,z}$ that determine the polarizability along the principal axes and L_x, L_y, L_z defining the semilengths of the ellipsoid.[86] The depolarization factors $P_{x,y,z}$ for an ellipsoid with rotational symmetry around the z-axis are defined via the eccentricity e:[92,94]

$$e = \sqrt{1 - \left(\frac{L_x}{L_z}\right)^2}, \tag{3.17}$$

$$P_z = \frac{1 - e^2}{e^2}\left[\frac{1}{2e}\ln\left(\frac{1+e}{1-e}\right) - 1\right], \tag{3.18}$$

$$P_x = P_y = \frac{1 - P_z}{2}. \tag{3.19}$$

For elongated particles, the optical properties in polarized light depend upon the orientation of the particle with respect to the direction of polarization. The anisotropic optical behavior can be shown by the polarizabilities along the main axes of the particle described by equation 3.16.

In the absence of a distinct direction towards the polarization, the random orientation of the elongated nanoparticles is given by the average polarizability

$$\langle\alpha_x\rangle = \frac{1}{3}\sum_i \alpha_i, \tag{3.20}$$

while in the presence of an orientation, the angle drawn between the polarization direction of light and the long particle axis θ has to be considered.[97] For an orientation with the long particle axis parallel to polarization, the polarizability is given by[97]

$$\alpha_{\parallel} = \cos^2\theta\alpha_1 + \left(1 - \cos^2\theta\right)\alpha_2, \tag{3.21}$$

and for perpendicular orientation

$$\alpha_{\perp} = \frac{1 - \cos^2\theta}{2}\alpha_1 + \frac{1 + \cos^2\theta}{2}\alpha_2. \tag{3.22}$$

In case of an ensemble of particles, the average polarizability for the two distinct orientations is given by

$$\langle\alpha_{\parallel}\rangle = \langle\cos^2\theta\rangle\alpha_1 + \left(1 - \langle\cos^2\theta\rangle\right)\alpha_2 \tag{3.23}$$

and

$$\langle\alpha_{\perp}\rangle = \frac{1 - \langle\cos^2\theta\rangle}{2}\alpha_1 + \frac{1 + \langle\cos^2\theta\rangle}{2}\alpha_2, \tag{3.24}$$

with $\langle\cos\theta\rangle$ as the average angle.[97]

Another more complex particle geometry is a core-shell structure. Here, the polarizability of a spherical core-shell particle in the quasi-static regime can be written in case of a single shell of thickness d and dielectric constant ϵ_S as

$$\alpha = 4\pi(R+d)^3\frac{(\epsilon_S - \epsilon_m)(\epsilon + 2\epsilon_S) + \left(\frac{R}{R+d}\right)^3(\epsilon - \epsilon_S)(\epsilon_m + 2\epsilon_S)}{(\epsilon_S + 2\epsilon_m)(\epsilon + 2\epsilon_S) + \left(\frac{R}{R+d}\right)^3(\epsilon - \epsilon_S)(2\epsilon_S - 2\epsilon_m)}, \tag{3.25}$$

with the dielectric constant of the core ϵ.[86]

An exact optical description of more complex particle geometries is difficult and, at a certain degree of complexity, even impossible. Therefore, numerical methods have to be used to obtain useful approximations of the optical behavior, which will be discussed in the frame of the present work in the following chapter.[88,89,92,95,96,98]

3.2.2. Discrete Dipole Approximation

Among the numerical methods used to describe the optical properties of complex particle geometries, the discrete dipole approximation (DDA) is reported to be one of the most useful computational methods and is used for the calculations in this work.[99–102] The basic ideas of the DDA have first been developed 1964-65 by DeVoe[103,104] and were later extended by Purcell and Pennypacker[100] reviewed in its principles by Draine.[105]

This method divides the particle into an array of N polarizable points in a cubic lattice, where the properties of these points depend on the dielectric function of the involved material.[101] For an incident electromagnetic wave, the scattering and absorption behavior is calculated based on the interaction of the incident

wave with the specific array of points, and on interactions between the formed dipoles.[99] The polarization vector of each element in the array is defined as

$$\vec{P}_i = \alpha_i \vec{E}_i, \tag{3.26}$$

with the polarizability α_i of each point and the local electric field $\vec{E}_i$ at the position $\vec{r}_i$.[105] The electric field is the sum of the incident field and the fields over all other polarizations given by

$$\vec{E}_i = \vec{E}_{inc,i} - \sum_{i \neq j} \vec{A}_{ij} \vec{P}_j, \tag{3.27}$$

with the incident electric field

$$\vec{E}_{inc,i} = \vec{E}_0 \exp\left(i\vec{k}\vec{r}_i - i\omega t\right), \tag{3.28}$$

depending on the wave vector $\vec{k}$ with $k = 2\pi n/\lambda$ in a surrounding dielectric medium of refractive index n.[105] $\vec{A}_{ij}\vec{P}_i$ is given by

$$\vec{A}_{ij}\vec{P}_i = \frac{exp(ikr)}{\vec{r}_{ij}^{\,3}} \left\{ k^2 \vec{r}_{ij} \times (r_{ij} \times P_j) + \frac{(1 - ik\vec{r}_{ij})}{\vec{r}_{ij}^{\,2}} \left[\vec{r}_{ij}^{\,2} \vec{P}_j - 3\vec{r}_{ij}(\vec{r}_{ij}\vec{P}_j) \right] \right\}, \tag{3.29}$$

as the electric field at the position $\vec{r}_i$.[105] The extinction and absorption cross sections are given by[105]

$$C_{ext} = \frac{4\pi k}{\mid E_0 \mid^2} \sum_{i=1}^{N} Im(\vec{E}^*_{inc,i}\vec{P}_i) \tag{3.30}$$

and

$$C_{abs} = \frac{4\pi k}{\mid E_0 \mid^2} \sum_{i=1}^{N} \left\{ Im\left[\vec{P}_i (\alpha_i^{-1})^* \vec{P}_i^* \right] - \frac{2}{3} k^3 \mid \vec{P}_i \mid^2 \right\}. \tag{3.31}$$

It has been shown that the DDA is a very useful method and yields accurate results for studying the optical properties of particles with arbitrary geometry.[53,99,106,107]

3.2.3. Plasmonic Nanoparticles in Biomedical Applications

Mainly, the wavelength shift of the plasmon resonance peak is used for the case of plasmonic nanoparticles in biomedical applications, which offers the possibility of label-free sensing. For example, plasmonic nanoparticles adhered to a surface can be used. Here, a shift of the plasmon resonance peak indicates a change of the dielectric environment surrounding the particle, which is the result of the binding of target molecules.[108,109] Biotinylated triangular silver nanoparticles on a glass slide have been used to detect streptavidin in the high femtomolar range.[110] The same group proposed the use of the mentioned silver triangles for the introduction of an Alzheimer's disease biosensor.[111] By using dark-field microscopy techniques,

the plasmon peak wavelength shift of single nanoparticles can be detected, and sensitivities down to the picomolar range can be achieved.[112,113]

Besides the adhesion onto a substrate and the detection of the plasmon peak shift due to changes in the dielectric environment, plasmonic nanoparticles in solution can be employed. For example, agglomeration methods can be used for biosensing. This approach is based on a peak wavelength shift resulting from the aggregation of the nanoparticles, which is induced by the target molecule.[114] Oligonucleotide covered Au nanoparticles are linked with a suitable polynucleotide target forming aggregates of Au particles to detect the presence and the amount of polynucleotide in the sample solution.[115,116] A whole blood immunoassay with minimized sample preparation has been realized by functionalized Au nanoparticles forming aggregates upon target protein binding and measurements in the near-infrared regime of light, resulting in sensitivities down to the low picomolar range.[22]

Another example for a biosensing principle making use of plasmonic nanoparticles in solution is the detection of target molecules through changes of the local refractive index near the particle surface.[117] Taking advantage of spectrally separated longitudinal plasmon resonance peaks of Au nanorods with different aspect ratios results in the realization of multiple target detection systems.[118,119]

Finally, plasmonic nanoparticles are also used for Surface-Enhanced Raman Spectroscopy or in the more conventional propagating surface plasmon resonance biosensors. The nanoparticle can be used to enhance the Raman scattering due to its local electromagnetic field as well as a label for the propagating plasmon signal, and leads to higher detection sensitivities.[90,120,121]

3.3. Hydrodynamic Nanoparticle Behavior

3.3.1. General Remarks and Behavior in External Rotating Magnetic Fields

In the absence of external magnetic fields, mobile magnetic nanoparticles are disordered and their orientation varies stochastically. By applying an external magnetic field, the particles are forced to align their magnetic moment parallel to the field direction, so that an ordered state of nanoparticle orientation is achieved, which undergoes relaxation processes after switching off the external field. Besides the Néel relaxation with an inverse time constant of τ_N (see chapter 3.1.1 and equation 3.1), Brownian relaxation of magnetic nanoparticles is observed too. While Néel relaxation describes the relaxation process of the particle's magnetic moment, Brownian motion leads to an additional relaxation process involving movement of the whole particle with a characteristic relaxation time τ_B.[122] Brownian relaxation depends on the particle size, the fluid viscosity, and the temperature. Néel relaxation is defined by the magnetic properties of the particle and can be treated as an internal rotational diffusion compared to the Brownian analog in the surrounding

fluid.[122]

Both relaxation processes can be combined by an effective relaxation time that is written as[123]

$$\frac{1}{\tau_{eff}} = \frac{1}{\tau_B} + \frac{1}{\tau_N}, \tag{3.32}$$

which, therefore, can be expressed as

$$\tau_{eff} = \frac{\tau_B \tau_N}{\tau_B + \tau_N}. \tag{3.33}$$

The Brownian relaxation time depends on the temperature T, the Boltzmann constant k_B and a rotational drag coefficient α and is defined by[124]

$$\tau_B = \frac{\alpha}{2k_B T}. \tag{3.34}$$

Here, the rotational drag coefficient in case of a spherical particle is[124]

$$\alpha = 6\eta V_{hydro}, \tag{3.35}$$

with the dynamic viscosity of the surrounding medium η and the hydrodynamic volume V_{hydro}. Therefore, τ_B can be written as

$$\tau_B = \frac{3\eta V_{hydro}}{k_B T}. \tag{3.36}$$

In case of cylindrical particles, Tirado and de la Torre calculated the rotational drag coefficient α to be[125]

$$\alpha = \frac{\pi \eta L_h^3}{3} \left(\ln \frac{L_h}{d_h} + C \right)^{-1}, \tag{3.37}$$

with L_h and d_h being the hydrodynamic length and diameter of the cylinder. In case of cylindrical particles used in this work, the geometric parameter relevant as an end cap correction factor C is given by[125]

$$C = -0.662 + 0.891 \frac{d_h}{L_h}. \tag{3.38}$$

While the Gilbert equation can be used to describe magnetization processes within solids, thermal agitation has to be considered for suspended magnetic nanoparticles in fluids, which results in the Fokker-Planck equation.[126] Shliomis has shown that the magnetization dynamics in an external magnetic field $\vec{H}$ can be represented in a linear approximation corresponding to small changes from the equilibrium magnetization, by a differential equation as[127]

$$\frac{d\vec{M}}{dt} = -\frac{1}{H^2 \tau_{par}} \vec{H} \left[\left(\vec{M} - \vec{M}_0 \right) \vec{H} \right] - \frac{1}{H^2 \tau_{perp}} \left[\vec{H} \times \left(\vec{M} \times \vec{H} \right) \right], \tag{3.39}$$

with the magnetic fluid magnetization $\vec{M}$ and under the assumption that the magnetic nanorods are rigid dipoles with fixed magnetic moments. Applying the effective field method results in the equilibrium magnetization of the whole nanoparticle ensemble with concentration n to have the following form:[127,128]

$$\vec{M_0} = nmL(\xi)\frac{\vec{H}}{H}. \tag{3.40}$$

The Langevin function $L(\xi)$ is defined as

$$L(\xi) = \coth\xi - \frac{1}{\xi}, \tag{3.41}$$

with

$$\xi = \frac{mH\mu_0}{k_B T} \tag{3.42}$$

and a magnetic moment of a single particle of

$$m = \frac{\pi}{4} M_S L_C d_C^2, \tag{3.43}$$

with L_C being the magnetic core length and d_C the diameter, respectively. M_S denotes the saturation magnetization.[33,129]

For cylindrical particles, two distinct relaxation times can be distinguished. One relaxation time describing relaxation parallel to the cylinder axis τ_{par} and another one τ_{perp} perpendicular to it.[127] These have the form of[127]

$$\tau_{par} = \tau_B \frac{d\ln L(\xi)}{d\ln\xi} \tag{3.44}$$

and

$$\tau_{perp} = \tau_B \frac{2L(\xi)}{\xi - L(\xi)}. \tag{3.45}$$

In case of an external rotating magnetic field

$$\vec{B} = \begin{pmatrix} B_0\cos\omega t \\ B_0\sin\omega t \\ 0 \end{pmatrix}, \tag{3.46}$$

with angular frequency ω, field amplitude B_0 and a constant phase lag ϕ of the magnetization with respect to the external magnetic field of the form

$$\vec{M} = \begin{pmatrix} M\cos(\omega t - \phi) \\ M\sin(\omega t - \phi) \\ 0 \end{pmatrix}, \tag{3.47}$$

a cubic equation describes the behavior of the phase lag (with $x = \tan\phi$):[127,129]

$$x^3 - (\omega\tau_B)\,x^2 + \left(1 + \frac{1}{2}\xi L(\xi)\right)x - \omega\tau_B = 0. \tag{3.48}$$

The phase lag can be expressed as[127]

$$\phi = \arctan\left(\omega\tau_{perp}\right). \tag{3.49}$$

The above presented model has recently been further improved by Yoshida et al,[130] who modified the effective field model and extended it to a wide range of frequencies and amplitudes covering all of the typically used experimental conditions. In the following, this model will be presented in detail.

Under the assumption of single-domain nanoparticles with spherical shape and a fixed magnetization direction ($\tau_B \ll \tau_N$), the Fokker-Planck equation, which characterizes the behavior of a magnetic fluid in an external rotating magnetic field, takes the following form:

$$2\tau_B \frac{\partial W}{\partial t} = \frac{1}{k_B T}\left(\nabla^2 E\right) W + \frac{1}{k_B T}\left(\nabla E\right)\left(\nabla W\right) + \nabla^2 W \tag{3.50}$$

with the potential energy of a particle with magnetic moment m within an external magnetic field B

$$E(\theta, \phi, t) = -mB \sin\theta \cos\left(\omega t - \phi\right) \tag{3.51}$$

and W as the time and orientation dependent distribution function of the magnetic moment vectors of an ensemble of single-domain nanoparticles.[130]

By using numerical solutions of the Fokker-Planck equation and comparing to the effective field model of cylindrical nanorods, the latter has been modified, and the result is a set of empirical equations describing the dynamics of magnetic nanocylinders in a rotating external field.[130]

The equation describing the real part of the magnetization is

$$\frac{M'}{M_s} = \frac{L\left(\xi\right)}{1 + \left(\omega\tau_{perp}\right)^2}\left[\frac{1 + a_4\left(\omega\tau_{perp}\right)^2 + a_5\left(\omega\tau_{perp}\right)^{a_3}}{1 + a_1\left(\omega\tau_{perp}\right)^2 + a_2\left(\omega\tau_{perp}\right)^{a_3}}\right] \tag{3.52}$$

and for the imaginary part it is

$$\frac{M''}{M_s} = \frac{L\left(\xi\right)}{1 + \left(\omega\tau_{perp}\right)^2}\left[b_1 + b_2 \frac{\left[1 + \left(\omega\tau_{perp}\right)^2\right]\left(\omega\tau_{perp}\right)^{(0.4b_3 - 1)}}{1 + 0.25\left(\omega\tau_{perp}\right)^{2b_3}}\right], \tag{3.53}$$

with

$$a_1 = \frac{3.76\xi^2 + 0.029\xi^4}{1 + 29.6\xi + 7.61\xi^2 + 0.00382\xi^4}, \tag{3.54}$$

$$a_2 = 0.13\xi^{1.1}, \tag{3.55}$$

$$a_3 = 4 + 16\left(\frac{\xi}{\xi + 17}\right)^2, \tag{3.56}$$

$$a_4 = 0.1\xi, \tag{3.57}$$

$$a_5 = \frac{0.0865\xi + 0.205\xi^2 + 0.000397\xi^4}{1 + 0.88\xi + 0.606\xi^2 + 0.00652\xi^4}, \tag{3.58}$$

$$b_1 = 1 - \frac{0.2\xi^{1.2}}{\xi^{1.2} + 5.5}, \tag{3.59}$$

$$b_2 = \frac{0.6\xi^{1.5}}{\xi^{1.5} + 16} \tag{3.60}$$

and

$$b_3 = 1.4 + \frac{3.2\xi}{\xi + 5}. \tag{3.61}$$

The phase lag ϕ is then calculated by

$$\phi = \arctan \frac{M''}{M'}. \tag{3.62}$$

3.3.2. Biomedical Applications Using the Nanoparticles' Hydrodynamic Behavior

The change of the hydrodynamic behavior of nanoparticles as a stand-alone signal is only rarely used for biosensing applications. Normally, other properties of nanoparticles are exploited as well (e.g. the magnetic behavior for magnetorelaxation based biosensors). Additional examples are mentioned in chapters 3.1.2 and 3.2.3.

Apart from these methods, changes in the hydrodynamic volume of nanoparticles are detectable by dynamic light scattering (DLS), which is also known as photon correlation spectroscopy.[131] Though DLS suffers from a complex instrumentation, a relatively long measurement time with restricted ability for high throughput testing and weaknesses for polydisperse samples, label-free DNA detection with functionalized Au nanoparticles has been proven with sensitivities down to the picomolar range.[132]

An optical method with a simpler experimental setup compared to DLS is accomplished by nanoparticle tracking analysis instruments of the company NanoSight (UK), which use changes of the hydrodynamic volume and, hence, observe changes in Brownian motion.[133] This instrument is mainly used for characterizing the size and the zeta potential of nanoparticles, proteins, viruses, etc, but can also be used for biosensing applications (e.g. enzyme detection on the surface of nanoparticles has been reported).[134,135]

4. Experimental Setup

In this chapter, the PlasMag setup used for measurements of the rotational behavior of magnetic nanoparticles in external magnetic fields is presented. It consists of three main parts (see Fig. 4.1 for a sketch of the setup), which are the rotating magnetic field generating component, the optical detection unit for measurements of the transmission of nanoparticle suspensions and an interface for electronic data acquisition.

The rotating magnetic field is generated by two perpendicular Helmholtz coils, which are fed by two sinusoidal currents 90° phase shifted to each other. The currents are monitored via shunt resistors, which allow the calibration of the amplitudes and the phases of the two currents and, hence, the rotating magnetic field. The sound card of the measurement computer is used for the generation of the two sinusoidal currents, which are further amplified by a commercially available two channel audio amplifier that is able to produce high currents at low frequencies.

The optical part of the setup consists of a fiber coupled laser diode that generates a collimated light beam with a high degree of polarization. After passing through the sample solution in a cuvette in the center of the setup, the transmitted light is collected by a focusing lens attached to a second fiber that passes the transmitted light to a photodetector.

The main component for data acquisition is a Lock-in amplifier that records the generated signal and calculates the phase lag between the magnetic field and the long particle axis. While the signal input of the Lock-in amplifier is sourced by the output channel of the photo detector, the reference input is fed by the signal generated at the shunt resistor of the Helmholtz coil with its axis aligned parallel to the polarization direction of the incoming laser light beam. The Lock-in amplifier is set to measure the second harmonic of the reference signal due to the elongated symmetry of the used nanorods. Measurements of the signal amplitude and phase are carried out as a function of the frequency and the magnitude of the applied rotating magnetic field. A custom LabView program controls the signal output for generating the currents fed to the coils and is responsible for data acquisition as well.

As the measurement setup has been continuously developed throughout the time of this thesis, the results presented in the following chapters are not always based on exactly the same setup. No basic components have been changed, however, mainly the optical part has been improved from the first to the present setup in order to allow future scattering measurements with a photomultiplier tube. Furthermore, the setup has been incorporated in a small lightproof box, which

paves the way for further development of a transportable POC device.

The first initial version of the setup is shown in Fig. 4.2. The main components are installed on an optical air damped breadboard. The optical part of the setup is mechanically decoupled from the Helmholtz coils, thus, ensuring minimization of mechanical vibrations.

The current version of the setup is shown in Fig. 4.3. Modifications concern the installed laser module with changed wavelength. Consequently, a different photodetector with according spectral sensitivity is installed. The main parts of the optics are assembled in a lightproof box. Furthermore, this setup includes an option for a future installation of a photomultiplier tube for highly sensitive detection of scattered light.

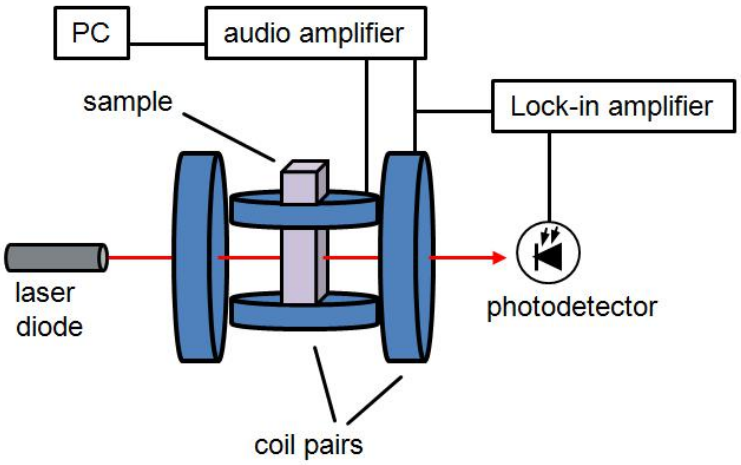

Figure 4.1.: The PlasMag setup. Two perpendicular Helmholtz coils with the sample cuvette in their center are fed by currents generated by the sound card of a computer and an audio amplifier to generate a rotating magnetic field. A laser diode and a photodetector are used to measure the sample's transmission. The Lock-in amplifier compares the optical to the magnetic signal and calculates the phase lag between the two.[10,11]

In the following chapters, the different components of the experimental setup are described in more detail.

4.1. Helmholtz Coils and Magnetic Field Generating Components

Two Helmholtz coils are used, which are aligned perpendicularly to each other and are sourced by the two channels of an audio power amplifier (ATEC LAB power amplifier FPt14000BP). The input signal for the amplifier is generated by a LabView code and sourced by a soundcard (E-MU Systems model 0404).

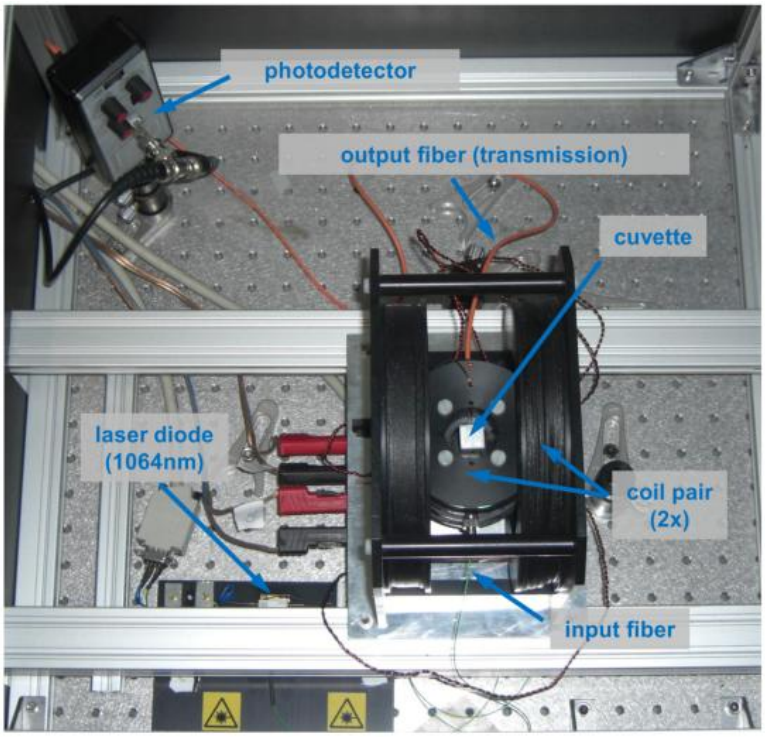

Figure 4.2.: The main parts of the setup mounted on an air damped optical breadboard. The whole setup is enclosed in a box to do justice to laser safety regulations.

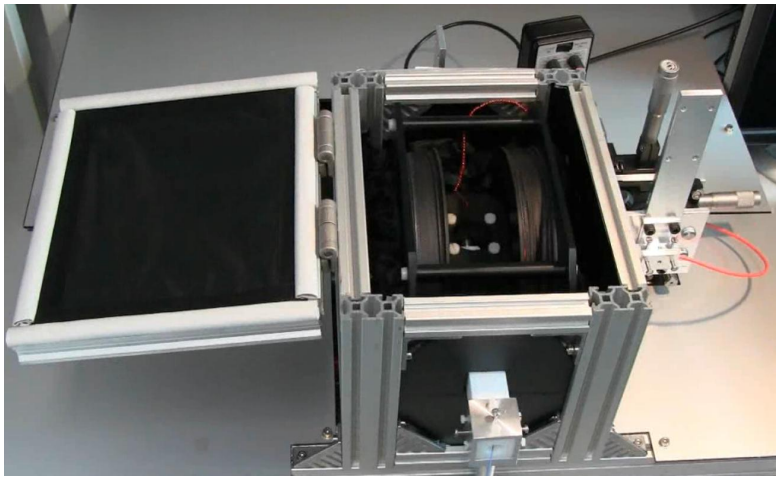

Figure 4.3.: The main parts of the new revised setup enclosed in a small lightproof box.

Each coil is fed by a sinusoidal current, while the two currents possess a relative phase shift of 90° to each other. This results in a circular homogeneous rotating magnetic field as long as each coil's current is in phase with its corresponding magnetic field (see appendix A for a full characterization of the coils and the currents' phase behavior). The resulting magnetic field is controlled by measuring the current through each coil via the voltage drop across precision shunt resistors (Isabellenhuette RUG-Z, 0.5 Ohm), which allows to adjust the amplitudes and relative phases of the left and right output channel of the power amplifier until a rotating magnetic field of desired strength is obtained at the frequency of interest. Field magnitudes of 10 mT can be generated up to a maximum frequency of 430 Hz, 5mT fields up to 1130 Hz, while frequencies higher than 2 kHz are possible for field magnitudes of 2.5 mT and below. In principle, higher magnitudes and frequencies could be obtained by setting up discrete electrical resonant circuits.

4.2. Optics

The light generating part of the optical setup consists of a polarization maintaining fiber-coupled laser diode (OECA LQ7i-1060-25/BF2-FCSPC) with high polarization extinction ratio (30 dB) at 1060 nm which is power and temperature controlled by a laser diode combi controller (Thorlabs ITC510). The use of a laser light source emitting in the infrared regime of light is associated with the length of the used nanorods and with the sample fluid, and will be explained later in chapter 5.2. To point the laser light beam to the sample cuvette, a fiber coupled collimator is employed with a light beam diameter of 0.5 mm. A focusing lens mounted on a multi-mode fiber is used to collect light from the center of the sample cuvette and for subsequent coupling of the transmitted light into the photodetector (New Focus Model 2011).

Changes in the optics for the revised measurement setup were made concerning the light wavelength, i.e. a decrease down to smaller wavelengths to be able to use common photomultiplier tubes for scattering experiments. The new laser supplied a wavelength of 785 nm (Frankfurt Laser Company FLQ-785-30S-BTF-PM) which resulted in a change of the photodetector (New Focus Model 2051) to suit the decreased wavelength. To achieve a high polarization extinction ratio, a fiber optic polarizer (OZ Optics FOP-11-11-785-5-125-P-P-40-3S3S-1-1-ER=25) has been installed, and to reduce disturbances from back scattered light, a polarization sensitive isolator has been mounted between the laser and the polarizer (OZ Optics FOI-11-11-785-5-125-P-40-3A3S-1-1-35). The output fiber can also be positioned at an angle of 90° with respect to the incoming light path for a possible measurement in scattering geometry, which would involve, as mentioned above, a photomultiplier tube for appropriate light detection.

4.3. Data Acquisition

The voltage drop at the shunt resistor of the coil with its axis aligned parallel to the polarization direction of the incoming laser light is fed to the reference channel of a Lock-in amplifier (Signal Recovery DSP 7265), while the signal channel is sourced by the photodetector output of transmitted light intensity. The signal of interest is the second harmonic. This is due to the axial symmetry of the particles. Every 180°, the spatial orientation of rotating particles' long axis is repeated, so that the optical signal is frequency doubled with respect to the magnetic signal. This is schematically illustrated in Fig. 4.4.

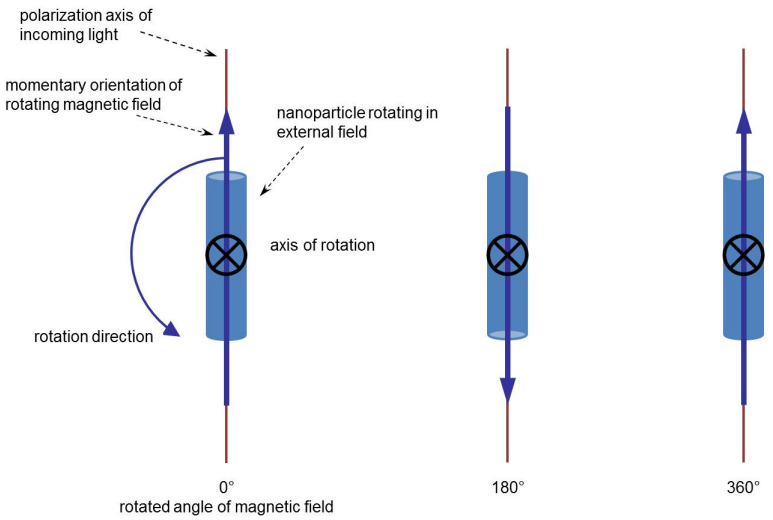

Figure 4.4.: Origin of the second harmonic signal. The particle is aligned parallel to the polarization direction twice dyring one rotation cycle of the magnetic field. This results in a frequency doubled optical signal.

A custom LabView program consisting of a signal generating part (used in chapter 4.1 for supplying sinusoidal currents to the Helmholtz coils) and a data acquisition part is used to initialize the Lock-in amplifier and to read out data. Phase and amplitude of the optical signal are recorded in dependence of frequency and magnitude of the rotating magnetic field and stored in a data file (with a phase uncertainty of the PlasMag setup below 0.5°). Finally, further signal processing and interpretation of the obtained data is carried out with a graphing and data analysis software (OriginLab).

5. Results and Discussion

5.1. Description and Properties of the used Nanoparticles

Plain magnetic Co and Ni nanorods are used as model systems for an initial proof of principle of the PlasMag measurement method and for the detection of unspecific protein adhesion.

For sHER2 cancer biomarker detection measurements, the synthesis route of the Co nanorods has been improved, resulting in noble metal shell coated nanorods. The noble metal shell offers multiple advantages. First, the shell prevents the core from being oxidized and second, the noble metal shell supports plasmon resonances that allow to decrease the amount of particles used for the PlasMag measurements, which subsequently improves the sensitivity of the PlasMag measurement system.

Stabilization and functionalization in aqueous buffer solutions was achieved via coating the nanoparticles with a polymer. For a first proof of specific binding, the particles have been functionalized with biotin to target streptavidin. Additionally, functionalization with the Herceptin antibody as recognition agent for sHER2 was carried out.

Particle synthesis by electrodeposition into commercially available nanoporous filter membranes was carried out. Ni and Au nanorods as well as nanorods with subsequent segments of those two metals were fabricated. The synthesis and especially the stabilization of these nanorods in aqueous dispersions is still under investigation, so that these nanorods have not been used for measurements with the PlasMag system yet. Their fabrication and an outlook for further improvement is presented in appendix B.

The different synthesis types of the employed nanorods are described in the following chapters as well as structural and magnetic characterization results and the respective stabilization and functionalization procedures.

5.1.1. Cobalt Nanorods

The Co nanorods are supplied by the group of Katerina Soulantica in Toulouse (Université de Toulouse, INSA, UPS, LPCNO, and CNRS).

Plain Co nanorods dissolved in organic solvents can be synthesized from organometallic precursors to obtain nanorods with high precision of shape and excellent size control.[59] These single-crystalline nanorods possess a fixed diameter of about 6 nm and adjustable lengths between 40 nm and 200 nm with standard deviations

of the length and the diameter of less than 10% (see Fig. 5.1 for a transmission electron microscopy (TEM) image of such a nanorod batch).[136] The synthesis follows the protocol published by Wetz et al. based on the decomposition of a cobalt coordination precursor ($Co[N(SiMe_3)_2]_2$).[136] Under addition of lauric acid (LA) and hexadecylamine (HDA), the precursor is mixed with an organic solvent in a Fischer-Porter pressure vessel inside a glovebox. The closed vessel is charged with H_2 under magnetic stirring after evacuation. In a next step, the vessel is transferred to an oil bath that is heated up to the reaction temperature. Modifications of the reaction conditions (time, temperature, H_2 pressure, Co/LA/HDA ratio, solvent) are used to adapt the mean length of the aspired nanorods. The nanocrystals have to be purified by centrifugation in order to separate spherical from cylindrical nanoparticles. After a drying step the nanorods are redispersed in organic solvents such as toluene or THF (tetrahydrofuran). The dispersion in organic solvents and a subsequent storage under argon atmosphere is necessary to avoid oxidation.[10,136] This is schematically the synthesis route for the first particles that have been tested with the PlasMag platform (results will be presented later in chapter 5.4.1).

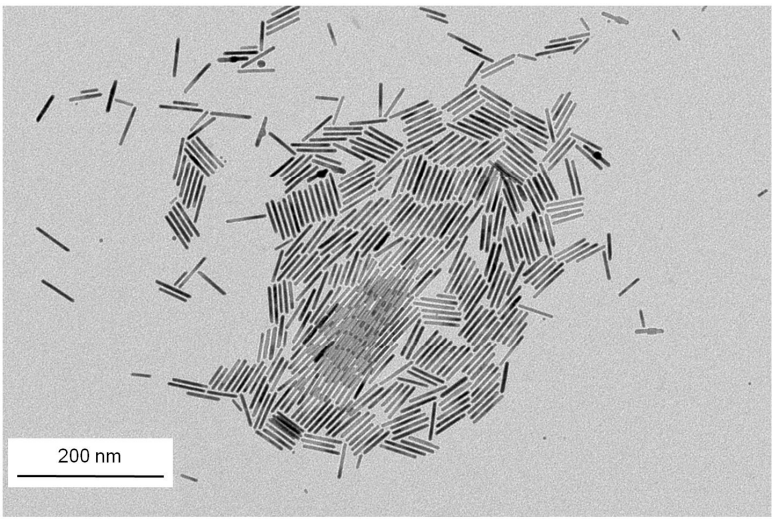

Figure 5.1.: TEM image of bare Co nanorods of 52±4.6 nm length and 5±0.5 nm diameter.

The particle fabrication procedure was further optimized recently. To prevent agglomeration and to avoid that particles come into very close contact and form irreversible aggregates, the synthesis procedure has been changed with the aim to circumvent the drying step. Furthermore, a noble metal shell is synthesized around the Co core in order to protect the core from oxidation in aqueous solutions and to provide amplification of the optical signal. This is accomplished via a thin metal interlayer (IL) of tin that reduces the difference in surface energies between the Co core and the noble metal shell. Regarding the noble metal

shell, sequential deposition of Platinum (Pt) and Au proved to provide the best protection of the core against oxidation, resulting in stability periods of aqueous nanorod dispersions of more than eight weeks. A possible reason for the stability of the combined Pt and Au shell is demonstrated in Fig. 5.2, which shows energy-dispersive X-ray spectroscopy (EDX) analysis of a nanorod TEM image. The EDX signal contains information about the elemental composition of the nanorods. The signal originating from different metals are represented by the colored images in the figure. Clearly, the Au deposition has the tendency to fill up existing gaps in the previous Pt coating, so together, these two materials form a highly stable shell. Both noble metals, Pt and Au, form grains on the tin covered surface of the nanoparticle, which leads to the growth of the noble metals on different sections on the nanoparticle surface. Additionally, Pt and Au are not miscible, which supports the presence of grains of Pt and Au.[137] In total, the interlayer and the noble metal shell amount to an average shell thickness of about 1.8 nm.

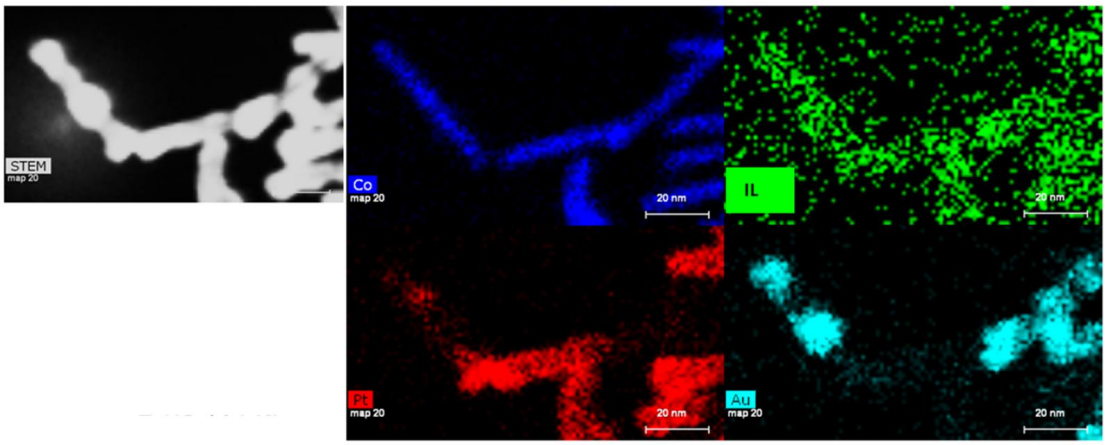

Figure 5.2.: EDX of noble metal shell coated Co nanorods. Based on the TEM image in the left, EDX is used to separately image the individual metals. Starting from Co (dark blue) nanorods, a metallic interlayer (green) is deposited, followed by subsequent deposition of Pt (red) and Au (bright blue). The combination of Pt and Au results in a complete noble metal coverage of the magnetic core.

The synthesized nanorods are usually stabilized with hydrophobic surfactants in organic solvents such as toluene, so that they have to be transferred and stabilized in aqueous solutions to enable biofunctionalization and subsequent binding measurements of target molecules. For this reason, coating of the nanorods has been developed at the Philipps-Universität Marburg (PUM) by the group of Wolfgang Parak with an amphiphilic polymer, i.e. a polymer (PMA - Poly(isobutylene-alt-maleic anhydride)) comprising hydrophobic side chains for the linkage to the nanorod surface and a hydrophilic backbone that provides water solubility through charged groups.[138,139] The coating and activation procedure is sketched in Fig.

5.3. Specifically, in a first step, the polymer is mixed in THF with dodecylamine sufficient to bind to approximately 75% of the polymer backbone rings. Therefore, the anhydride rings are opened and carboxy (COOH) groups are created, which are used to bind the dodecylamine via its amine (NH_2) group. Next, the particles dissolved in $CHCl_3$ are added and by evaporating the organic solvent, the polymer binds to the hydrophobic surfactant layer of the nanorods (HDA and LA). Binding of the polymer is achieved via its hydrophobic side chains due to hydrophobic interaction. About 1000 PMA monomers per nm^2 of particle surface are used. Afterwards, the remaining 25% of the rings on the polymer backbone have to be opened to ensure water solubility and electrostatic stabilization based on the resulting carboxy groups, which is accomplished by incubation in basic media (i.e. 0.1 M NaOH). Repeated gentle centrifugation is used to wash out unbound polymer and for the transfer to water. Finally, the nanorods can be redissolved in the chosen aqueous buffer solution. Excellent stability of the resulting nanorod dispersions has been verified by their highly negative Zeta potential of around -80 to -100 mV (measurements carried out in deionized water by a Malvern Zetasizer Nano ZS, Model ZEN3600).

Measurements of the spectral transmission after the polymer coating procedure of the nanorods are shown in Fig. 5.4. A plasmon resonance peak (minimum in the transmission spectrum) at a wavelength of about 530 nm is observed, which has its origin in the presence of grains of Pt and Au within the noble metal shell. A longitudinal plasmon resonance can not be observed, which for the present nanorod geometry would be expected at around 800 nm. Therefore, improvement of the detectable nanorod concentration by exploiting the enhanced nanorod-orientation dependent scattering of longitudinal plasmon resonances can not be achieved, but the noble metal shell prevents the core from oxidation, which is a prerequisite for the transfer to water.

Following stabilization in water, the nanorods have been functionalized by conjugating recognition agents to the carboxy groups of the polymer backbone. To that end, well established N-(3-Dimethylaminopropyl)-N'-ethylcarbodiimide hydrochloride (EDC) / N-Hydroxysulfosuccinimide sodium salt (Sulfo-NHS) carboxy activation to couple amine groups is employed (reagents purchased from Sigma-Aldrich).[140] Amine-modified biotin as recognition agent for streptavidin is coupled to the carboxy groups of the polymer backbone. Therefore, biotinylated and amine conjugated polyethylene glycol polymers with a molecular weight of about 3000 Da, purchased from RAPP Polymere, as well as EZ-LINK Pentylamine-Biotin with a molecular weight of about 310 Da, purchased from VWR, are applied. This is accomplished by mixing the particles with EDC, Sulfo-NHS and the amine conjugated biotin. All reagents are added in a 100k mol excess to the number of nanoparticles. After a reaction time of 1h, the particles are gently centrifuged to wash out free unbound EDC, Sulfo-NHS and biotin complexes by precipitation. Afterwards, the particles are redissolved in water or buffer solution.

The procedure of binding the monoclonal antibody Herceptin[141] as recognition agent for sHER2 assays has been employed according to the biotinylation protocol

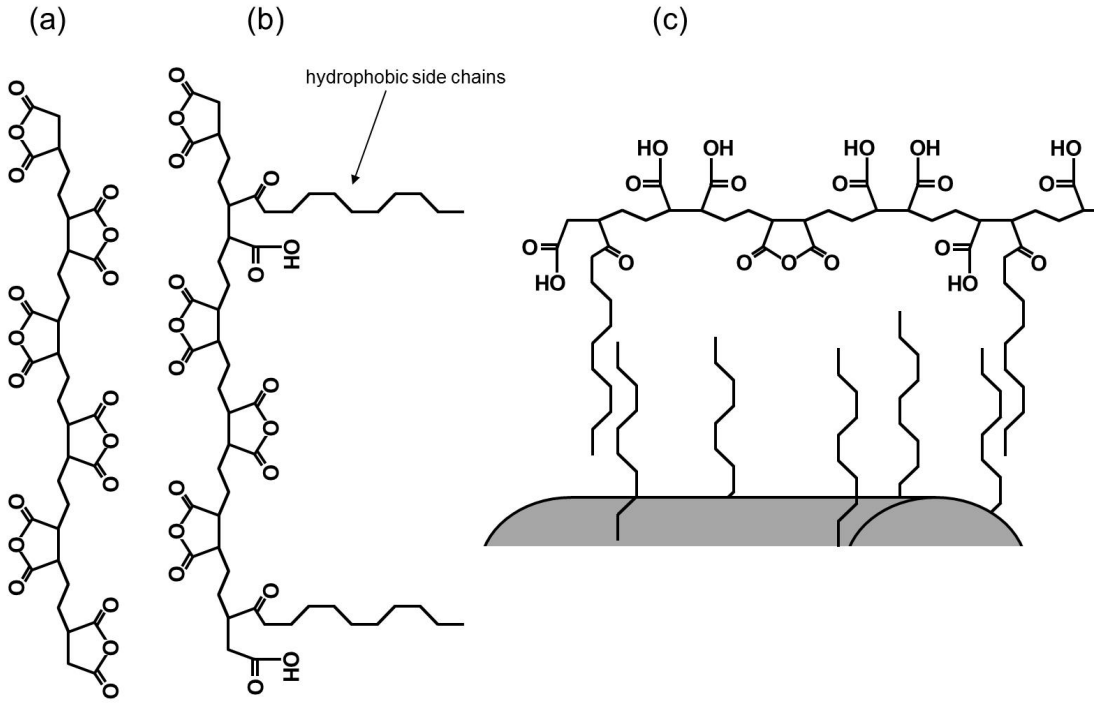

Figure 5.3.: Schematic illustration of the polymer coating procedure. (a) The initial polymer backbone with the anhydride rings. (b) Hydrophobic side chains are added to the backbone via opening the rings of the polymer and by a reaction of the amine with the created carboxy group. (c) The hydrophobic surfactant on the nanoparticle surface interacts with the hydrophobic side chains of the polymer and binding is formed via hydrophobic interaction. Opening the rest of the rings increases the number of carboxy groups and allows an electrostatic particle stabilization in aqueous solution.[138]

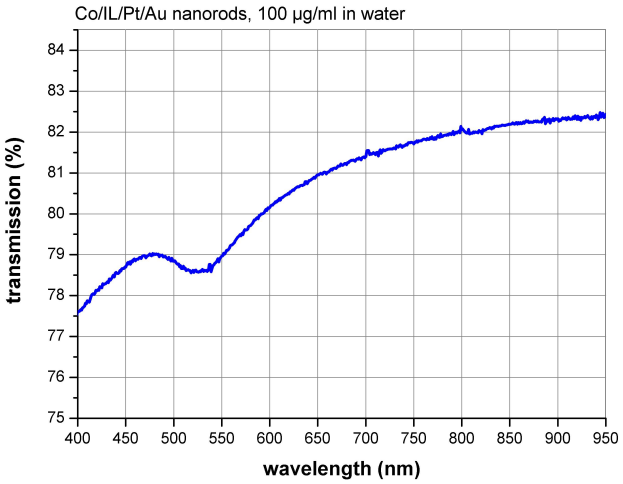

Figure 5.4.: Spectral transmission of polymer stabilized noble metal coated nanorods. No longitudinal plasmon resonance can be observed (expected at about 800 nm). The minimum of transmission at about 530 nm, which is typical for particles with a nearly spherical geometry, indicates that the noble metal shell consists of separated grains.

mentioned above.

Recognition agent coupling has been verified by a substantial loss in Zeta potential magnitude (typically 30-40 mV) induced by the binding of the polymer carboxy groups to amines that decreases the overall nanoprobe charge.

5.1.2. Nickel Nanorods

Synthesis of Ni nanorods into nanoporous alumina templates by electrodeposition from a Watts bath has been realized in Saarbrücken (Saarland University) by the group of Andreas Tschöpe according to a protocol described previously by Guenther et al.[142] Here, a two step anodization process in sulfuric acid is applied to create a nanoporous alumina membrane in an aluminum foil. After the first anodization, the resulting alumina surface is dissolved in phosphoric acid. The anodization process is then repeated, resulting in highly ordered nanoporous films with pore diameters between 20 and 30 nm. Afterwards, the pores are filled with Ni in a Watts bath comprising of nickelsulfate, nickelchloride and boric acid by pulsed electrodeposition. Drying of the substrate has to be avoided to ensure uniform pore filling. Control of the length of the rods is achieved by adjusting the overall charge transfer during the pore filling step.

Finally, the membranes are transferred to a NaOH solution to dissolve the oxide and to release the nanorods. Adding Polyvinylpyrrolidone (PVP) as surfactant to the alkaline etchant ensures stabilization of the Ni nanorods resulting in single

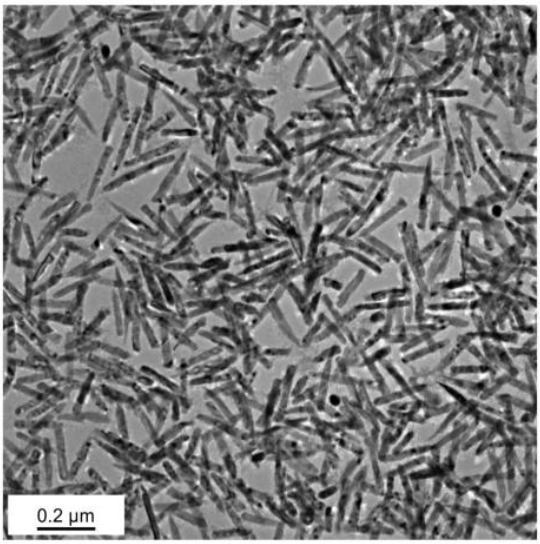

Figure 5.5.: TEM image of a Ni nanorod batch recorded in Saarbrücken by Annegret Günther and Andreas Tschöpe. The mean magnetic core length of the particles is 182±29 nm and the mean magnetic core diameter is 26±3 nm.[11]

particle dispersions. Washing of the solution and transfer of the particles to water is done via precipitation in a centrifuge and sonication.

To examinine the geometry of the particles, TEM is used and the recorded images are taken to determine the mean and standard deviation of the length and diameter (see Fig. 5.5). With TEM imaging, the PVP surfactant layer is not visible, so that the geometry of the bare magnetic core can be determined. The length and diameter of the here employed nanorod batch amount to 182±29 nm and 26±3 nm, respectively.[11] Magnetic characterization has been done by vibrating sample magnetometry (VSM) and reveals a mean particle magnetic moment of $3.75 \cdot 10^{-17}$ Am^2.[11]

These particles are single dispersed in water, but very sensitive to changes of the salt concentration and the pH value. Thus, these Ni nanorods cannot directly be used for specific functionalization by a recognition agent, but are well suited to characterize unspecific protein binding in water. Results will be presented in chapter 5.4.2.

5.2. Modeling of the Ideally Suited Nanoparticle

By modeling of the nanoparticle characteristics prior to the execution of measurements, the ideal shape and composition of a suitable nanoparticle type can be determined. Thus, modeling results serve as a guideline for the development of a synthesis procedure. Moreover, the modeling of the behavior of rotating nanorods helps to understand and to interpret obtained experimental results, which in turn

allow to continuously improve the theoretical model.

The following subsections deal with the three main characteristics of suitable nanoparticles, which are the optical, magnetic and the rotational properties. Each of these properties can be characterized individually, however, to obtain the most useful particle type, all three have to be regarded as an ensemble of interconnected parameters. Therefore, it is not enough to optimize one of them if the others are not taken into account. For example, a very small particle size would maximize the effect of relative increase in hydrodynamic drag upon target molecule binding, but on the other hand, it would obviously hinder a successful optical detection. Furthermore, technically feasible synthesis routes have to be kept in mind to obtain useful results.

Optimization of the optical response to the incident light allows to use a low nanoprobe concentration in the sample volume, which leads to an increased sensitivity of the biosensing principle. Also, by separating the longitudinal plasmon resonances of differently functionalized types of nanorods used together in the same sample volume, multiplexing analysis can be made possible. Optical simulation results of ideal particles will be presented and discussed in the first section. It concludes with an outlook on alternative particle types that could also be used for the PlasMag measurement system from an optical point of view.

Magnetic nanorod property modeling defines the degree of orientation in an external magnetic field of a certain strength, which affects the magnitude of the obtained measurement signal. Modeling of the rotational nanorod behavior in an external field specifies usable nanorod dimensions and enables to estimate the biosensing potential of the proposed technique.

The modeling presented here, explicitly focuses on Co core nanorods (presented in chapter 5.1.1), as these represent particles, which meet best the needs of the PlasMag measurement principle.

5.2.1. Optical Nanorod Property Modeling

The modeling of the optical nanoparticle characteristics allows to determine the most suitable particle geometry regarding a maximization of the scattered and absorbed light to enable detection of particle concentrations as low as possible.

In this chapter, optical nanorod properties studied by the DDA code DDSCAT will be discussed (see chapter 3.2.2). For the sake of simple comparison of the gained results, water is chosen as the surrounding medium throughout all simulations presented in this chapter even for bare Co nanorods. Unless otherwise specified, linearly polarized incident light and nanorods oriented with their long axis parallel to the polarization direction are assumed. Mainly, this chapter focuses on plasmonic enhancement of the optical properties of suitable nanorod types upon the addition of noble metal shells, which enables to tune the nanorod scattering and absorption behavior.

From an optical point of view, even bare magnetic nanorods are suitable and appropriate for the proposed PlasMag measurement technique. In linearly po-

larized light, the extinction depends on the angle between the long nanorod axis and the direction of polarization, which is the basic prerequisite of the PlasMag detection method. This is demonstrated in Fig. 5.6, which exemplarily shows calculated extinction cross sections for plain cylindrical Co nanorods with a length of 80 nm and a diameter of 6 nm (see chapter 5.1.1 for fabrication details on these nanorods). Here, α denotes the angle between the nanorod's long axis and the direction of polarization. The figure shows that the extinction is high in case of a parallel nanorod orientation (black line, $\alpha = 0°$) and decreases with increasing angle, reaching its minimum for perpendicular orientation (green line). Even though no plasmon resonance can be excited within this wavelength range, the intrinsic anisotropic polarizability of rod-shaped particles allows to employ even bare magnetic nanorods as probes for PlasMag measurements. The different slopes of the single extinction spectra in the figure at small wavelengths indicate a transversal plasmon resonance peak at a wavelength smaller than 300 nm. In non-polarized light, the extinction spectrum would be identical for all possible particle orientations. The geometry of the nanocylinder has been chosen with respect to experimentally obtainable Co nanorods that possess the advantage of being small in size with a narrow distribution of particle geometry parameters.

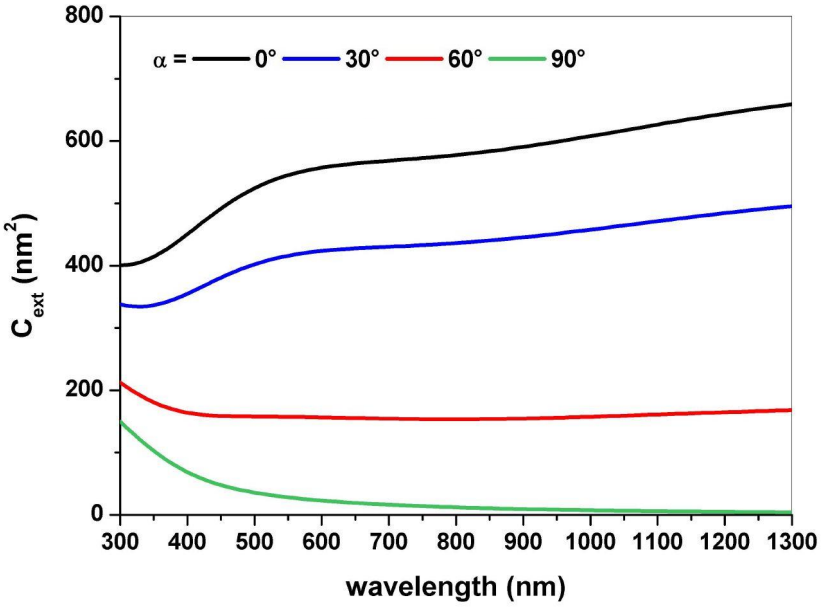

Figure 5.6.: Extinction spectra of bare Co cylinders (80 nm length and 6 nm diameter) for different angles between the direction of incoming light polarization and the long axis of the nanocylinder, ranging from parallel ($\alpha = 0°$, black) to perpendicular (green line) orientation.

The choice of the laser wavelength of 1060 nm in the experimental setup (see

chapter 4) is supported by measurements of the transmission spectra of deoxyhemoglobin and saline buffer solutions, which shows a maximum in the near infrared regime of light.[143,144] The difference in extinction between parallel and perpendicular oriented nanoparticles at the used light wavelength is proportional to the measured signal magnitude. Therefore, it serves as a parameter for comparing different nanorod types. This value amounts to about 610 nm^2 for the shown bare Co nanorods (Fig. 5.6) and will be used later in this thesis again.

In general, particles that support plasmon resonances show significantly increased scattering and transmission characteristics (see chapter 3.2 for details on plasmon resonances). The geometry of the nanoparticle is the main factor determining the peak position of the plasmon resonance wavelength. This is shown schematically in a normalized plot (see Fig. 5.7) for the case of bare Au particles. Here, spheres of different diameters are compared to cylinders of varying aspect ratios. While an increasing diameter of spheres does not significantly change the plasmon resonance peak position (black line d=5 nm, grey line d=40 nm), a change of the aspect ratio of cylinders results in large shifts of the longitudinal plasmon resonance peak position (d=10 nm fixed; lengths vary from L=20 nm, red line, to L=70 nm, orange line).

For characterization of suitable core-shell nanorods, experimentally already available bare magnetic nanorods, as used for the spectra simulation in Fig. 5.6, have been chosen as core-particles. In Fig. 5.8, the influence of the noble metal shell thickness on the longitudinal plasmon resonance peak is shown. Here, a Au shell is assumed as noble metal coating on the Co nanorods. The simulations show that with increasing shell thickness, a sharp longitudinal plasmon peak is formed. The thicker the Au shell, the more the peak wavelength is shifted to the visible range of light. Also, the peak sharpness and height increases. By comparing the spectra of Au coated nanorods (Fig. 5.8) to bare Co nanorods (Fig. 5.6), an increase in extinction cross section of about a factor of 100 can be gained by adding a Au shell.

The effect of the gold's high electrical conductivity contrary to platinum, which has a lower conductivity is shown in Fig. 5.9, which compares the extinction of nanorods with a Pt shell to nanorods with a Au shell of the same thickness as well as to bare Co nanorods (Co core parameters: L=80 nm, d=6 nm). Furthermore, the extinction spectrum of nanorods with both platinum and Au as subsequent shells is plotted. It can be clearly seen that the 5 nm thick Au shell (green line) results in the sharpest peak, while Co nanorods do not show a peak wavelength at all (black line, see also Fig. 5.6). Platinum coverage (blue line) results in a broader peak, smaller in height, in the lower wavelength regime. Both noble metals as subsequent layers in the shell increases the height of the plasmon peak and results, in comparison to a plain Au shell, in a broadening of the overall peak (red line). Therefore, Au is preferred to Pt as shell material, as the Au shell results in a sharp plasmon resonance peak in the infrared wavelength regime, which can be achieved with the combined Pt / Au shell only at the prize of an enlarged particle volume. The combined Pt / Au noble metal shell used for the simulations

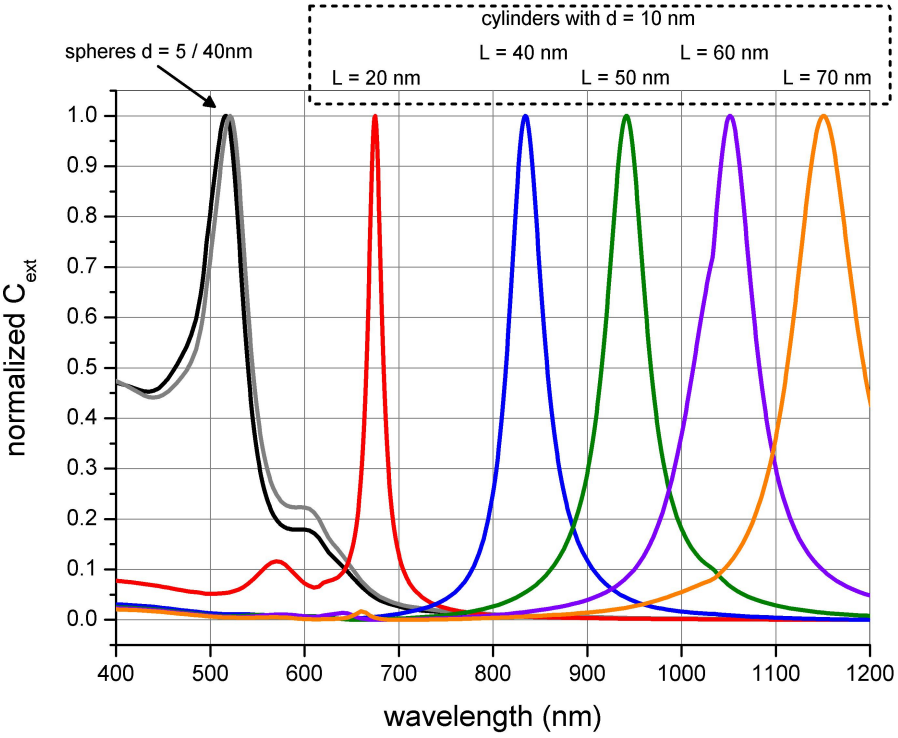

Figure 5.7.: Plasmon peak shift of bare Au particles of different shape and size in a normalized plot. While an increasing radius of spheres does not significantly change the plasmon resonance peak position (black line for d=5 nm, grey line for d=40 nm), a change of the aspect ratio of cylinders results in large peak shifts of the longitudinal plasmon resonance. The cylinders possess a fixed diameter of 10 nm and varying lengths.

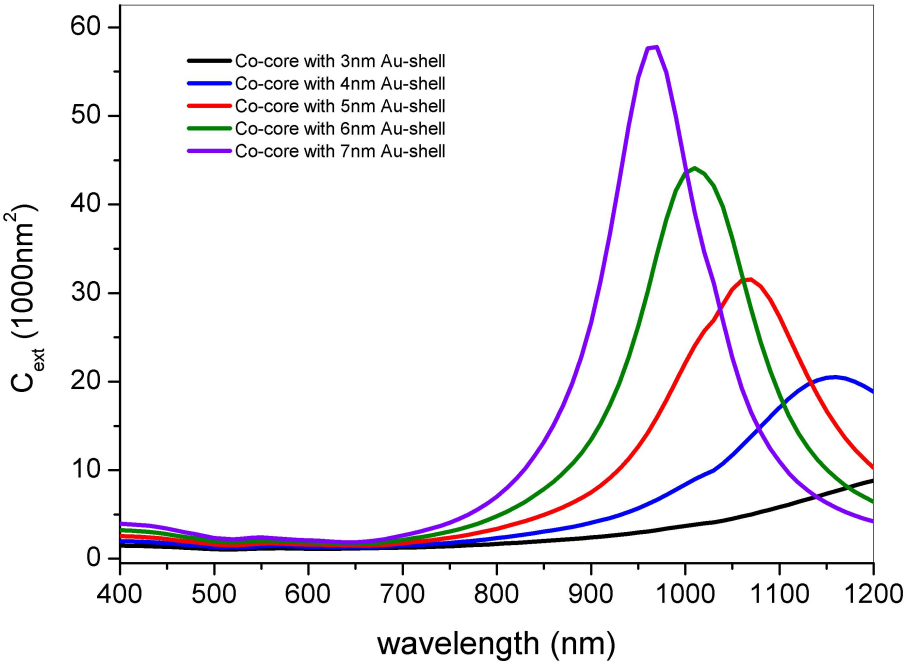

Figure 5.8.: Influence of the thickness of the noble metal shell in case of core / shell particles. Extinction spectra of the longitudinal plasmon resonances of cylindrical Co core particles (L=80 nm, d=6 nm) surrounded by Au shells of varying thicknesses.

can not be compared to the experimentally obtained shell in chapter 5.1.1 due the grain-like shell structure of the experimentally used nanoparticles.

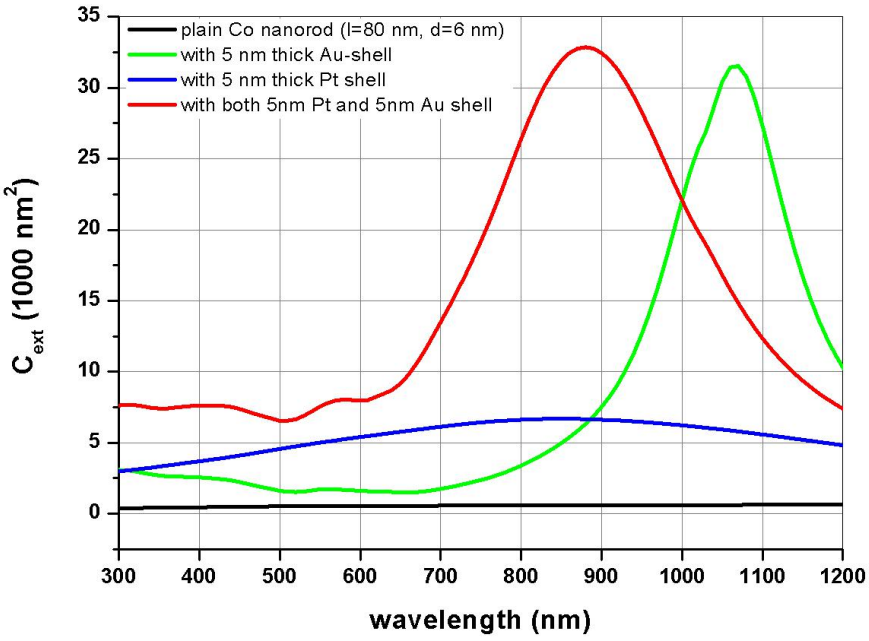

Figure 5.9.: Comparison of different shell materials. Longitudinal plasmon resonance spectra for bare Co nanorods (L=80 nm, d=6 nm, black), for Co core / Au shell nanorods (5 nm shell thickness, green), for Co core / Pt shell nanorods (5 nm shell thickness, blue) and for Co core nanorods with Pt (5 nm) and Au (5 nm) as subsequent shell layers (red line).

The PlasMag measurement signal originates from volume changes of the applied nanoparticles. Therefore, the smaller the volume of a bare nanoprobe is, the higher is the relative increase upon analyte binding and the better is the sensor's sensitivity. The simulations concerning the noble metal shell show that a Au shell thickness of 5 nm represents a good compromise between amplification of the optical extinction and the added particle volume. Thus, in the following simulations a Au shell thickness of 5 nm is assumed.

Fig. 5.10 illustrates the shift in longitudinal plasmon peak resonance position upon changes of the initial Co core length (diameter fixed at 6 nm, lengths varying from 60 nm to 100 nm) with a Au shell thickness of 5 nm. Nanorods with a Co core length of 80 nm and a Au shell thickness of 5 nm can be expected to show a longitudinal plasmon resonance peak in the targeted near-infrared wavelength regime. Additionally, this graph also shows a potential path towards multiplexed analyte detection in the same sample cuvette. Here, the behavior of differently functionalized nanorods could be resolved by employing nanorod batches of different core lengths and appropriate laser wavelengths for detection.

For Co nanorods (80 nm length and 6 nm diameter) surrounded by a 5 nm

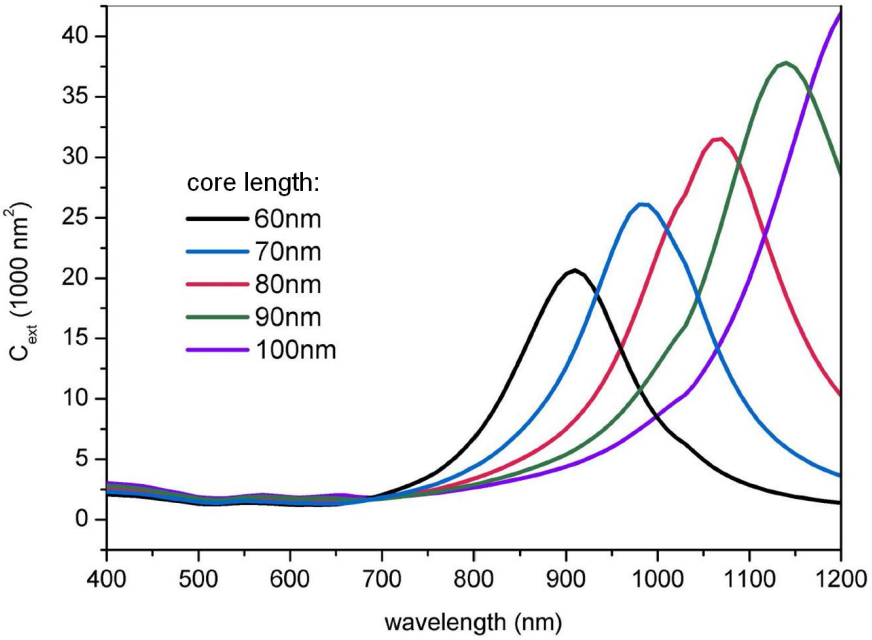

Figure 5.10.: Shift of the longitudinal plasmon peak resonance position of Co core / Au shell nanorods upon changes of the initial Co core length (diameter fixed at 6 nm) with a Au shell thickness of 5 nm.

thick Au shell, the dependence of the extinction on the orientation of the main nanocylinder axis to the direction of polarization is plotted in Fig. 5.11. As expected, the longitudinal plasmon peak height decreases with increasing angle. In comparison to plain magnetic nanorods (see Fig. 5.6), the extinction difference of parallel to perpendicular oriented particles at a wavelength of 1060 nm is much higher and amounts to about 31410 nm^2 (bare Co nanorods: 610 nm^2, i.e. an increase by a factor of > 50). The transversal plasmon resonance peak can be seen at about 510 nm.

The influence of a realistic Gaussian distribution of particle geometries on the longitudinal plasmon resonance peak is shown in Fig. 5.12. While the standard deviation of the length of the Co core has been determined experimentally using TEM imaging, the diameter can be set constant according to the narrow distribution obtained by the synthesis (see chapter 5.1.1). Assumptions have to be made for the expected but not yet experimentally achieved Au shell. A rather broad distribution is used for the Au shell compared to the Co core length. The quotient σ/μ of the standard deviation σ and the mean value μ amounts to 0.18 for the Au shell and to 0.07 for the Co core length. Ideal particles without geometry distribution are represented by the black line in Fig 5.12(a). By varying the Co core length (red line) only, no shift of the plasmon peak position is observed but a decrease of the peak height by about 14%. Upon a variation of the Au shell thickness, a shift of the plasmon peak wavelength occurs (shown by the blue line).

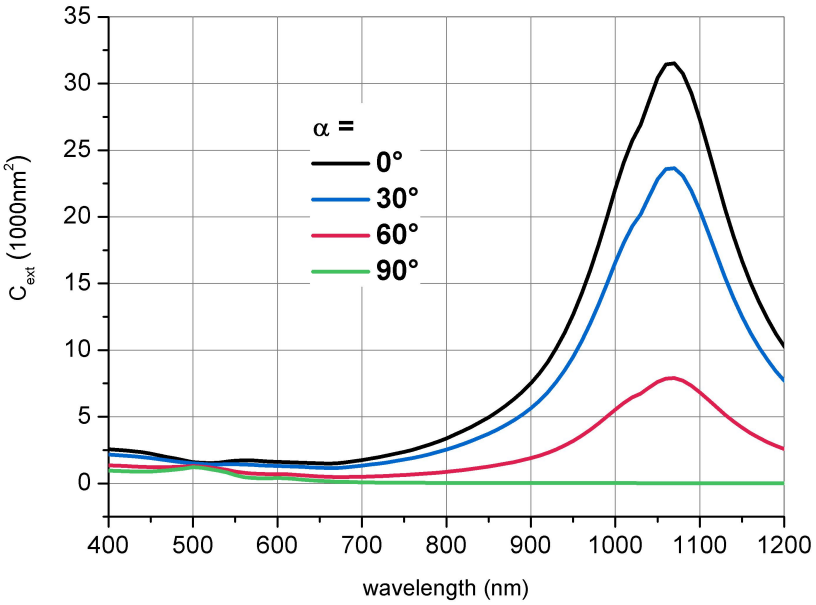

Figure 5.11.: Dependence of the extinction upon changes of the orientation of Co core / Au shell nanorods. Here, α denotes the angle between the nanocylinder's main axis and the direction of polarization and varies from parallel alignment ($\alpha = 0°$, black) up to a perpendicular one (green line). The core possesses a length of 80 nm and a diameter of 6 nm and is surrounded by a 5 nm thick shell.

The experimentally realistic case of a variation of both the Au shell thickness and the Co core length (green line) results in a peak shift of 26 nm towards smaller wavelengths. Furthermore, it results in a decrease of the peak height by approximately 27% and in an increase of the half width maximum from 190 nm to 280 nm relative to the ideal particles without geometry distribution. These facts have to be considered when experimentally realizing a PlasMag measurement (e.g. by adjusting the laser wavelength). Fig. 5.12(b) shows the relative abundances of the used particle geometry parameters in % that are used to create the curves in (a) by adding up the respective extinction spectra.[10]

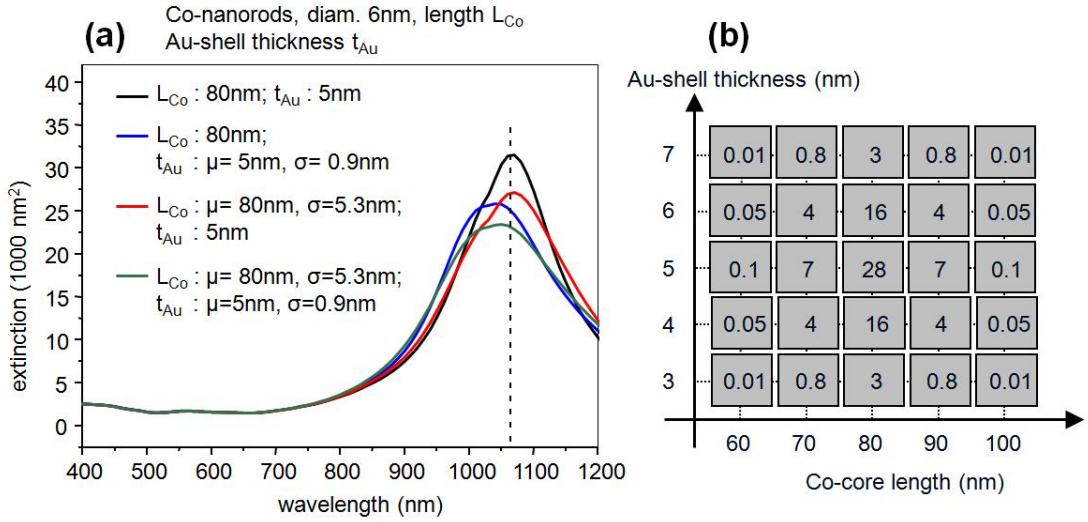

Figure 5.12.: (a) Influence of a realistic Gaussian distribution of particle geometry parameters on the longitudinal plasmon resonance peak (mean value μ, standard deviation σ). The black line corresponds to ideal particles without any geometry parameter distribution. Variations of the Au shell thickness (blue curve), the Co core length (red curve), and both the Au shell thickness and Co core length (green curve) are plotted. (b) Relative abundances of the used particle geometry parameters in %.[10]

Moreover, an additional coating with a biomolecular shell causes a shift of the peak wavelength position of the longitudinal plasmon resonance. This is illustrated in Fig. 5.13 for Au coated Co cylinders (core length 80 nm, core diameter 6 nm, 5 nm Au layer) with two different thicknesses of an assumed organic shell. Bare core-shell cylinders are represented by the black line, while the extinction spectrum for a 5 nm thick extra biomolecular layer is plotted in green, and the spectrum for an additional 10 nm thick layer is shown by the blue curve. The longitudinal plasmon peak is shifted into the infrared regime of light and increases in height by adding organic layers. This is of importance for the stabilization and functionalization procedure as well as for further binding of analyte molecules. Calculations are carried out with a real refractive index of the organic layer of 1.45 and under the

assumption of a dense homogeneous coating.[145]

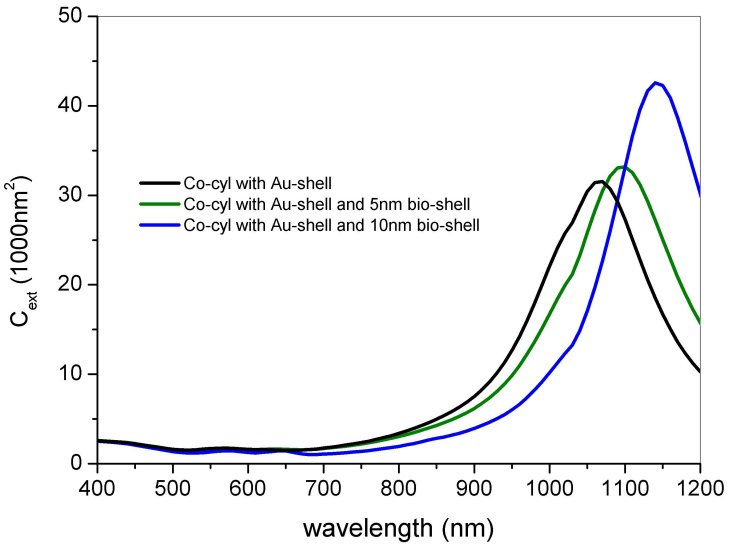

Figure 5.13.: Longitudinal plasmon resonance peak wavelength shifts of Au coated Co nanocylinders upon addition of a biomolecular shell (core length 80 nm, core diameter 6 nm, and 5 nm Au layer). Extinction spectra of a plain Co core / Au shell cylinder (black), after addition of a 5 nm (green) and of a 10 nm (blue) thick biomolecular shell.

Furthermore, additional simulations of the optical properties of other particle types have been carried out within the scope of this work at an early stage of the project to identify a whole set of suitable particle types. These have not been tested with the PlasMag method, but they represent possible alternatives to the noble metal shell coated Co core nanorods (the most appropriate particle type for the PlasMag measurement method). Alternative particle materials and geometries have always been chosen according to possible synthesis routes. Particle types of different collaborators have been tested for their applicability for the PlasMag measurement technique. A summary of those simulations is shown in Fig. 5.14 in a normalized plot. The blue line represents cylindrical particles with an overall length of 210 nm and a diameter of 40 nm composed of two different materials, namely Au and Co, which are arranged in three layers of equal length (two Au layers and one Co layer in between; synthesized in a nanoporous template based on electrochemical deposition techniques carried out at the University of Hamburg by the group of Kornelius Nielsch).[146–148] Commercially available Au nanorods (L=40 nm and d=20 nm, Nanopartz Inc.) encapsulated by a 5 nm maghemite shell (Fe_2O_3, synthesis at the Austrian Institute of Technology) are shown in red. The black line refers to the Co-particles from chapter 5.1.1, but instead of the

mixed Pt/Au shell presented there, a Pt coverage on the side walls and Au on the tips of the cylinder is assumed (the assumption is based on published as well as on unpublished preceding fabrication methods carried out by the INSA Toulouse).[149] Finally, the dark green line shows the extinction of a maghemite cylinder (L=580 nm, d=25 nm) surrounded by a Pt shell of 15 nm thickness (the shell does not cover the tips of the inner cylinder). The latter particle type can be synthesized by atomic layer deposition into nanoporous templates.[150] These simulations show that a wide range of different potential particle types can be characterized on their optical behavior by the DDA simulation method.

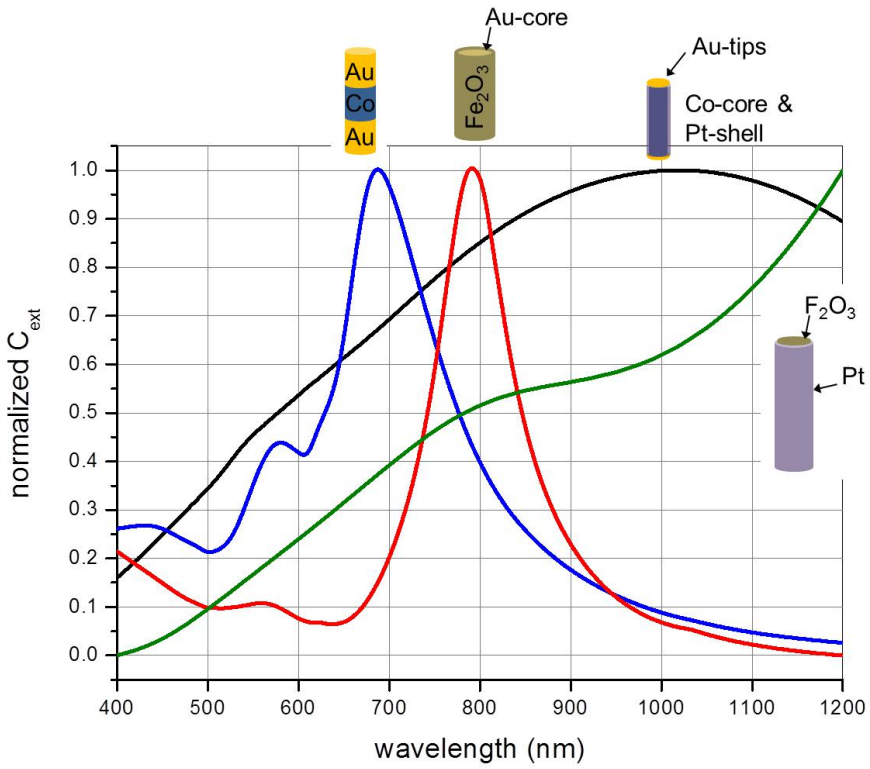

Figure 5.14.: Normalized extinction spectra of alternative particle types. The geometry and the materials are qualitatively illustrated in the figure while a more detailed description is given in the text.

In summary, the modeling of the optical properties serves as a useful tool to figure out nanorod dimensions and compositions, which are optimal for the PlasMag method. With regard to the wavelength position of the longitudinal plasmon peak (near-infrared regime) as well as to the expected optical signal strength. A particle type composed of a Co core with a diameter of 6 nm and a length of 80 nm coated by a Au shell of 5 nm thickness suits best the requirements for a successful PlasMag sensing. These dimensions act as target input for nanorod synthesis.

5.2.2. Magnetic Nanorod Property Modeling

Modeling of the magnetic properties of suitable nanorods is mainly accomplished regarding the characteristics presented in chapter 3.1, which includes the choice of magnetic material, size and geometry of the nanorods to obtain ferromagnetic particles with fixed magnetic moment direction. Modeling is used to determine the needed magnetic field strength to obtain a high degree of nanorod alignment within the solution, which is another important experimental parameter, especially for the design of the measurement setup.

For the Co nanorods presented in chapter 5.1.1, the magnetic crystal and shape anisotropies are parallel to each other and force the particles' magnetic moments to be directed along the main axes of the nanorods.[151] Thus, for typically encountered nanorod lengths, the magnetic anisotropy energy greatly exceeds the thermal energy and superparamagnetism can be neglected. For Co nanorods of 80 nm length, the Néel relaxation time (see equation 3.1 on page 22) is of the order of 10^{80} s at room temperature, which indicates that the magnetic moment is stable and fixed in its direction within the particle.

An ensemble of ferromagnetic nanoparticles behaves similarly to the magnetic domains in a bulk paramagnet. Therefore, it can be well described by the Langevin equation (see equation 3.41 on page 36),[33] which makes it possible to determine the degree of alignment with respect to the external magnetic field strength, the temperature, the specific magnetic material, and the size of the nanorods. Fig. 5.15 shows the degree of alignment of bare Co nanorods, under assumption of single domain particles, with a fixed diameter of 6 nm depending on the external field strength and the length of the nanorods as it can be varied within the synthesis procedure (see chapter 5.1.1). The temperature is set to 295 K. Obviously, the higher the field strength and the longer the particles are, the higher is the degree of alignment, which is attributed to the decreased temperature influences on larger particles and the influence of the external magnetic field interacting with the magnetic moment of the nanorod.

For example, for nanorods with a core length of 80 nm, an alignment ratio of about 75 % at a field strength of 5 mT is achieved. Thus, external magnetic field strengths up to 10 mT ensure a high degree of alignment (up to 88 %). The PlasMag measurement signal of an ensemble of particles reflects a superposition of all particle orientations, so that an increased alignment ratio results in an optimized signal.

5.2.3. Modeling of Nanorod Rotational Behavior and Biosensing Potential

Modeling of the rotational behavior of nanoprobes upon analyte binding is applied to gain additional information about required specifications of both the nanorod properties and the measurement setup as well as information about the biosensing potential of the PlasMag measurement technique.

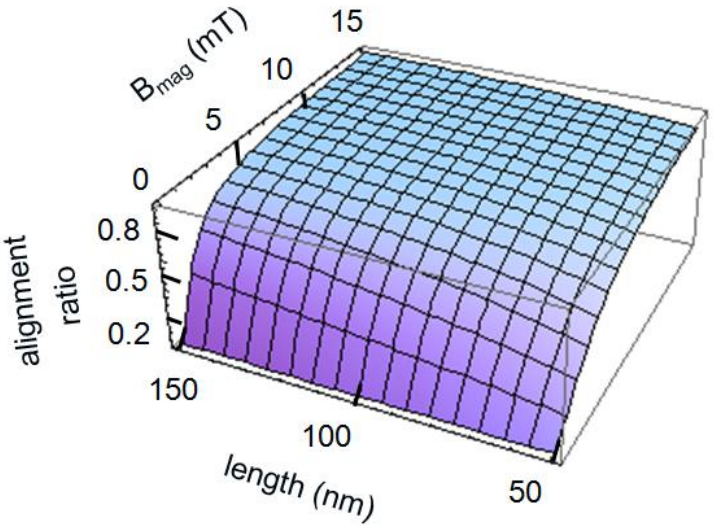

Figure 5.15.: Alignment ratio of dispersed Co nanorods in dependence of their core length and the applied external magnetic field strength B_{mag}.

Therefore, the model developed by Shliomis for particles within an external rotating magnetic field is applied (see equation 3.49 on page 37), which satisfyingly describes the measurement signal at the field strength and frequencies used in this chapter. For the here used field strengths and frequencies, the Shliomis model can be well applied. Fig. 5.16 shows the dependence of the phase lag on the Co core length as well as on the frequency of the applied external magnetic field for different shell thicknesses. As expected, the phase lag increases with increasing shell thickness. Here, bare Co nanorods are compared to Au coated nanorods, to nanorods possessing a Au shell and antibody (Ab) functionalization and to nanorods of different additional antigen (Ag) loadings. Under the assumption of an antigen of 5 nm length, an additional Ag shell thickness of 1 nm corresponds to an Ag loading of 20 %. The 60-80 nm Co core length particles show the maximum phase lag change upon binding of antigen (about 15° for a fully Ag coated nanorod) after comparing the phase lag of the Ag loaded nanorods to the functionalized nanorods and by calculating the phase lag difference. While the decrease of the phase lag difference for longer nanorods can be explained by a reduced relative change of the hydrodynamic volume upon coating with a constant shell thickness, the decrease for shorter nanorod lengths can be explained by a decreased alignment ratio due to the temperature influence (see chapter 5.2.2). Following parameters have been assumed for the calculations: Co with a bulk value of saturation magnetization of M_S of $1.44{\cdot}10^6$ A/m,[31] an external magnetic field magnitude of 1 mT at a frequency of 1 kHz, and water as medium with a viscosity of 1 mPa·s at 295 K. Fig. 5.16(b) shows the frequency dependence of the phase lag of particles with 80 nm core length and at a field strength of 1 mT,

again, which have the largest phase lag differences at frequencies of about 1 kHz.

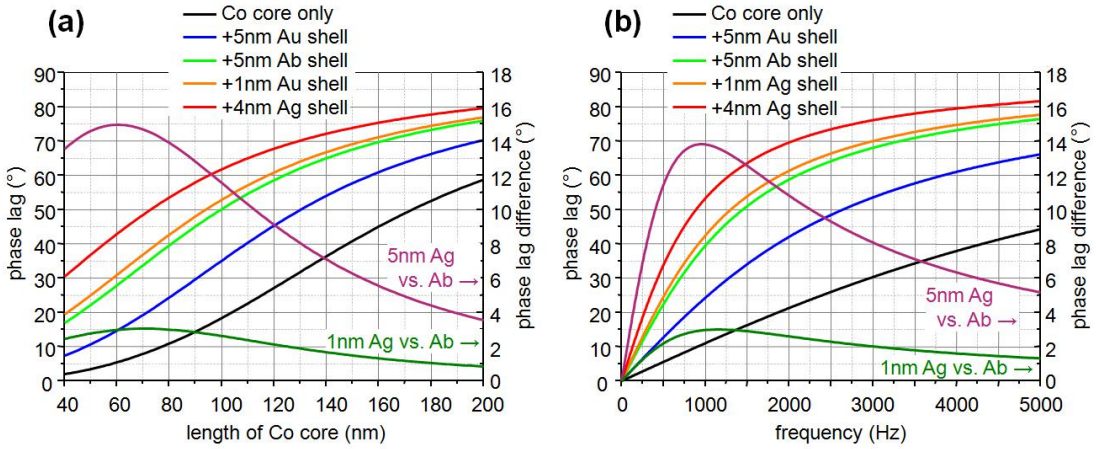

Figure 5.16.: Phase lag change upon addition of various shells. (a) Dependence of the phase lag on the Co core length for subsequent shell coating, starting with bare Co nanorods (black), Au coated nanorods (blue), antibody (Ab) functionalized nanorods (green), nanorods with 1 nm (20 % coverage) antigen (Ag) loading, and fully Ag coated nanorods (5 nm). Absolute phase lag values correspond to the left axis, while phase lag differences (Ab coverage vs. Ag loading) are indicated by the right axis. (b) Frequency dependence of the phase lag of particles with 80 nm core length with the same nanorod coating states as in (a).[10]

This means that nanorods with a Co core length of 80 nm can be used most effectively at an experimentally reasonable frequency in the lower kHz regime. Furthermore, antigen loading down to 20 % is measurable under the assumption of a homogeneous distribution of the analyte molecules translating into reduced analyte shell thickness.

5.3. Spectral Measurements in Static Magnetic Fields

Spectral measurements of bare Co nanorods have been carried out to prove the simulated dependence of the particle extinction on the angle between the polarization direction of the light and the long particle axis (see Fig. 5.6 in chapter 5.2). The reason for the angular dependence is the shape-dependent anisotropic polarizability.

In order to achieve a high alignment ratio of the magnetic nanorods, a homogeneous static magnetic field (15 mT magnitude) was applied parallel and perpendicular to the polarization direction of the incident light, and then, wavelength spectra were recorded. Additionally, spectra of randomly oriented particles in the

absence of an external field were measured. The instrumentation comprises a halogen lamp, a rotatable polarizing filter, and a spectrometer (Trax 550 spectrometer from JYHoriba). The spectra are corrected for a linear time dependence due to aggregation resulting in a precipitation of the magnetic particles. The employed nanorod batch consists of nanorods of 90 nm length at a concentration of 4 μg/ml (i.e. n=1.8·10^{17} particles/m^3) stabilized by HDA in toluene.[10]

Fig. 5.17 compares the measured spectra (solid lines) with the simulated spectra (dashed lines) for all three particle orientations with respect to the polarization direction. The transmission $T = exp(-nsC_{ext})$ depends on the extinction cross section C_{ext}, the particle concentration n, and the optical path length s (1 cm through the sample cuvette).[86] These transmissions have been calculated for parallel (T_{par}), perpendicular (T_{perp}), and random (T_{rand}) orientations. The latter is given by $T_{rand} = \frac{1}{3}(T_{par} + 2T_{perp})$ according to two degrees of freedom for the perpendicular orientation.[97] The DDA simulation method is used for the calculation of the respective extinction cross sections. Here, an additional 2 nm thick molecular shell with a refractive index of 1.5 has been included to take account of the HDA surfactant layer. The simulated curves and the measured spectra are in good qualitative agreement.[10]

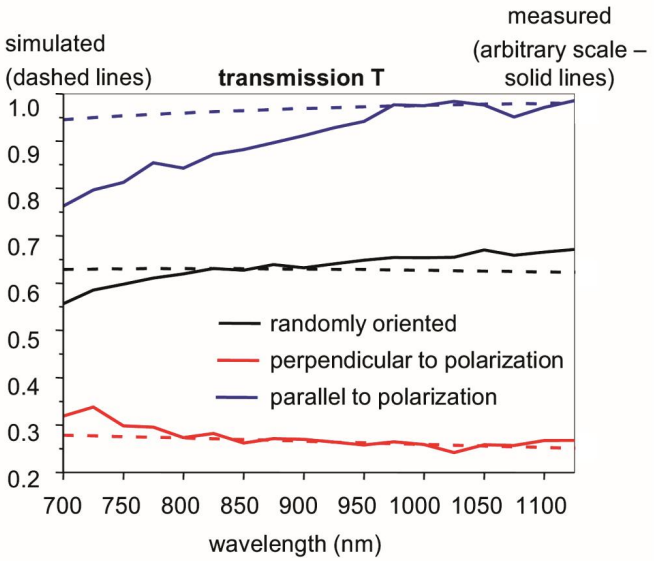

Figure 5.17.: Simulated and measured transmission spectra of Co nanorods in a static magnetic field for three different particle orientations with respect to the direction of polarization of the incident light. Simulated (dashed lines) and measured (solid lines) spectra are compared. Particle alignment is experimentally achieved by a static magnetic field of 15 mT magnitude.[10]

5.4. Measurements in Rotating Magnetic Fields

This chapter summarizes the main experimental results achieved with the PlasMag measurement setup and covers measurements in rotating magnetic fields of all types of nanoparticles presented in chapter 5.1. The structure of this chapter is composed in a systematic way of step-wise proving the measurement principle. It starts with measurements of bare Co nanorods in organic solvents. Furthermore, unspecific binding of protein to Ni nanorods will be presented and, finally, results of specific binding measurements using noble metal shell coated Co nanorods to detect streptavidin as well as the cancer biomarker sHER2 will prove the working principle of the PlasMag method.

5.4.1. Measurement Results of Bare Cobalt Nanoparticles

The first particles available, were bare Co nanorods, which are ideally suited as core material for the aspired core-shell nanorods as predicted by the modeling in chapter 5.2. Due to their shape-dependent anisotropic polarizability, which has been proven by measurements in static magnetic fields in chapter 5.3, these rods can be used for an optical detection of the rotational dynamics. This serves as a first experimental validation of the PlasMag measurement principle. The used particles are dissolved in organic solvents to prevent oxidation, which would result in changes of the magnetic characteristics. Agglomeration of the bare magnetic nanorods in solution is a critical point and will be discussed in the following. The employed particle batch consists of nanorods dissolved in tetrahydrofuran (THF) with lauric acid (LA) as ligand. The viscosity η of THF is 0.48 mPa·s and the particles' geometrical dimensions are 53 nm medium length and 6 nm medium diameter. Moreover, a 2 nm thick LA ligand shell can be assumed. The ideal particle length of 80 nm has not been achieved for the particle batch used here, but due to the lack of the noble metal shell (no plasmon resonances) and due to the fact that these particles are used to give an initial proof of the PlasMag concept, they can be well applied.

For the measurements presented here, the first setup shown in chapter 4 has been used. The model of Shliomis was used to describe the rotational behavior of bare Co nanorods (see equation 3.49 on page 37). Even though, this model has been further developed by Yoshida et al, it is justified to use Shliomis' model to describe the main characteristics of the rotational dynamics due to the problems regarding aggregation of the nanorod batch, which hinder the Yoshida model to substantially improve the interpretation of the measured data.

In Fig. 5.19(a) typical raw signals generated by the PlasMag setup are shown. The black line denotes the optical signal from the photodetector output while the red line represents the reference signal, which originates from the magnetic field. This signal is generated by the voltage drop across one coil of the Helmholtz coil pair indicative of the rotating magnetic field component parallel to the polarization axis of light (see also chpater 4.3). The phase lag of interest can now be illustrated

by a simple example under the assumption that the particles do not experience a drag torque and are rotating in phase with the field (see Fig. 5.18). In this case, they are oriented parallel to the direction of the polarization, when the magnetic field of the coil parallel to the polarization direction shows a maximum. Particles oriented parallel to the polarization show a maximum of extinction and, thus, a minimum in the transmission signal is obtained. Therefore, the time difference between the reference maximum and the minimum of the photodetector output corresponds to the phase lag of the nanorod's long axis orientation relative to the rotating external magnetic field.[10]

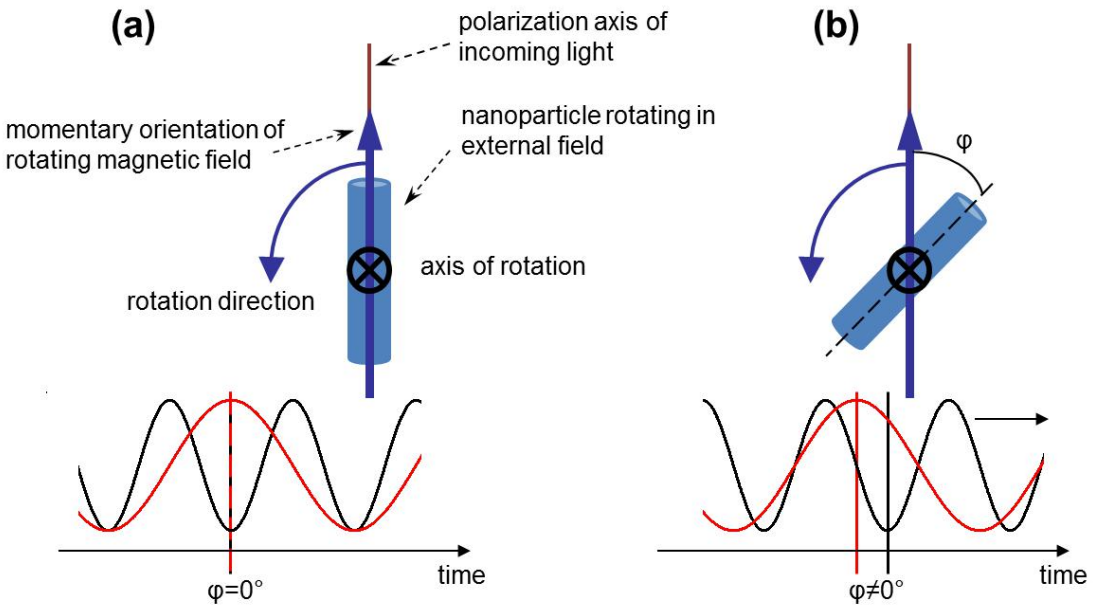

Figure 5.18.: Schematic illustration of the measured phase lag. (a) Particle without phase lag. The magnetic signal (red) of the coil parallel to the polarization axis is maximal and the particle aligned parallel to polarization, which results in a minimum of light transmission (black). (b) Particle with phase lag. The magnetic signal (red) is maximal, but the transmission signal (black) is shifted in time with the phase lag φ.

The phase lag is recorded with respect to the magnetic field frequency and magnitude. Measured phase lag spectra at three different external magnetic field magnitudes (1 mT, 2.5 mT, 5 mT) are shown in Fig. 5.19(b) in solid lines. It can be seen, according to the theoretical model, that the phase lag roughly follows an arctan dependence and that it decreases with increasing field strength due to an enlarged magnetic torque acting on the nanorods. Moreover, the optical signal is frequency doubled with respect to the magnetic signal according to the symmetry in particle geometry (see also chapter 4.3). However, the model calculations give smaller phase lags (dotted lines corresponding to the right axis in the graph). For

the model, particle geometry data determined by TEM imaging and Co with a bulk value of saturation magnetization of M_S of $1.44 \cdot 10^6$ A/m were used.[31] The reason for the deviation from the measured phase lag originates from the fact that the particles form agglomerates and that the measured signal corresponds to the rotating agglomerates. This is supported by alternative measurements of the mean hydrodynamic diameter by single particle tracking microscope measurements,[133] which result in hydrodynamic diameters of 310 nm assuming a spherical particle shape.[10]

An improved modeling considering also the particle aggregation is based on spherical agglomerates with a hydrodynamic diameter of 310 nm. Under the assumption of hexagonal close packed nanorods with a core diameter of 6 nm and a particle distance of 10 nm (i.e. rod diameter + 2 x 2 nm surfactant layer) the magnetic part of the volume amounts to about 1/3 of the overall hydrodynamic volume. This corresponds to a magnetic core volume with a diameter of about 213 nm. By assuming hexagonal packed magnetic nanorods, the magnetic moments of neighboring rods will almost compensate each other (see Fig. 3.4 in chapter 3.1). Dumestre et al. report on the lowered magnetic moment due to a self organization of a comparable nanorod batch.[60] Therefore, additionally to assuming particle agglomerates, the magnetic moment has to be lowered accordingly. By reducing the magnetic moment of such an agglomerate by a factor of 1000, the calculated phase lag values show qualitative agreement with the measurement data.[10]

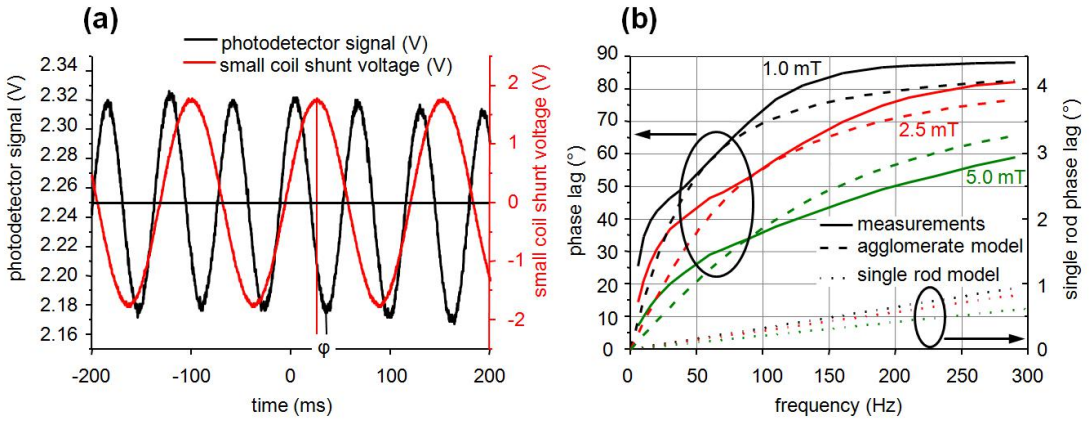

Figure 5.19.: PlasMag measurement results on bare Co nanorod solutions in an external rotating magnetic field. (a) Typical raw PlasMag signal comprising the reference signal (red line) and the frequency doubled optical signal (black line). The reference signal corresponds to one component of the rotating magnetic field, while the optical signal is the measured transmission detected by the photoreceiver. (b) Recorded phase lag spectra for three different field magnitudes (solid lines) and modeled phase lag spectra. The single particle model (dotted lines) and the agglomeration model (dashed lines) are compared.[10]

The reason for the strong formation of agglomerates is the synthesis procedure,

which involves repeated drying and washing steps that bring the particles into close contact. Even by using strong ultrasound sonication, these agglomerates cannot be separated. By the improved fabrication method without drying steps resulting in noble metal shell coated nanorods, aggregational problems can be avoided and single particle dispersions can be obtained, which will be shown later in chapter 5.4.3.

5.4.2. Measurement Results of Bare Nickel Nanoparticles

Ni nanorods synthesized as described in chapter 5.1.2 offer the advantage of being stabilizable in aqueous solution as single particle dispersions. Phase lag measurements of Ni nanorods in rotating magnetic fields have also been presented by Guenther et al.[142] As the functionalization of these particles is challenging due to the almost unreactive PVP on the particle surface and as the particle stability depends very sensitively upon changes of the pH and upon the ionic strength of the solution, the Ni nanorods are hardly applicable to specific binding experiments. Nevertheless, Ni nanorods can be used for the detection of unspecific protein binding, and therefore, prove that upon binding of target molecules, the measurement signal changes and an increased phase lag is obtained in the measured spectra.

Binding experiments of BSA to the surface of the nanorods are presented in the following paragraphs and give a good proof of the overall measurement principle. Additionally, the amount of bound protein has also been validated by measurements of the electrophoretic mobility of particles with and without adsorbed BSA. Upon protein binding, the surface charge density and, subsequently, the electrophoretic mobility changes, which allows an estimation of the amount of bound molecules.

Protein Detection Measurements

Phase lag spectra of Ni nanorod samples without BSA are compared to spectra of samples with BSA protein in Fig. 5.20. According to theory, the phase lag increases under the presence of BSA protein, which is due to the adhesion of the protein onto the surface of the Ni nanorods that results in an increased hydrodynamic volume. Along with measured phase lag spectra, Fig. 5.20 shows fits to the experimentally obtained data using the empirical Yoshida model (see chapter 3.3).

BSA with a molecular weight of 66.5 kDa (purchased from Sigma-Aldrich) is added at a concentration of 128 nM and the used Ni nanorod concentration amounts to 10 pM ($6{\cdot}10^9$ particles/ml). On the one hand, the surface layer of the Ni nanorods becomes oxidized in aqueous media, which results in a positive surface charge under slightly acidic pH conditions (see equation 3.3 on page 23). On the other hand, the BSA protein molecule can be modeled as a prolate ellipsoid with dimensions of 14 nm x 4 nm and an electric charge gradient along the main axis with an overall negative charge for the used solution.[152] Thus, it

can be assumed that the small area of the protein's cross section points toward the nanorod surface (upright oriented binding) with the result that the amount of used BSA is sufficient for at least five times full coverage of the nanorods, if hexagonal dense packing of the protein is expected. Effects related to a change of the sample viscosity upon protein addition can be neglected, as measurements with a micro-viscometer did not reveal viscosity changes within a resolution of 1% of the measured value.[11]

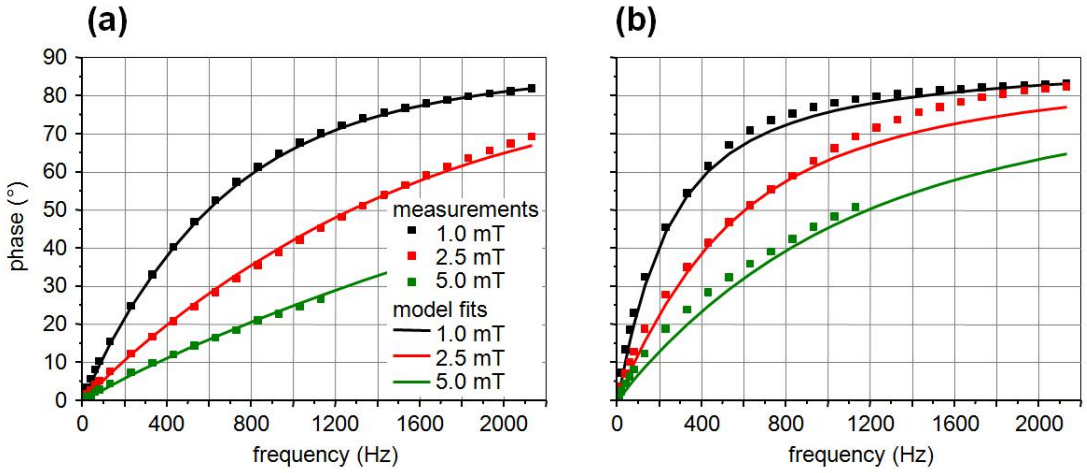

Figure 5.20.: Phase lag spectra of Ni nanorod dispersions without and with addition of BSA protein. Frequency phase lag spectra are recorded at three different field magnitudes. (a) Without addition of BSA. (b) After BSA addition at a concentration of 128 nM. Measured data (dots) is fitted by calculated phase spectra (solid lines).[11]

The model fits include integration over Gaussian distributions of the plain nanorod parameters (length, diameter, and magnetic moment) and the main free parameter for fitting, which is the hydrodynamic shell thickness. This shell is the sum of the PVP surfactant layer, the stagnant surface layer of immobile fluid, and a layer of adhered target proteins on the nanorod surface. While the geometric nanorod parameters (mean values and standard deviation of the length and the diameter) are determined by TEM imaging (see Fig. 5.5), the magnetic moment is deduced from VSM measurements (see chapter 5.1.2). Good model fits were obtained by reducing the magnetic moment by 20 % to a value of $3.0 \cdot 10^{-17}$ Am^2. The reason for the reduction of the magnetic moment is that the VSM measurements were carried out three weeks prior to the PlasMag measurements and that Ni experiences a progressing surface oxidation. A decrease of the magnetic volume of the Ni nanorods by 20 %, corresponds to a surface oxide layer of about 1.3 nm thickness, which agrees to reported values in the literature.[153] A standard deviation of the magnetic moment of $2.1 \cdot 10^{-17}$ Am^2 for the best fit manifests itself in the curvature of the phase lag spectra. The hydrodynamic shell thickness

extracted from the fitting procedure as the free parameter is 12±8 nm for bare Ni nanorods and 34±24 nm after BSA addition. Thus, the addition of BSA results in an increase of the mean hydrodynamic shell thickness of 22 nm. Regarding the dimensions of the BSA molecule and its polarity, as mentioned above, this increase represents a reasonable value. The remaining difference can be attributed to an increase of the stagnant surface layer of immobile fluid.[11]

Fig. 5.21 shows phase lag spectra of Ni nanorods with and without addition of BSA for a single field strength of 1 mT. Absolute phase lag values of Ni nanorods are shown in black (without BSA) and grey (with BSA) and the relative phase difference is shown in blue and corresponds to the right axis. Phase differences of approximately 22° are obtained at an external magnetic field frequency of 330 Hz. Therefore, protein binding can be easily detected by the PlasMag measurement method.

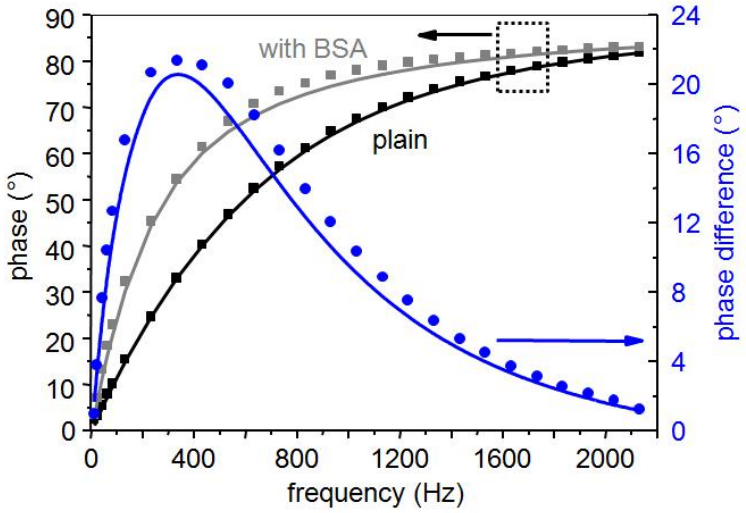

Figure 5.21.: Phase spectra of Ni nanorods with and without addition of protein at an external magnetic field amplitude of 1 mT and corresponding relative phase difference. The dots represent measured values, while the lines correspond to the calculated fits. The relative phase difference (blue) reaches a maximum value of about 22° at a frequency of 330 Hz.

Determination of bound BSA amount by electrophoretic mobility measurements

The amount of bound protein to the surface of the employed Ni nanorods has been evaluated independently by measuring the electrophoretic mobility of nanorods with and without adhered protein. Therefore, a commercial Zetasizer has been used (Malvern Zetasizer Nano ZS, Model ZEN3600). All samples were washed prior to the measurements and redispersed in ultrapure water to remove unbound

protein. The washing procedure involved a magnetic separation of the particles from the solution by using a small permanent magnet. Electrophoretic mobility measurements of 6 samples (three each with and without BSA) have been carried out. The results presented here, reflect the calculated mean values. Mobility values of 2.71·10^{-8} m^2/Vs for bare Ni nanorods and -1.05·10^{-8} m^2/Vs for Ni nanorods with bound BSA have been determined. The change of the sign of the mobility values upon BSA addition already indicates protein binding.[11] The Debye length $1/\kappa$ (see chapter 3.1) is experimentally determined from the ionic strength (IS) of the sample solution (see equation 5.1), while the ionic strength itself follows from the measured conductivity of the sample solution. The conductivity Λ amounts to about 2.0 μS/cm for all measured samples, which indicates a successful washing of the nanorod dispersions. The ionic strength can be calculated under the assumption of a small salt concentration by $IS[\mu M] \approx 9.3 \cdot \Lambda[\mu S/cm]$.[154] This results in Debye lengths for both samples of about 70 nm.

$$\kappa^{-1}[nm] = \frac{9.6}{\sqrt{IS[mM]}} \tag{5.1}$$

The product of the inverse Debye length κ and the hydrodynamic particle radius R determines the model that can be used for interpreting electrophoretic mobility measurements and calculating the zeta potential. The radius R corresponds to the distance from the center of the particle to the slip plane boundary (see chapter 3.1 and Fig. 3.5 for more details on the zeta potential). For cylindrical particles, this is the hydrodynamic particle radius and corresponds to the sum of the magnetic core radius and the additional hydrodynamic shell thickness.[155] Therefore, the product κR amounts to 0.36 for Ni nanorods without protein (R = 13 nm + 12 nm) and 0.67 for Ni nanorods with bound protein (R = 13 nm + 34 nm).

The geometry of the used nanorod has to be considered for calculating the zeta potential from measured electrophoretic mobilities. A model that can be used here, was developed by Ohshima[155] and is valid for all values of the κR product and, for an arbitrary orientation of the nanorods during the measurement. This model will be discussed in more detail in the following paragraphs.[11]

For cylindrical particles aligned perpendicular to the applied electric field, the electrophoretic mobility μ can be expressed as[156,157]

$$\mu = \frac{\epsilon_r \epsilon_0}{\eta} \zeta f(\kappa R) \tag{5.2}$$

with the Henry function $f(\kappa R)$ which is given by[155]

$$f(\kappa R) = \frac{1}{2}\left[1 + \frac{1}{\left(1 + 2.55/\left[\kappa R\left(1 + exp(-\kappa R)\right)\right]\right)^2}\right], \tag{5.3}$$

where ϵ_r (78.5) is the relative permittivity, ϵ_0 is the permittivity of vacuum with a value of 8.854·10^{-12}, η is the fluid viscosity, ζ denotes the zeta potential, κ the inverse Debye length and R the cylinder radius. The Henry function is valid for all values of the product κR and for low zeta potentials.[155]

For an arbitrarily oriented cylinder, the mobility averaged over a random distribution of orientations is of the form:

$$\mu_{av} = \frac{1}{3}\mu_{par} + \frac{2}{3}\mu_{perp}, \tag{5.4}$$

with μ_{par} the mobility for parallel orientation of the cylinder to the electric field and μ_{perp} the mobility for perpendicular alignment.[158] This can be expressed with Henry's function as[155]

$$\mu_{av} = \frac{\epsilon_r \epsilon_0}{3\eta}\zeta\left(1 + 2f(\kappa R)\right). \tag{5.5}$$

Inserting the values of κ, R, and the measured mobility μ_{av}, mean zeta potentials ζ of +55 mV for bare Ni nanorod samples, and -21 mV for BSA coated nanorod samples are obtained. As mentioned above, the Ni nanorods possess a thin oxide layer on their surface. Nickel oxide has a point of zero charge (see equation 3.3 in chapter 3.1) at a pH value of about 8, which is above the pH value of the used Ni nanorod sample solution ($pH = 5.4$).[159] Therefore, positive values of the zeta potential are reasonable.[11]

The surface charge density for cylindrical particles can be deduced from the zeta potential.[160] In general electrolyte solutions, the surface charge density of a cylindrical particle is given by

$$\sigma = \frac{\epsilon_r \epsilon_0 \kappa k_B T}{e} I, \tag{5.6}$$

with the Boltzmann constant k_B, the temperature $T = 295$ K, the elementary electric charge e, and a factor

$$I = 2\ \sinh\left(\frac{y_s}{2}\right)\left[1 + \left(\frac{1}{\beta^2} - 1\right)\frac{1}{\cosh^2\left(y_s/4\right)}\right]^{\frac{1}{2}}, \tag{5.7}$$

where

$$\beta = \frac{K_0(\kappa R)}{K_1(\kappa R)}, \tag{5.8}$$

which depends on modified Bessel functions $K_n(z)$ of the second kind of order n.[160]

Furthermore, the scaled potential y and the scaled surface potential y_s are of the form:[160]

$$y = \frac{e\psi}{k_B T} \tag{5.9}$$

and

$$y_s = \frac{e\psi_s}{k_B T}. \tag{5.10}$$

The electrical potential at a certain radial distance r is $\psi(r)$ and the potential on the particle surface ψ_s.[160]

Applying equation 5.6 results in surface charge densities at the slip plane of $+1.23 \cdot 10^{-3}$ C/m^2 for Ni nanorods without bound BSA, and $-0.28 \cdot 10^{-3}$ C/m^2 for BSA coated nanorods.

The number of elementary charges on the particle surface is

$$n = \frac{\sigma A}{e}, \tag{5.11}$$

with A denoting the particle surface area, and amounts to +280 for a bare nanorod, and to -150 for a protein coated nanorod. Therefore, the mean change upon protein binding in elementary charge per nanorod equals to a number of 430.

According to literature, every BSA molecule carries a mean charge of -3.4 at the used pH value of 5.4.[161] Therefore, a mean number of bound protein molecules can be calculated from the above mentioned change in overall surface charges upon protein binding. This value amounts to approximately 130 and corresponds to a protein surface density of 5.8 fmol/mm^2, which is reasonable compared to values of bound BSA densities on various surfaces reported in the literature ranging from 0.8 fmol/mm^2 to 54 fmol/mm^2.[11,162,163]

5.4.3. Measurement Results of Noble Metal Coated Cobalt Nanoparticles

While a basic proof-of-concept of the PlasMag detection principle was already demonstrated for direct protein adhesion onto Ni nanorods (see chapter 5.4.2), these types of nanoparticles only served as an intermediate solution, as the targeted nanoprobes were not available at that time. With the successful water-stabilization and functionalization of noble metal coated Co nanorods described in chapter 5.1.1, final proof-of-concept work on the desired nanoprobes could be executed.

In this chapter, stability measurements of these nanorods in different buffer solution concentrations as well as stability measurements over time are presented. Furthermore, the results of biotin-streptavidin model assays and the results of measurements on the detection of sHER2 by Herceptin-functionalized nanorods are discussed.

Stability Measurements

By measuring the transmission over time of the polymer coated nanorods dispersed in differently concentrated phosphate buffered saline (PBS) buffer solutions at a wavelength of 600 nm (Nicolet Evolution 100 UV-Visible Spectrophotometer), it was observed that the dispersion is stable even if the nanoparticles are dispersed in salt containing buffer solutions. In Fig. 5.22, the measured transmission and the calculated particle concentration are plotted for three different solvents (water, 15 mM PBS, 150 mM PBS). Here, particle dispersions with an initial concentration of 20 μg/ml are examined over time until the measured transmission values indicate

a stable dispersion. The used PBS buffer solution has been purchased from Sigma-Aldrich (150 mM sodium phosphate and 150 mM NaCl) and diluted with ultrapure water. Initial calibration curves with dilutions of known particle concentrations have been carried out prior to the measurements over time. For particles dispersed in water or in a low concentrated (15 mM PBS) buffer solution, stability is reached within a short time compared to particles dispersed in a high concentrated buffer solution (150 mM), where agglomeration and sedimentation can be observed for a long period. A first initial increase in transmission, and therefore, a drop in particle concentration has always been observed and can be attributed to a small amount of particles within the solution that suffer from poor stability caused by variations of the quality of the polymer coating.

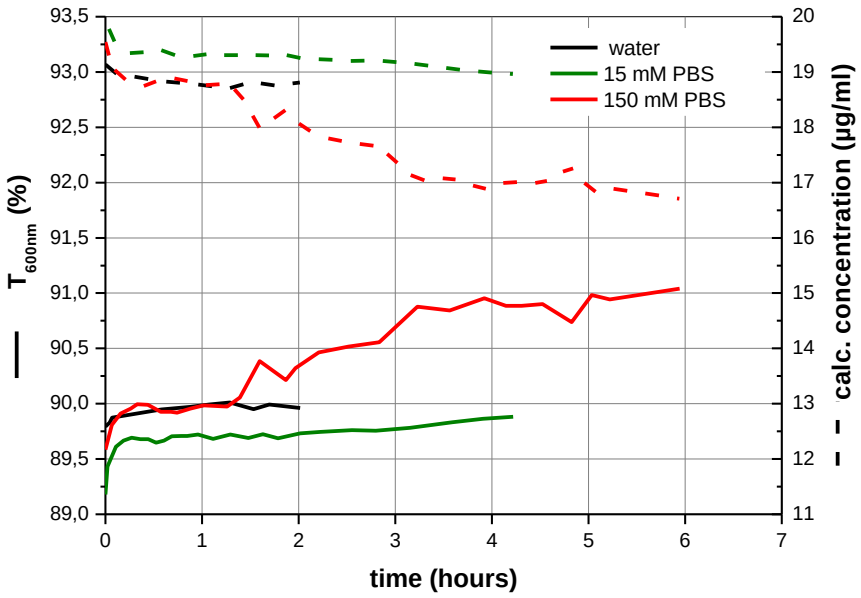

Figure 5.22.: Measured transmission at 600 nm and calculated particle concentration for polymer coated particles in water, 15 mM PBS and 150 mM PBS over time. The initial particle concentration amounts to 20 μg/ml.

Similar results are obtained by measurements in rotating magnetic fields for particles dispersed in low concentrated buffer solutions and are presented in Fig. 5.23. Here, the magnitude of the signal measured by the PlasMag platform at a magnetic field strength of 5 mT and a frequency of 1130 Hz serves as an indicator for the stability of the dispersion. A particle concentration of 10 μg/ml dispersed in three different solvents (water, 1 mM PBS, 13.5 mM PBS) has been examined and stable values were observed after a few hours. Agglomeration and sedimentation leading to a decrease of the measurement magnitude is observed in the first hours. These measurements refer to the amplitude of the signal, which

is correlated to the particle concentration. However, the main measurement parameter for the PlasMag method is the phase lag in a rotating magnetic field, and this value is stable within the observed measurement time. Thus, only the particle concentration is affected by the ion containing buffer solution. For particles stored more than 10 hours in buffer solution, saturation of the observed stability effects is obtained, so that PlasMag measurements using the phase lag as the measurement signal can be carried out under the assumption of a decreased particle concentration.

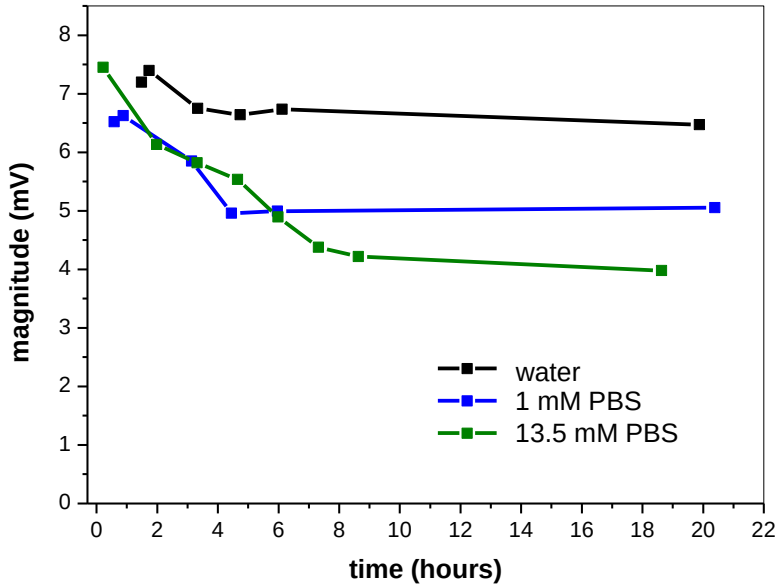

Figure 5.23.: Measured magnitude by the PlasMag setup at a field strength of 5 mT and a frequency of 1130 Hz for polymer coated particles in water, 1 mM PBS and 13.5 mM PBS over time. The initial particle concentration amounts to 10 μg/ml.

Good long-term stability of the nanorod dispersions in water obtained by the amphiphilic polymer approach is demonstrated in Fig. 5.24. Here, measurements by the PlasMag setup in rotating magnetic fields at a particle concentration of 100 μg/ml are shown. Phase lag spectra of the same nanorod dispersion are recorded at four different dates. The phase lag traces agree to each other within a maximum absolute variation of less than two degrees even after more than eight weeks of exposure to the aqueous solvent, which shows both the protective nature of the noble metal shell against oxidation of the magnetic core and the stability of the dispersion against agglomeration.

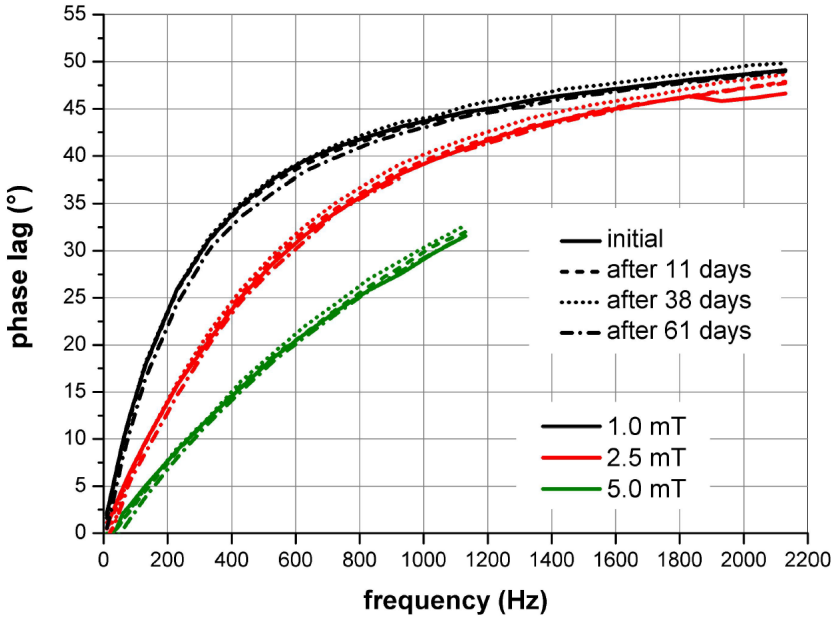

Figure 5.24.: Phase lag spectra of an aqueous dispersion of polymer coated nanorods (100 μg/ml) measured at different time intervals in rotating magnetic fields of different field strengths.

Biotin-Streptavidin Assay

Following a biotinylation of the nanoprobes, biotin-streptavidin model assays were executed. Results obtained by the PlasMag setup are shown in Fig. 5.25. Here, two sample solutions containing biotin-functionalized noble metal coated Co nanorods dispersed in water are measured in parallel at certain time intervals. The y-axis displays the measured change in phase lag of the nanorods with respect to their initial phase lag value (approximately 35° at 1 mT and 1130 Hz). At certain times (indicated by the arrows), drops of different volumes containing streptavidin protein are added, so that the overall streptavidin concentration amounts to 33 nM and 179 nM after each drop addition. At the same time, the particle concentration is lowered and decreases from initial 460 pM to 452 pM and finally to 412 pM. The streptavidin protein, purchased from Sigma-Aldrich with a molecular weight of about 60 kDa, is dissolved in PBS buffer, so that with each drop a small amount of PBS is added as well. The final concentration of PBS amounts to 20 μM and 110 μM respectively. In order to keep the volume of the reference sample equal, PBS-buffer drops without streptavidin are added to the reference sample at the same times. The table in Fig. 5.25 gives the respective sample volume (vol.), nanorod concentration (NR) and streptavidin concentration (Str.) before and after each added drop. While the phase lag of the reference trace changes stochastically within a maximum range of less than two degrees (corresponding

to the measurement uncertainty), the sample trace shows an increasing phase lag for each streptavidin drop addition and reaches a maximum phase lag change of about 5°.

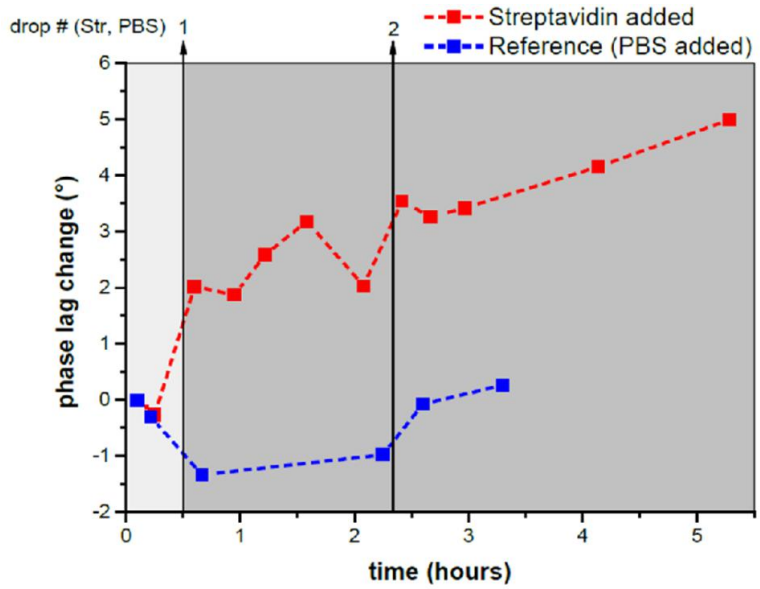

drop #	vol. (µl)	NR (pM)	Str. (nM)
	500	460	-
1	510	452	33
2	560	412	179

Figure 5.25.: Biotin-Streptavidin binding assay results. Phase lag change of biotinylated nanoparticles after addition of streptavidin. Two sample solutions of biotin-functionalized particles are measured in parallel over time and under addition of streptavidin or pure PBS buffer solution respectively (drop addition indicated by the arrows). The shown table gives the respective sample volume (vol.), nanorod concentration (NR) and streptavidin concentration (Str.) before and after each added drop.

These results demonstrate the concept of the PlasMag approach and serve as a first proof of specific binding.

Herceptin-sHER2 Assay - Measured Rotational Dynamics

The final proof of concept is the conduction of the assay for the detection of sHER2 protein as an important cancer biomarker of metastatic breast cancer (see chapter 2). Recombinant human sHER2 was purchased from eBioscience. Nanoprobes with Herceptin functionalization were prepared to specifically bind the sHER2 antigen (see chapter 5.1.1 for details on the functionalization procedure).

Following initial binding tests, PBS buffer was replaced for the sHER2 assay by TBS (Tris-bufferd saline) buffer solution with 25 mM Tris and 150 mM NaCl at a pH of 7.4 (chemicals purchased from Sigma-Aldrich), which leads to a higher assay sensitivity in comparison to PBS. Fig. 5.26 shows a characterization of nanoprobe dispersions for an applied external magnetic field strength of 5 mT.

Phase lag spectra of nanoprobes before (black markers) and after (red markers) functionalization with Herceptin antibodies are presented. Results of a following addition of large amounts of BSA as unspecific binding control are represented by the green markers. Finally, an amount of sHER2 protein sufficient for saturation of the antibody binding sites (positive control using sHER2 protein) is shown by the blue markers. Measured data is compared to corresponding fits (lines) according to the empirical model of Yoshida et al, described in chapter 3.3. Clearly, the phase lag of the nanorods with respect to the applied rotating magnetic field increases with the binding of both Herceptin antibodies and sHER2 antigen.

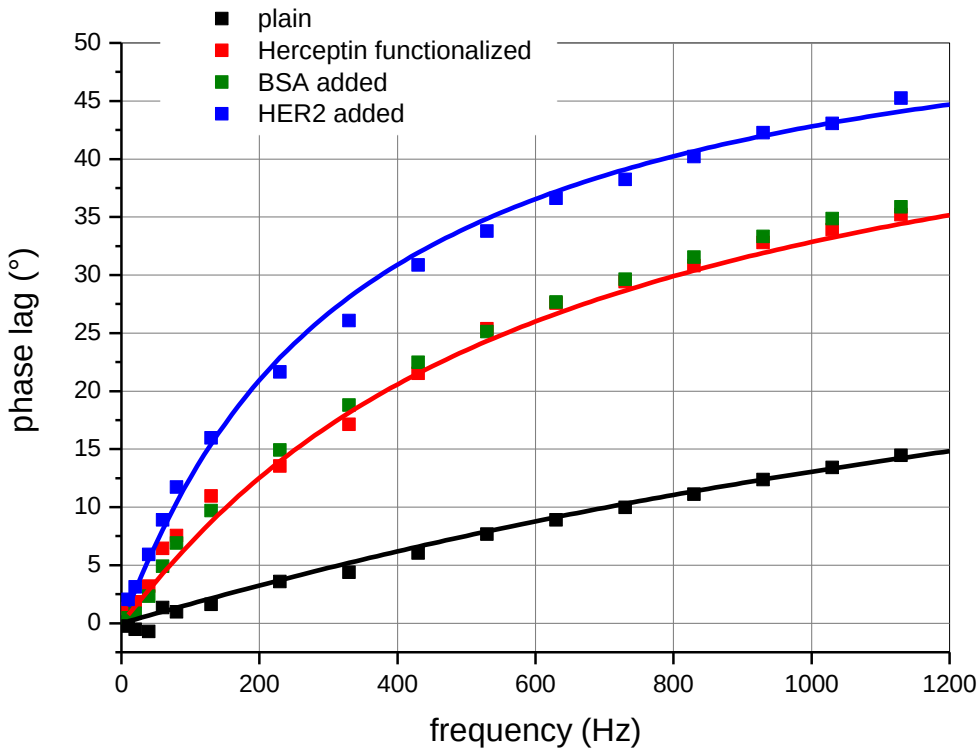

Figure 5.26.: Phase lag spectra (5 mT magnitude) of Co core / noble metal shell nanoprobes at a particle concentration of 10 μg/ml (about 240 pM). The black dots correspond to only PMA-coated nanoprobes in buffer, while the red dots show the frequency behavior of Herceptin-functionalized nanoprobes. Green dots represent measurements of functionalized particles after addition of a high amount of BSA (15 μM) which does not change the signal, while the blue dots show measurements of Herceptin-functionalized nanoprobes with added BSA (15 μM) and 200 nM sHER2

Herceptin-sHER2 Assay - Data Fitting Procedure

Data fitting is executed in a two-stage fitting procedure, which is schematically shown in the flow chart in Fig. 5.27. A detailed discussion of the individual steps of the fitting procedure is given in the following paragraphs. All values derived via the fitting procedure are summarized in the tables in Fig. 5.28. The table in Fig. 5.29 shows only those parameters, which are characteristic for the Herceptin functionalization and a full loading of the nanoprobes with sHER2. For the here presented fit procedure, a Gaussian distribution of the used particle parameters is applied with mean values μ and standard deviations σ.

For an interpretation of the observed rotational dynamics, an additional hydrodynamic shell is assumed. Realistic parameters for the polymer coating, that can be used for describing the PlasMag measurements, can only be obtained with particles in solution. Due to the lack of a reliable and comparable measurement method, it is best to use physical parameters derived by TEM imaging of the plain nanorods as basis for the fitting and not to determine the geometry parameters after the polymer coating. As the geometry of the Co core nanorods is more homogeneous than the one of noble metal coated particles, it is advantageous to use the bare Co nanorods as starting point for the determination of the geometry parameters. This means that the hydrodynamic shell includes the noble metal shell, the polymer coating and the stagnant surface layer of immobile fluid. The mean length μ_L^{TEM} of the Co core particles is 52 nm and the mean diameter μ_d^{TEM} is 5 nm, while the particle's magnetic moment μ_m^{TEM} can be calculated by the volume of the magnetic nanorod and the saturation magnetization of Co ($M_S = 1.44{\cdot}10^6$ A/m)[31] and amounts to $1.49{\cdot}10^{-18}$ Am^2. Oxidation and subsequent reduction of the magnetic moment of the Co core can be excluded due to the long term particle stability in aqueous solution measured before (shown in Fig. 5.24). By proceeding this way, the mean values for the length, the diameter and subsequently the magnetic moment are determined independently by TEM.

In the first fitting step, the hydrodynamic shell thickness $\mu_{t^{hydro}}$ is added to the mean values of the geometry parameters derived by TEM to obtain a mean hydrodynamic length μ_L^{hydro} and diameter μ_d^{hydro} (see equations 5.12 and 5.13). Particle agglomeration, which originates from the noble metal shell and the PMA coating procedures, is considered via the standard deviations of the hydrodynamic length, the hydrodynamic diameter and the magnetic moment. The same accounts for inhomogeneities of the noble metal shell and the PMA coating, which lead to a particle degradation over time. Therefore, the standard deviations that are derived from the fitting procedure for the length σ_L^{hydro}, the diameter σ_d^{hydro} and the magnetic moment σ_m^{hydro} are much higher than expected from the TEM analysis. The standard deviation of the additional hydrodynamic shell thickness is included in the standard deviations of the other parameters.

$$\mu_L^{hydro} = \mu_L^{TEM} + 2\mu_{t^{hydro}} \tag{5.12}$$

$$\mu_d^{hydro} = \mu_d^{TEM} + 2\mu_{t^{hydro}} \tag{5.13}$$

Fits are executed for the phase lag spectra of PMA covered nanoparticles dispersed in TBS buffer solution measured at three different magnetic field strengths of 1, 2.5 and 5 mT. This results in a mean hydrodynamic particle length of μ_L^{hydro}=63±45 nm, a mean hydrodynamic particle diameter of μ_d^{hydro}=16±6 nm, and a mean magnetic moment of μ_m^{hydro}=1.49±0.85·10^{-18} Am^2. Therefore, the additional hydrodynamic shell thickness $\mu_{t^{hydro}}$ after the PMA coating amounts to 5.5 nm. This is a reasonable value, as the shell comprises the noble metal shell (about 1.8 nm, see chapter 5.1.1), the surfactants (HDA and LA, with a chain length of the longer HDA of about 2 nm according to the chemical formula $CH_3(CH_2)_{15}NH_2$ and the mean carbon-carbon bond length[164]), the PMA polymer shell (interlocking with the surfactant chains), and the stagnant surface layer of immobile fluid due to the ions present in the solution. The free parameters for this first fitting step are the mean value of the hydrodynamic shell thickness $\mu_{t^{hydro}}$ and the standard deviations of the hydrodynamic length σ_L^{hydro}, the hydrodynamic diameter σ_d^{hydro} and the magnetic moment σ_m^{hydro} (i.e. 4 free parameters, see Fig. 5.27 and Fig. 5.28).

In the second step of the fitting procedure, the measured phase spectra of Herceptin functionalized and fully antigen coated nanoprobes are fitted at 5 mT external magnetic field strength (see Fig. 5.26 for the measurements and Fig. 5.27 for the fitting procedure). Here, the parameters derived from the first fitting step are used as a basis and an additional shell thickness t^{bio} consisting of the antibody and the antigen respectively is assumed (see equations 5.14 and 5.15). Therefore, the second fitting step involves only two free fitting parameters, which are the mean value $\mu_{t^{bio}}$ and the standard deviation $\sigma_{t^{bio}}$ of the additional hydrodynamic shell thickness (see Fig. 5.27 and Fig. 5.28). Additional shell thicknesses of $\mu_{t^{Herceptin}}$=15±9.5 nm for Herceptin functionalized nanoprobes and $\mu_{t^{sHER2}}$=25±13 nm for antigen coated nanoprobes are obtained. This is an increase in shell thickness by a factor of 1.67 upon binding of antigen molecules. The average molecular weight of Herceptin is 146 kDa,[165] while the average molecular weight of the used sHER2[166] is 87 kDa, so that the increase in weight amounts to 1.68, which fits well to the increase in additional shell thickness, and therefore, strengthens the obtained fit results. As both the antibody as well as the antigen are proteins, it can be assumed that their densities are similar, so that it is valid to compare the increase in shell thickness with the increase in molecular weight. Moreover, the obtained shell thickness upon antibody binding suits well reported sizes of antibodies.[167–169] The relevant parameters derived by the fitting procedure for the antibody functionalization and the full coating by antigens are summarized in Fig. 5.29.

$$\mu_L^{bio} = \mu_L^{hydro} + 2\mu_{t^{bio}} \tag{5.14}$$

$$\mu_d^{bio} = \mu_d^{hydro} + 2\mu_{t^{bio}} \tag{5.15}$$

The method for the fits, which are executed to describe the obtained measurement data, is a procedure, which involves a loop-wise execution of calculating the

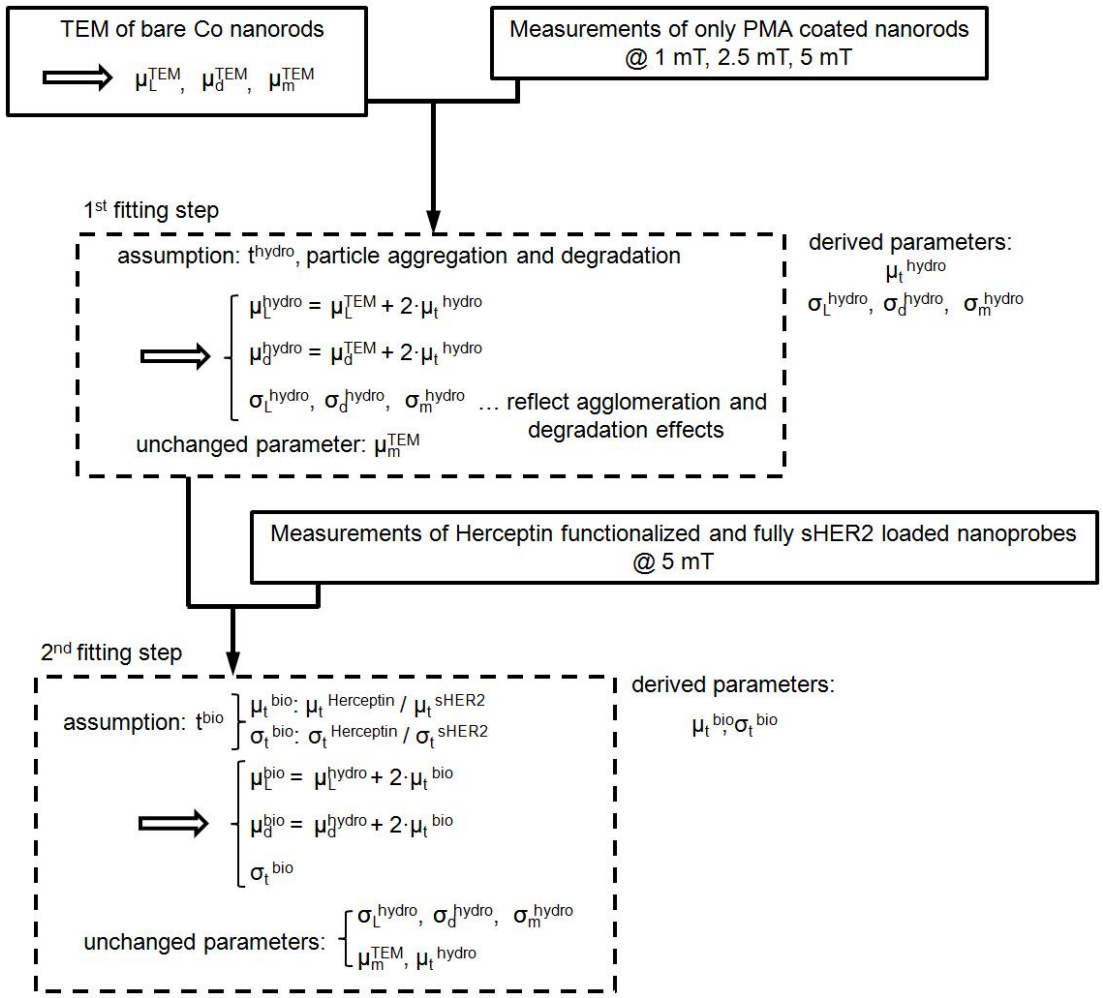

Figure 5.27.: Flow chart demonstrating the two-step fitting procedure. The derived parameters are given for each involved step for the length L, the diameter d, the magnetic moment m and an additional shell with thickness t (mean values μ and standard deviations σ). TEM image analysis serves as a first basis for the determination of the particle parameters. By the measurements and the respective fitting of only PMA coated nanorods and under the assumption of an additional hydrodynamic shell t^{hydro} and particle aggregation, the main hydrodynamic parameters are derived, which describe the rotational behavior of nanoparticles after the PMA coating. These parameters are used for fitting the phase lag behavior of Herceptin functionalized as well as fully sHER2 coated nanoparticles, which results in the determination of the values for the thicknesses of the corresponding shells ($\mu_{t^{bio}}$, $\sigma_{t^{bio}}$). Details on each step are given in the text.

TEM	
μ_L^{TEM}	52 nm
μ_d^{TEM}	5 nm
μ_m^{TEM}	$1.49 \cdot 10^{-18}$ Am^2

1st fitting step	
μ_t^{hydro}	5.5 nm
μ_L^{hydro}	63 nm
σ_L^{hydro}	45 nm
μ_d^{hydro}	16 nm
σ_d^{hydro}	6 nm
σ_m^{hydro}	$0.85 \cdot 10^{-18}$ Am^2

2nd fitting step	
$\mu_t^{Herceptin}$	15 nm
$\sigma_t^{Herceptin}$	9.5 nm
μ_t^{sHER2}	25 nm
σ_t^{sHER2}	13 nm

Figure 5.28.: All parameters, which are derived via the different steps of the fitting procedure. Mean values μ and standard deviations σ of the length L, the diameter d and an additional shell with thickness t are given.

Hydrodynamic length	63 ± 45 nm
Hydrodynamic diameter	16 ± 6 nm
Magnetic moment	$(1.49 \pm 0.85) \cdot 10^{-18}$ Am^2
Additional shell thickness for Herceptin functionalization	15 ± 9.5 nm
Additional shell thickness for fully sHER2 loaded nanoprobes	25 ± 13 nm

Figure 5.29.: Mean values and standard deviations of the parameters, which are used to characterize the functionalization with Herceptin as well as the full loading with sHER2.

phase lag based on the mathematical model, comparison to the measured data and subsequent adjustment of the calculation parameters. The latter are varied within physically reasonable ranges. Stop criteria for the fitting procedure are defined. Regarding the lengths parameters, the fitting is stopped once a variation of less than 0.1 nm does not improve the result. The stop criterion for the standard deviation of the magnetic moment is fulfilled for a variation of less than 1% of the mean value. An attempt of a purely mathematical fitting (minimization of the difference between measured and calculated data) has been made, but due to the complexity of the rotational dynamics, no physically reasonable result can be found. The knowledge of the curvature of the obtained phase lag spectra in a frequency regime beyond the measured one is a crucial requirement for obtaining a reasonable fit. Thus, the here used fitting approach is favorable, which results in both fits with a good agreement to measured data and reasonable parameters derived from the fitting procedure.

Herceptin-sHER2 Assay - Limit of Detection

Phase lag spectra as shown in Fig. 5.26 are well-suited for characterizing the nanorod dispersions and extracting average molecular shell thicknesses by fitting the spectra. However, for actual measurements it is sufficient to only look at the relative phase lag difference of the nanoprobes exposed to the sample with respect to nanoprobes immersed in a reference solution at a single magnitude and frequency of the applied rotating magnetic field. Fig. 5.30 shows the relative phase lags for different concentrations of sHER2 sample dispersions along with a logistic fit at a frequency of 1030 Hz and 5 mT field strength. Clearly, the measured phase lag difference increases systematically with the concentration of added sHER2 antigen. This indicates an increasing hydrodynamic volume of the nanorods due to binding of sHER2 protein to the immobilized Herceptin antibodies. The error bars in the figure are calculated with the standard deviations of the single measurements using the error propagation law (the error of the reference measurement is added to the error of the sHER2 measurement). All measurements are done under physiological salt conditions with a large amount of BSA protein present. Albumin is the most abundant protein in human serum and is used here at a concentration of 15 μM corresponding to a serum dilution factor of about 40,[170] which demonstrates the feasibility of the PlasMag homogeneous immunodiagnostic measurement principle in a relevant environment.

The logistic function for fitting the obtained measurement data for different concentrations of the antigen takes the form:

$$\Delta\phi(c) = \frac{A - B}{1 + \left(\frac{c}{c_0}\right)^{\alpha}} + B, \tag{5.16}$$

with the measurement signal without antigen present in solution A=0°, the saturation phase lag change value B=14.3°, the concentration at half of the maximum measured signal c_0, and a value α, derived from the fit.[17]

The logistic fit indicates a limit of detection of approximately 20 nM, i.e. the phase lag change is greater than 2.5 times the standard deviation.

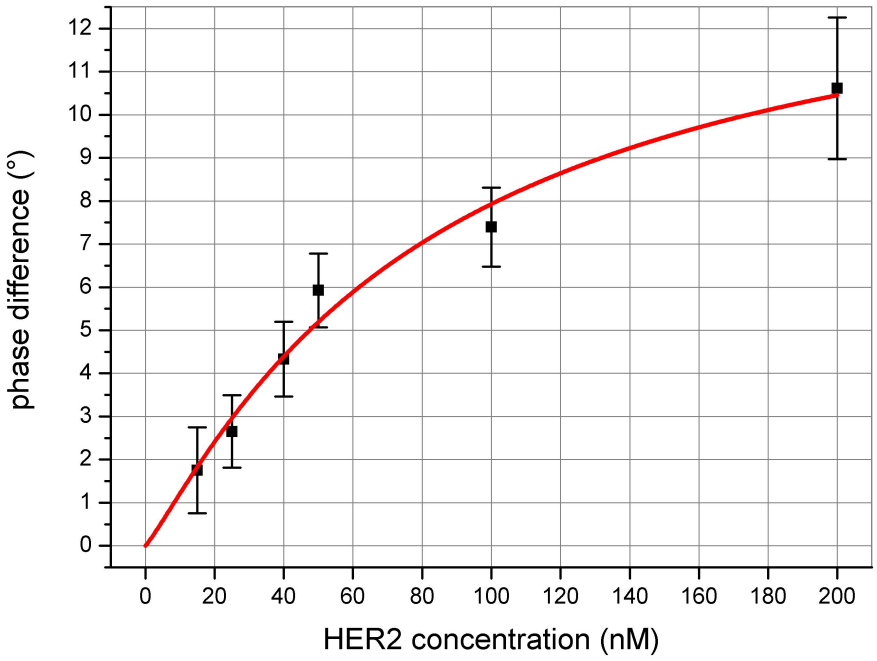

Figure 5.30.: Dependence of the measured phase lag difference on the concentration of added sHER2 antigen (difference with respect to a reference sample without added sHER2). The measurements are carried out at a field strength of 5 mT and at a frequency of 1030 Hz.

Herceptin-sHER2 Assay - Nanoprobe Concentration vs. Limit of Detection

A simple strategy to improve the limit of detection (LOD) is to decrease the number of used nanoprobes, which results in an increase of target molecules per nanoprobe. The binding mechanism of antibodies to antigens relies on an affinity binding, which involves binding kinetics. For a homogeneous assay principle like PlasMag, the binding kinetics are very fast due to the three dimensional diffusion of both binding partners, so that the equilibrium state is reflected by the measurements. The strength of an antibody antigen bond is described by the binding affinity constant.

The formation of antibody-antigen complexes can be well described by the law of mass action.[171] Here, the relation between the concentration of free antibodies [fAb], free antigens [fAg] and the concentration of formed antibody-antigen complexes [AbAg] is

$$[\mathrm{fAb}] + [\mathrm{fAg}] \underset{k_d}{\overset{k_a}{\rightleftharpoons}} [\mathrm{AbAg}], \tag{5.17}$$

with the rate constants of forward and reverse reactions k_a and k_d.[171] The law of mass can also be expressed as

$$K = \frac{k_a}{k_d} = \frac{[AbAg]}{[fAb][fAg]}, \tag{5.18}$$

where K is called the binding affinity constant.[171] By introducing the equilibrium dissociation constant K_D as the reverse of the binding affinity constant, it follows that[171]

$$K_D = \frac{1}{K} = \frac{[fAb][fAg]}{[AbAg]}. \tag{5.19}$$

To calculate the number of formed complexes, the concentration of free antibodies is replaced by the concentration of initial antibodies subtracted by the concentration of formed complexes

$$[fAb] = [Ab] - [AbAg], \tag{5.20}$$

and the same is done for the free antigen concentration

$$[fAg] = [Ag] - [AbAg], \tag{5.21}$$

so that by inserting 5.20 and 5.21 in 5.19, a quadratic equation is obtained for the concentration of complexes [AbAg]:

$$K_D[AbAg] = ([Ab] - [AbAg])([Ag] - [AbAg]). \tag{5.22}$$

Thus, it follows that the concentration of formed complexes is given by

$$[AbAg] = -\frac{(-K_D - [Ag] - [Ab])}{2} \underset{(-)}{+} \sqrt{\frac{(-K_D - [Ag] - [Ab])^2}{4} - [Ab][Ag]}, \tag{5.23}$$

with only the + sign resulting in a reasonable result.

To solve equation 5.23 a medium number of ten immobilized functional Herceptin antibodies per nanorod and an equilibrium dissociation constant K_D=0.49 nM is assumed.[172] The calculations result in Fig. 5.31, which qualitatively demonstrates the antibody receptor coverage for the Herceptin-HER2 assay system. It can be seen that by decreasing the detectable nanoprobe concentration, it is possible to improve the analyte LOD. Generally, the better the affinity constant of the antibody to the antigen, the more can be gained from a decreased detection limit of the nanoprobes. Also, a further increase of the thickness of the noble metal shell of the Co nanorods will enhance the optical signal amplification by excitation of localized plasmon resonances within the shell, which will help to detect lower nanorod concentrations.

The incubation time is limited by the diffusion of the nanoprobes as well as of the analyte molecules and it can be expected that the incubation time will be increased for low concentrations of the binding partners. However, for the concentrations

used in this thesis, no time depending effect is observed and the measurements can be carried out directly after mixing the reagents. Here, the incubation time is the time needed for mixing the reagents and starting the measurement (less than 5 min), and it is long enough to observe measurement results of the analyte binding that are stable over time.

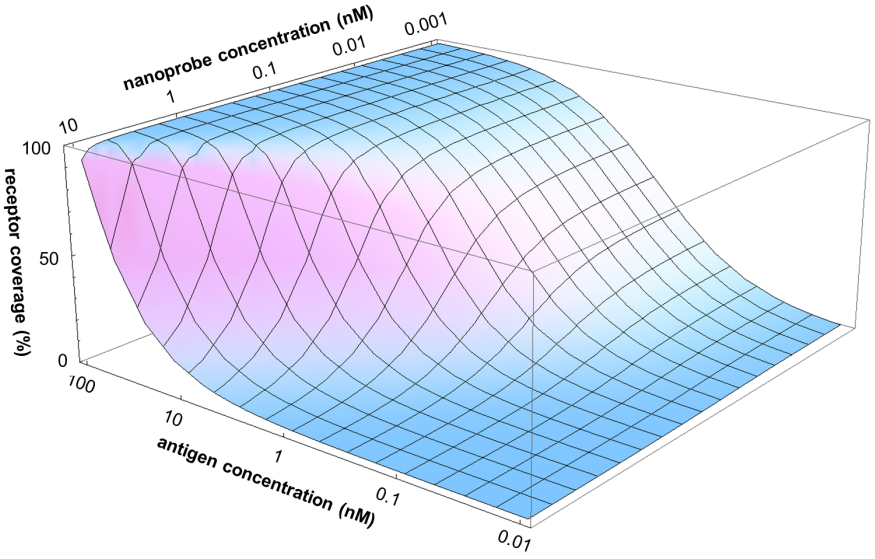

Figure 5.31.: Calculated dependence of the antibody receptor coverage ratio on the concentration of antigens and nanoprobes present in solution. Herceptin-sHER2 assay with an equilibrium dissociation constant of K_D=0.49 nM.

The measurements of the sHER2 assay prove the PlasMag principle for specific binding of analyte molecules in the presence of large concentrations of albumin protein as unspecific binding control in a buffered solution at physiological salt conditions. The analyte LOD of 20 nM of these measurements is still above the clinically relevant value of 140 pM. As regards a comparison to an established measurement method, the Siemens ADVIA Centaur instrument, which is not applicable for POC testing, reaches a limit of detection of about 5 pM.[26] However, the calulations of the dependence of the nanoprobe concentration on the receptor coverage, which directly translates into the measurement signal, shows that by decreasing the nanoprobe concentration, clinically relevant LODs can be accomplished by the PlasMag measurement method.

6. Conclusions and Outlook

It is expected that in the near future automated and easy to use POC measurement devices will play a major role in the diagnosis of various diseases. Among the different methods for diagnostics, the detection of biomarkers has gained great attention in the last two decades. In this thesis, a new approach (PlasMag) for biomarker POC testing is presented that enables homogeneous label-free biosensing. A versatile method of an easy to use and fast measurement technique for POC applications has been realized.

The nanoparticle-based measurement method is based upon the optical detection of the rotational dynamics of nanoparticles immersed in the sample solution. For this purpose, hybrid nanorods with magnetic and optical anisotropic properties are employed, which are rotated in an external magnetic field. The measurement signal originates from changes of the hydrodynamic volume upon binding of analyte molecules that lead to altered rotational dynamics. To be more precise, the nanorods experience a drag torque that results in a phase lag between the main axis of the nanorods and the external rotating magnetic field. Changes of the hydrodynamic volume lead to altered phase lags, which are recorded in dependence of the frequency and the magnitude of the external magnetic field.

Within the scope of this thesis, the PlasMag measurement method itself and its underlying fundamental principles were discussed including the involved physics that present a theoretical background needed for the interpretation of the achieved experimental results. Modeling of the optical, magnetic and hydrodynamic nanorod characteristics within the scope of current physical and chemical particle fabrication techniques enables to determine the properties of the best suited nanoparticle type. Furthermore, the theoretical modeling supports the identification of important parameters for a suitable measurement setup. As a result of the modeling, Au shell coated Co core nanorods with a 5 nm thick Au shell, a fixed core diameter of 6 nm and a variable core length that depends on the actual laser light wavelength are identified as optimal. To enable successful biomarker detection, a measurement setup fulfilling the experimental requirements for PlasMag biosensing has been realized and characterized.

For an experimental proof of principle bare magnetic nanorods (Co and Ni) as well as Co nanorods coated by a noble metal shell were used.

A first demonstration of the PlasMag measurement principle is given using bare Co nanorods dispersed in organic solvents. It could be shown that, in principle, the obtained signal suits the theoretically expected behavior. However, particle agglomeration and stabilization in aqueous solution is a major concern, so that bare Co nanorods are no suitable particle types for the proposed measurement

method.

In a next step of validating the PlasMag principle, single particle dispersions of Ni nanorods have been employed, and unspecific binding of protein to the surface of the nanorods has been shown. Here, protein binding mimics antibody binding for a future specific detection of biomarkers. Fitting of observed phase lag spectra for the rotational dynamics of bare and protein coated nanorods with a recently developed theoretical model revealed hydrodynamic size volume changes upon protein binding that can be well explained by the size of the protein and changes of the stagnant surface layer. Moreover, electrophoretic mobility measurements by an alternative measurement method prove the results obtained by the PlasMag method. Due to the large geometric dimensions of these nanorods compared to the Co nanorods, their suitability for PlasMag measurements is limited as the achievable sensitivity can be expected to be comparably low.

Once noble metal shell coated nanoparticles have been available, specific binding of analyte molecules was made possible. Noble metal shells composed of Au and Pt have been synthesized around a Co core and serve as a protecting layer. Furthermore, particle stabilization in aqueous buffer solutions has been achieved using an amphiphilic polymer coating process. The polymer coating allowed to fabricate nanoprobes with biotin and antibody functionalization. Biotin-streptavidin binding assays have been conducted and serve as a first proof of specific binding. For the final proof of principle of the PlasMag method, a binding assay of the breast cancer biomarker sHER2 has been realized. Measurements at physiological salt conditions and under addition of large amounts of albumin protein to mimic serum-like properties prove the suitability of the measurement method. Fitting the obtained phase lag spectra results in reasonable increases of the hydrodynamic volume and suit the measured behavior. Changes of the rotational dynamics upon antibody functionalization and upon analyte binding are well described by the model. A limit of detection of 20nM has been be achieved.

Future optimizations of the measurement method affect the physical as well as the biochemical properties of the used nanoparticles and modifications of the measurement setup. Mainly two strategies can be used to further improve the limit of detection: First, a decrease of the used nanoprobe concentration within the sample solution, and second, a modified functionalization procedure that increases the relative change in volume upon binding of analyte molecules.

The particles derived by electrochemical deposition into commercial nanoporous membranes can be further optimized by decreasing the diameter and subsequently the volume of the obtained nanorods. For this purpose, membranes with pore diameters down to 13 nm are available. Furthermore, the stabilization of these nanorods by applying suitable surface chemistry can be improved. By using nanorods composed of Ni with Au on the tips only, a particle type is presented that provides an option for a localized functionalization on the Au tips. This would result in an increased sensitivity upon analyte binding due to the enlarged relative change of nanorod drag torque compared to a homogeneous binding over the whole particle surface.

Generally, independent of specific synthesis methods applied, the nanoprobe limit of detection can be further enhanced by the large scattering cross section inherent to localized plasmon resonances excited within the noble metal shells. By enhancing both the optics of the instrument (scattering geometry) and the noble metal shell of the nanorods, the detectable nanoprobe concentration can be decreased. Furthermore, the noble metal shell can be used to do multiplexed analysis of the sample solution by a spectral separation of the longitudinal plasmon resonance of differently functionalized nanoprobes.

The law of mass action allows to describe the formation of antibody-antigen complexes and to evaluate the theoretically possible limit of detection depending on the concentration of used nanoprobes. It has been shown that by a further decrease of the nanoprobe concentration, the limit of detection can be lowered as well and that a clinically relevant sensitivity can be reached. Thus, by optimizing the assay system and testing different types of antibodies, the PlasMag system can be improved accordingly.

Another option for optimizing the measurement method is to use fragmented antibodies, which possess the antigen recognizing fragment only. Thus, the relative increase in hydrodynamic volume upon antigen binding can be enhanced, which subsequently increases the sensor's sensitivity. Alternatively, aptamers can be used instead of antibodies. These are nucleic acid or amino acid based small molecules able to bind to a specific analyte. Their benefit would be the smaller size of the aptamer compared to an antibody.

Regarding a future optimization of the measurement setup and its specifications, the fits to the sHER2 measurements can be used to define the optimal working point. Fig. 6.1 shows the calculated phase difference between antibody functionalized and fully target molecule loaded nanoprobes in dependence of the field strength and frequency. A maximum signal is achieved at approximately 1 kHz (only slightly shifted with the field magnitude), which decreases quickly at lower frequencies. Increased field magnitudes result in increased phase differences, but with a weak dependence. Therefore, a modification of the measurement setup to reach magnetic field strengths up to 10 mT at frequencies around 1 kHz seems reasonable. The increase in field strength does not only enlarge the obtained phase lag, but also results in an increased alignment ratio of the nanoparticles, which further optimizes the obtained measurement signal.

Further steps to clinically validate the biosensing principle are measurements of cell lysates consisting of in vitro grown cells that are forced to produce a high amount of HER2 protein. As the lysate is a complex mixture of all the molecules present in the cell culture including, HER2, other proteins, lipids, and nucleotides, its complexity is comparable to serum. Thus, it is well suited for future tests of the PlasMag system. Mouse serum of animals with cancer showing elevated levels of sHER2 can be used as well. The final clinical proof of principle can be accomplished by measurements of human serum and added amounts of sHER2 protein followed by measurements of serum of cancer patients and healthy controls.

Furthermore, testing for different biomarkers suitable for alternative POC appli-

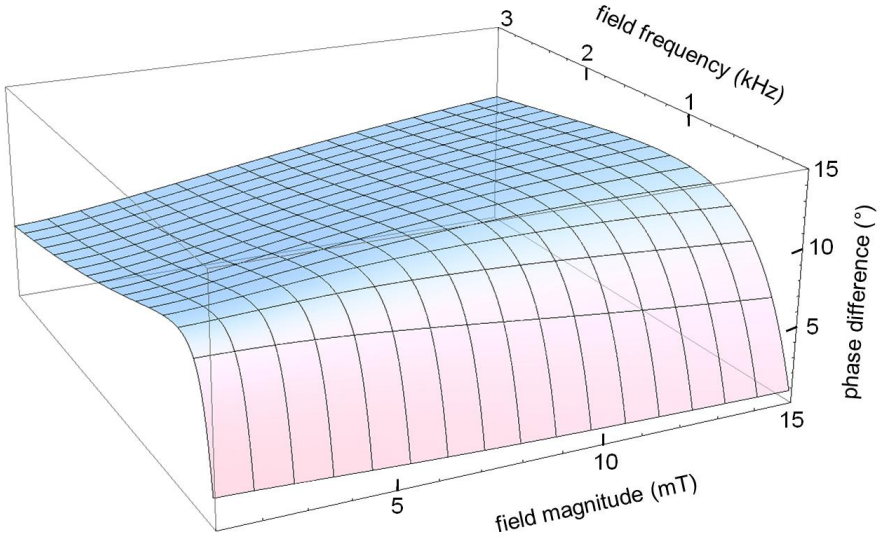

Figure 6.1.: Calculated phase difference between antibody functionalized and target molecule loaded nanoprobes to identify an optimal working point of a further optimized measurement setup.

cations will demonstrate the broad suitability of the PlasMag biosensing method.

To conclude, this thesis summarizes the theoretical background as well as the experimental conditions that are needed for applying the PlasMag measurement principle. Measurements that prove the biosensing method are presented and an outlook is given that provides strategies for a further improvement of the technique. Based on the results presented here , it appears promising to further continue working on the measurement method and to develop it towards an applicable POC testing instrument.

A. Coil Characterization

The coils are wound with a copper wire of 1 mm diameter on polyvinyl chloride (PVC) holders and possess diameters in the center of the winding pack of 150 mm (289 windings) and 70 mm (196 windings), respectively. The generated magnetic field is simulated by Femlab for each coil in order to test the homogeneity. In Fig. A.1 the resulting simulated magnetic flux density magnitude is plotted for each coil pair in a radial cut plane and for an applied current of 10 A. The component of the magnetic flux density in direction of the coil axis along a radial line in the coil pair center is plotted in Fig. A.2. Both figures demonstrate good homogeneity of the magnetic flux density in the center of the setup where the sample is placed.

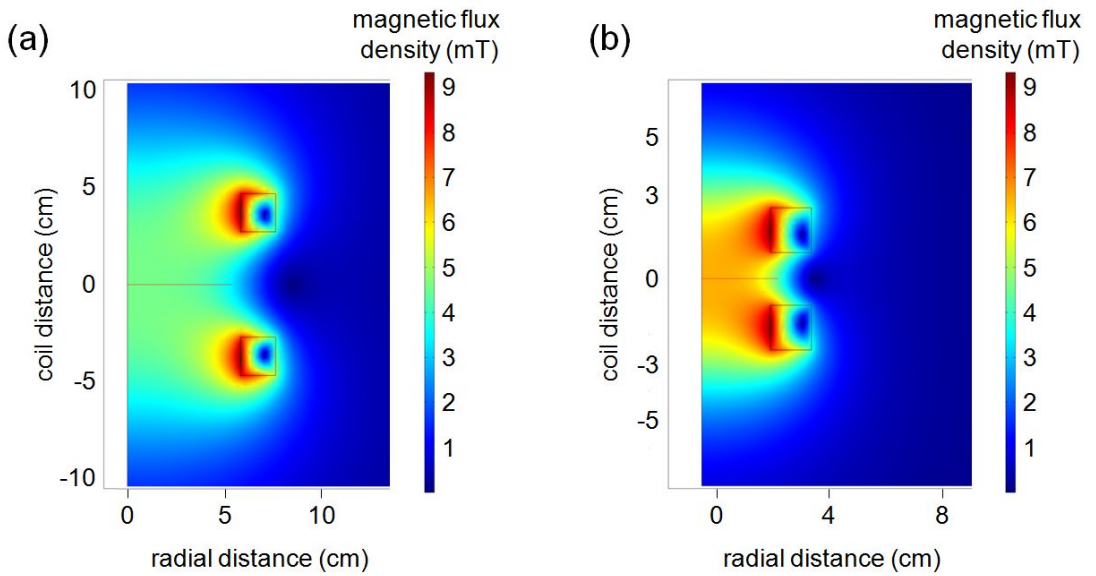

Figure A.1.: Simulated magnetic flux density for the large Helmholtz coil (a) and the small coil (b) for an applied current of 10 A.

In the measurement setup, the phase of the applied magnetic field is deduced from the phase of the voltage drop across a shunt resistor. Here, it is assumed that there is no phase difference between the magnetic field and the shunt resistor. As real coils also possess parasitic capacitances between their windings, this is only the case for negligible capacitive parasitic currents. Fig. A.3 shows the equivalent circuit diagram of a real coil along with the shunt resistance R_1. If the values of

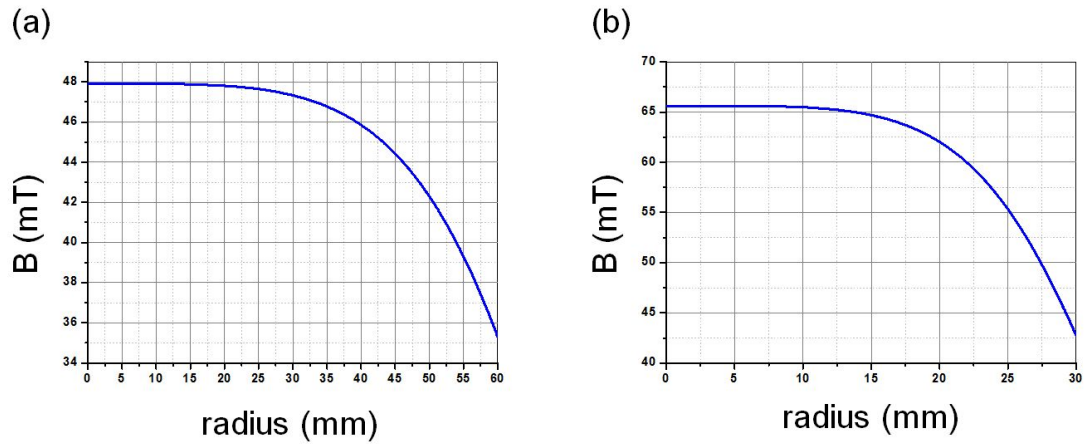

Figure A.2.: Simulated magnetic flux density for the large Helmholtz coil (a) and the small coil (b) caused by a current of 10 A.

the ohmic coil resistance R_2, the inductance L_2 and the parasitic conductance C_3 are known, this equivalent circuit can be used to determine the phase difference between the measured shunt current I_1 and the ohmic coil current I_2 that generates the magnetic field.

The inductance and capacitance of each coil pair was measured with a LCR meter (Agilent 4284A). First, the inductance has been measured at a low frequency of 20 Hz relying on a serial L-R model, while the capacitance has been calculated after measuring the resonance peak of the impedance (see Fig. A.4) by the resonance condition:

$$f_{res} = \frac{1}{2\pi\sqrt{LC}}. \tag{A.1}$$

Furthermore, the inductance and capacitance of each coil have been calculated based on theoretical models,[173,174] and the obtained values have been compared to the measured ones in Fig. A.5. While the calculated inductance values fit well to the measured ones, the capacitance values differ more significantly, which can be attributed to the approximations made for the capacitance calculations.[173,174]

Calculating the phase difference between the shunt and "inductance current" shows that the phase shift stays below 10^{-3} degrees up to 3 kHz for each coil pair. These results have also been verified using the 5Spice Analysis software.

To sum up, deducing the phase of the magnetic field from the shunt current is a valid method with negligible error.

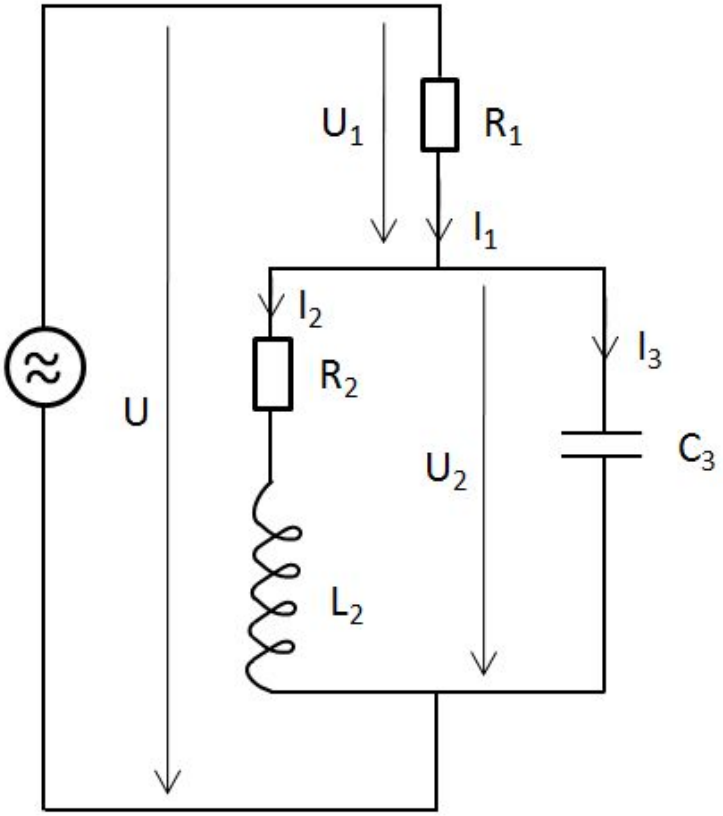

Figure A.3.: Equivalent circuit diagram of a real coil including the shunt resistor R1.

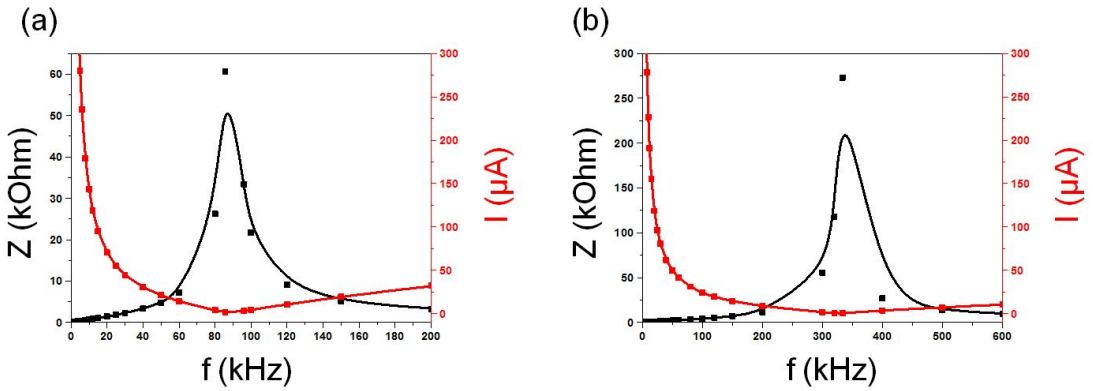

Figure A.4.: Measured resonance peaks of the impedance Z of both Helmholtz coils. (a) large coil pair and (b) small coil pair.

	R (Ohm)		L (mH)		C (pF)	
	meas	calc	meas	calc	meas	calc
large coil pair (parallel)	1.5	1.5	11.1	11.2	310.6	200.4
small coil pair (serial)	1.95	1.88	7.3	7.3	31.2	23.6

Figure A.5.: Comparison of calculated and measured coil parameters.

B. Nanorod Synthesis by Electrochemistry

Electrochemical methods can be applied for the synthesis of nanoparticles of defined composition and shape. Here, nanorod synthesis by electrodeposition into nanoporous templates is accomplished by a three electrode system (working electrode, counter electrode, and reference electrode). The working electrode with the nanoporous template, a platinum grid counter electrode, and a silver/silver chloride reference electrode are immersed in an electrolyte solution, which contains the metal to be deposited as dissolved salt (metal cations). By applying an electrical potential, the working electrode acts as cathode, resulting in a movement of the cations toward the electrode, and in a subsequent reduction of the ions to bulk metal. The reference electrode is used to control the applied voltage, whereas the counter electrode is needed for the charge transfer and to supply the current for the chemical reduction. The reduction inside the pores results in the formation of nanorods, which are controllable in length by limiting the overall charge transfer.

To that end, different commercially available templates were tested (track etched polycarbonate (PC) and anodic aluminum oxide (AAO) membranes from Whatman purchased from VWR, and AAO membranes purchased from Synkera Technologies). Membranes were characterized by electron microscopy techniques prior to the electrodeposition. Here, the employed electrochemically deposited materials are Ni and Au. Synthesis of nanorods of different composition into porous templates consists of 3 major steps. First, a conducting material (working electrode) is deposited on one side of the membrane to close the pores and to enable the electrodeposition process, second, the nanopores are filled with the cations and these are subsequent reduced to bulk metal by applying a suitable voltage between the counter and the working electrode, and third, the dissolution of the membrane to release the formed nanorods. In this chapter, the main synthesis steps and the main results will be presented. The focus of the deposition results presented here is based on the different synthesis possibilities, so that information about the length of the nanorods will not be given.

For the electrochemical nanorod synthesis, a custom built setup in a beaker glass (500 ml volume) was used, which consists of the mentioned three electrodes - mounted by polytetrafluoroethylene (PTFE) parts - and additional probes to control and monitor the temperature and the pH value of the electrolyte (see sketch in Fig. B.1). An Autolab potentiostat / galvanostat (PGSTAT30) was used to apply negative DC potentials relative to the reference electrode. The working electrode was fabricated by different materials either by sputter deposi-

tion or by thermal evaporation. Indium-doped tin oxide and Au thin films were deposited under Ar atmosphere by DC magnetron sputtering (Leybold Univex 450 C) from 4 inch targets. By thermal evaporation (Leybold Univex 450), thin films of titanium, gold and silver were deposited. The membrane with the deposited working electrode was fixed on a custom PTFE mount and sealed to avoid contact of the electrolyte to the back side (electrodeposition through the pores only). Sealing can be achieved either by a rubber O-ring, or by polydimethylsiloxane (PDMS).

For the synthesis of Ni nanorods, a Watts bath was used, comprising nickel sulfate, nickel chloride, and boric acid dissolved in ultrapure water (300 g/l $NiSO_4 \cdot 6\,H_2O$, 50 g/l $NiCl_2 \cdot 6\,H_2O$, 40 g/l H_3BO_3) at a pH value of 4.5 (adjusted by the addition of HCl and NaOH). The temperature of the Watts bath was set to 50° C, and the electrolyte solution was stirred magnetically. The electrolyte for the Au deposition consist of $HAuCl_4 \cdot 3\,H_2$ dissolved in ultrapure water at a concentration of 10 mM. Here, the temperature of the solution was kept at room temperature and no stirring was employed. Following the electrochemical deposition steps, the samples were removed from the solution immediately and thoroughly rinsed with ultrapure water to eliminate residual salts and unreacted products. Afterwards, the samples were dried under a moderate air flux at 70° C.

Dissolving of the PC membranes was accomplished by dichloromethane (DCM), CH_2Cl_2, followed by subsequent washing steps with isopropyl alcohol (IPA) and magnetic separation. The AAO membranes were dissolved by 1 M NaOH and transferred to IPA by the same procedure as used for the PC membranes.

For the characterization of the initial templates, the Whatman PC membranes were coated with a 5 nm thick Au layer by sputter deposition to facilitate electron microscopy imaging. Fig. B.2 depicts that the PC membrane with 50 nm nominal pore diameter possesses well defined pores of low surface density, which are distributed randomly. Here, the pores are of uniform size through the whole membrane thickness (20 μm).

In Fig. B.3, scanning electron microscopy (SEM) images of Ni nanorods deposited in a PC membrane of 15 nm nominal pore diameter are shown. Here, a thermally evaporated silver electrode was used (300 nm thickness) and a negative potential of 1.1 V was applied. This deposition resulted in uniform nanorods of about 100 nm diameter. The difference between the nominal pore diameter and the actual nanorod diameter can be attributed to a swelling process of the PC membrane within the acidic electrolyte environment.

In addition to Ni nanorods, Au nanorods were synthesized within the pores of a PC membrane (see Fig. B.4 for a corresponding SEM image). Again, homogenous nanorods were obtained by electrodeposition.

Segmented nanorods of Au and Ni sections can be fabricated by subsequent depositions of these two metals. Rinsing steps with ultrapure water are required between the individual electrochemical depositions. Initial results for Au-Ni-Au segmented nanorods are presented in Fig. B.5. On the SEM image some of the nanorods seem to consist of different materials, even though alternative charac-

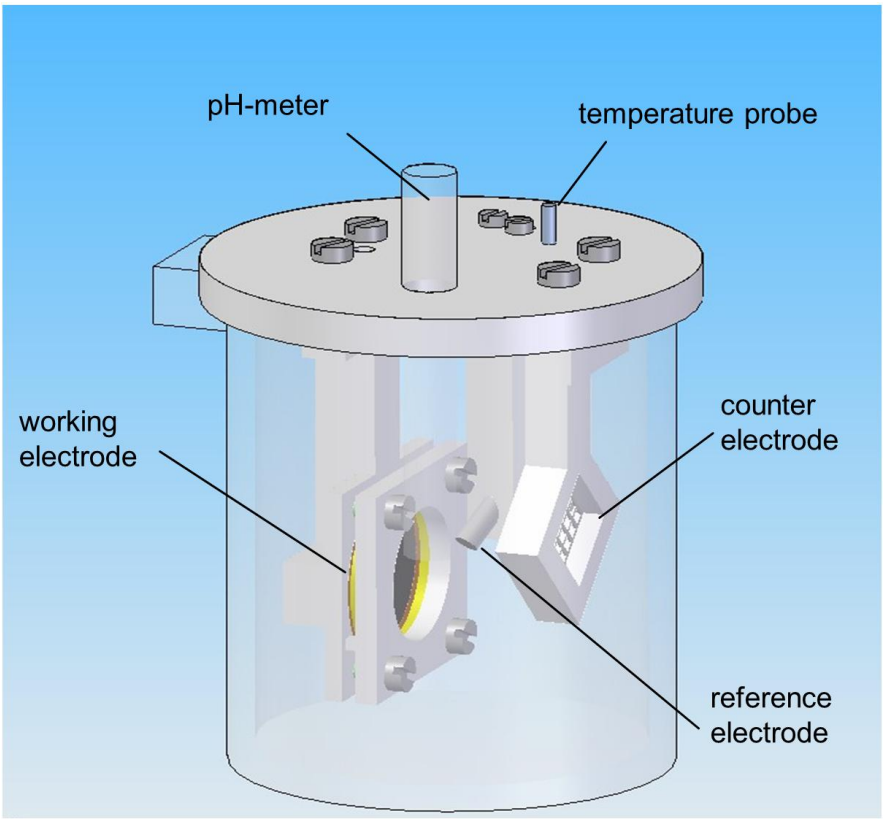

Figure B.1.: Sketch of the electrodeposition setup in a beaker glass, including the three electrode system, the temperature probe as well as the pH value probe.

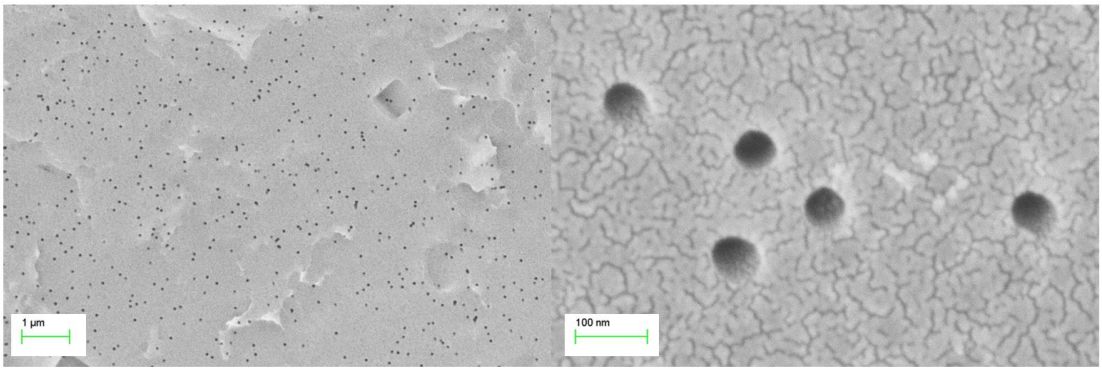

Figure B.2.: Whatman PC filter membrane with pores of 50 nm nominal diameter.

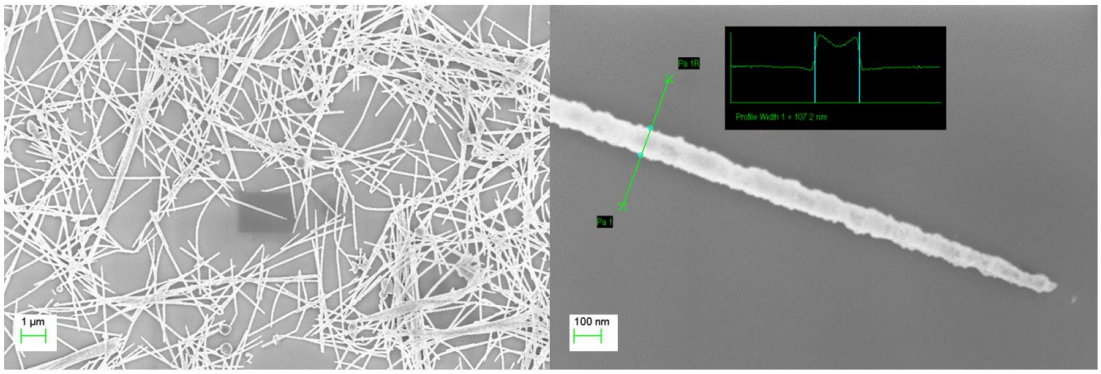

Figure B.3.: Ni nanorods deposited into a Whatman PC membrane.

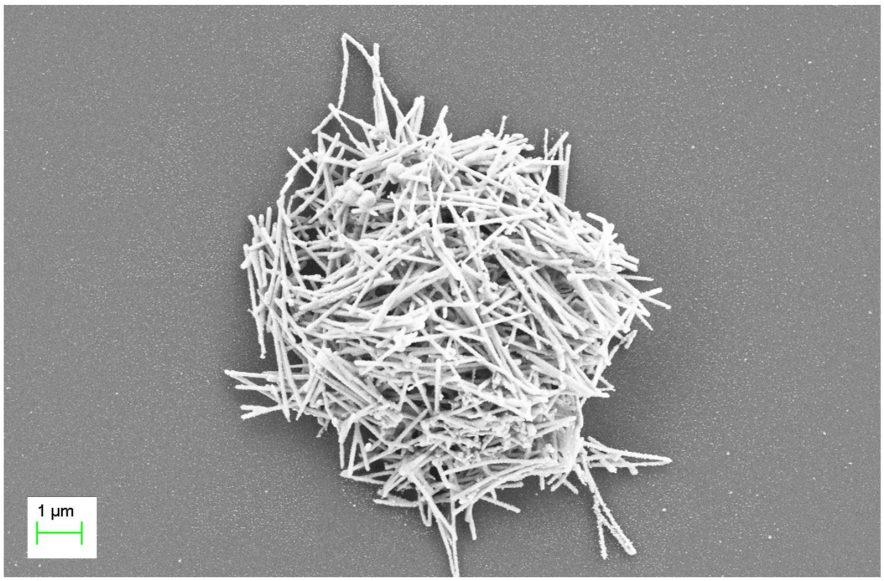

Figure B.4.: Au nanorods deposited into a Whatman PC membrane.

terization methods still have to be executed to clearly distinguish among different metals. Particles with a Au-Ni-Au composition possess the possibility of a localized functionalization on the Au tips only, which would be an option for improving the sensitivity of the PlasMag biosensing method. Reason for this is the increase of the drag torque upon analyte molecule binding on the tips of the nanoparticle compared to a homogeneous binding over the whole particle surface. This effect is especially of importance in case of a very low analyte concentration and low nanoprobe surface coverage with analyte molecules. Such a localized functionalization can be obtained by using thiols that strongly bind to Au and weakly bind to metal oxides, and carboxylic acid with a strong preference for the metal oxide.[175]

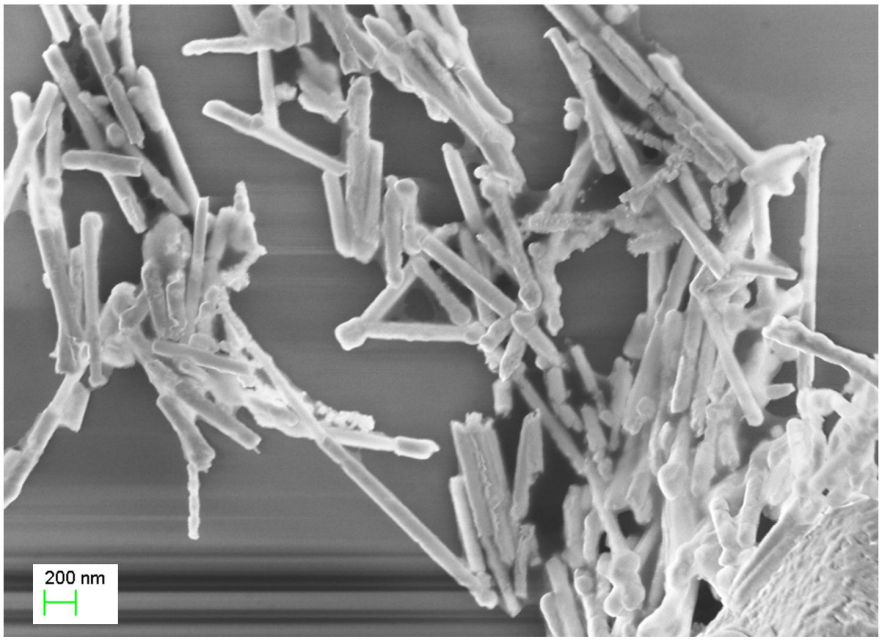

Figure B.5.: Au-Ni-Au segmented nanorods deposited into a Whatman PC membrane.

Whatman AAO membranes were characterized by electron microscopy according to initial preparation steps used for the PC membranes. In Fig. B.6, both sides of a membrane of 20 nm nominal pore diameter are shown (60 μm membrane thickness). The pore diameter differs substantially (200 nm and 20 nm, respectively) as well as the homogeneity of the pores. It is obvious that these membranes are suitable for filtering applications (i.e. the intended usage) but of restricted applicability for the synthesis of homogenous nanorods. Nevertheless, the pore density is higher compared to PC membranes, offering the possibility of larger synthesis batches.

Images of the cross section of these Whatman AAO membranes reveal that the pore diameter is reduced within the first 200-300 nm on the backside of the

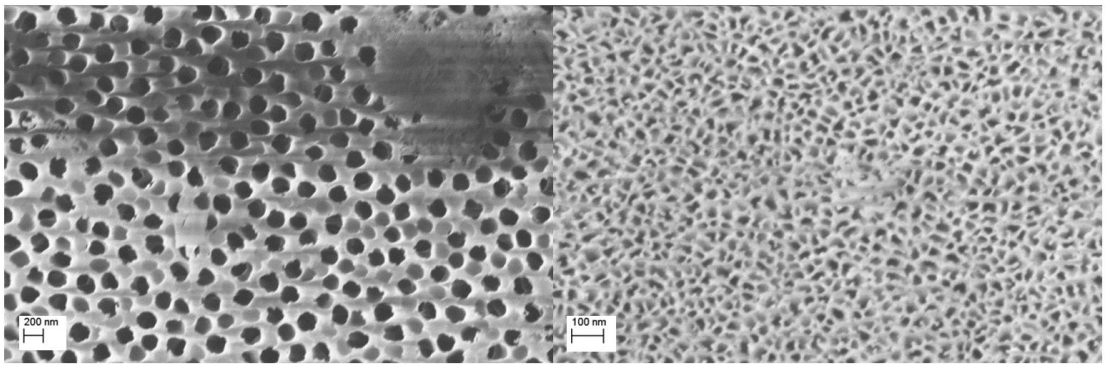

Figure B.6.: Front (left) and back (right) side of a Whatman AAO membrane. The pore diameter on the front side amounts to 200 nm, while the backside shows pore diameters of 20 nm.

membrane (see Fig. B.7). Thus, deposited Ni nanorods show a structure according to this pore geometry (see Fig. B.8). Here, the working electrode consists of a 500 nm thick ITO layer with a 10 nm thick Au layer on the backside. ITO offers the advantage of being dissolvable in NaOH. Therefore, the membrane as well as the electrode can be etched in one step without attacking the metallic nanorods. The applied negative potential amounted to 1 V.

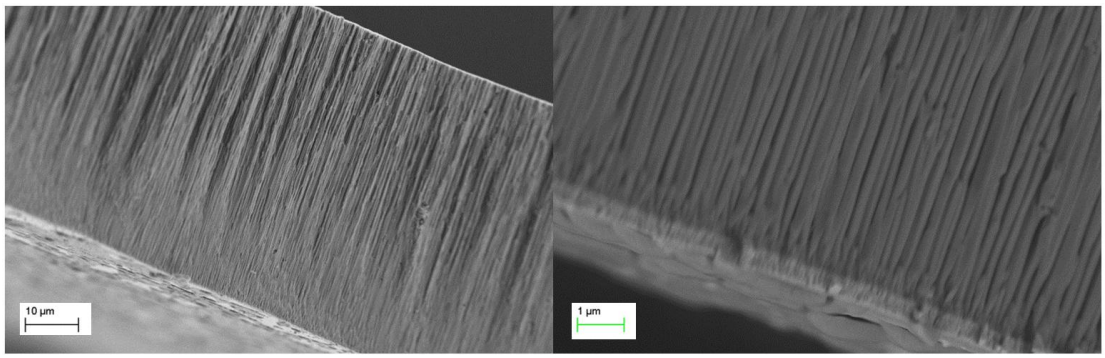

Figure B.7.: Whatman AAO membrane cross section.

The AAO membranes purchased from Synkera Technologies possess the advantage of uniform, small pore diameters (down to 18 nm) throughout the entire thickness (50 μm) of the membrane, and a very high pore density (the suppliers homepage provides details - www.synkerainc.com). Therefore, these membranes combine the advantages of both the Whatman PC and AAO membranes. The working electrode consists of a 500 nm thick ITO layer followed by a 20 nm thick Au layer, and the applied potential amounted to -0.9 V. The resulting particles have a diameter corresponding to the pore diameter of about 18 nm. The electrodeposition into these membranes results in a large amount of homogeneous

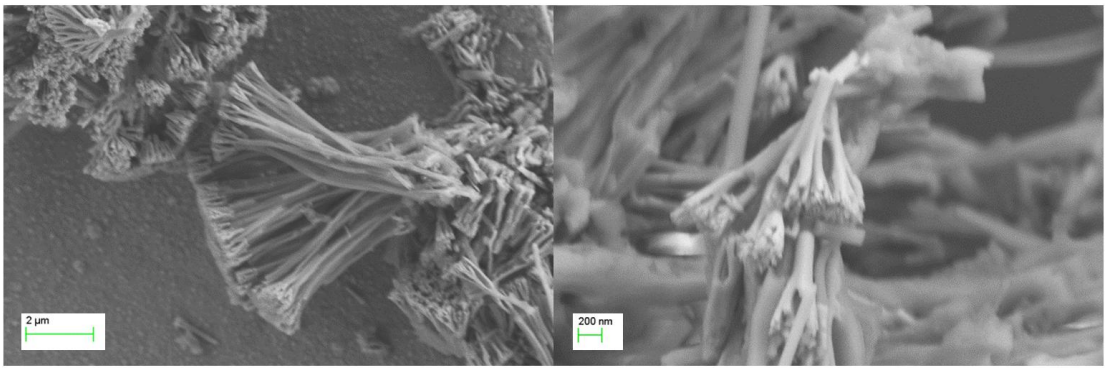

Figure B.8.: Ni nanorods deposited into a Whatman AAO membrane.

nanorods, even though the dissolution of the membrane and the particle stabilization have to be improved as it is shown in Fig. B.9.

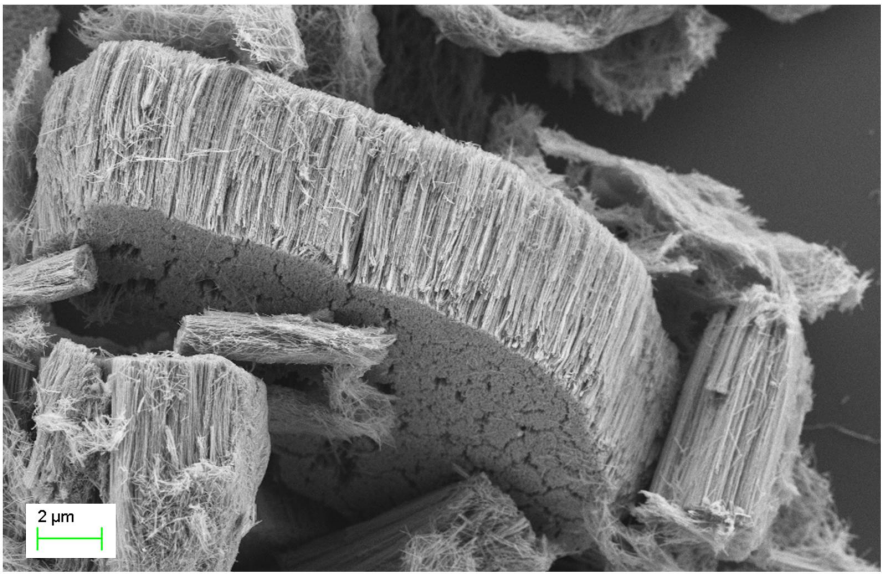

Figure B.9.: Ni nanorods deposited into a Synkera AAO membrane of 18 nm nominal pore diameter.

Acknowledgements

First of all, I want to thank my supervisors Univ.Doz. Dr. Hubert Brückl and Univ.Prof. Dr. Andreas Hütten for the opportunity to work on the PlasMag project and on the presented thesis. Furthermore, I want to thank for their advice and their support throughout the whole project.

The research on the PlasMag project leading to some of the results presented in this thesis was funded by the European Community's 7^{th} Framework Programme within the NAMDIATREAM project under grant agreement n° NMP4-LA-2010-246479. The coordinator of the PlasMag project and, thus, my first contact person in the daily work on the project was Dr. Jörg Schotter. I want to express my special thanks to Jörg for all of his support and his patience throughout the last years. The chance to work under his daily guidance gave me the opportunity to improve my knowledge on a broad base while working on this highly interdisciplinary project. It also included a lot of traveling to both international conferences and project meetings. I appreciated both the time spent together in scientific meetings as well as the after-work spare time in various bars all across Europe.

Further, I want to express my gratitude to Frank Ludwig and Jan Dieckhoff from the Institute of Electrical Measurement and Fundamental Electrical Engineering at the TU Braunschweig. They were of great help throughout the whole project time and supportive with discussions on almost all the topics related to PlasMag. I appreciated their scientific input as well as their hospitality during the visits in Braunschweig. I enjoyed working together in a productive atmosphere on long working days that did not miss a conclusive discussion in a typical Viennese restaurant or even ended up at a closed ski lift.

I want to thank Katerina Soulantica, Sergio Lentijo, Guillaume Viau, Lise-Marie Lacroix, Rym Boubekri and Jèrôme Maynadié from the Université de Toulouse, INSA, UPS, LPCNO, and CNRS, LPCNO in Toulouse for their great efforts in particle synthesis. Especially, the work of Katerina and Sergio on the noble metal coated nanorods made it possible to bring the PlasMag project on the high level as it is presented here.

Furthermore, I want to thank Andreas Tschöpe and Annegret Günther from the Saarland University in Saarbrücken for the supply of the Ni nanorods, which enabled the detection of protein adhesion onto the particles' surfaces.

A big thank you also goes to Wolfgang Parak and Beatriz Pelaz from the Philipps-Universität Marburg for their great efforts in particle stabilization and functionalization and for the opportunity to spend a whole week in their laboratory. Thanks for sharing your knowledge and your skills on the stabilization procedure as well as for spending your spare time outside the laboratory with an

Austrian guy "talking too much"!

The used Herceptin antibody was supplied by the group of Frauke Alves and Julia Bode at the Max Planck Institute for Experimental Medicine in Göttingen. The simple and quick way of providing the particles and their willingness to answer all appearing questions deserves great thanks.

I want to thank David Fernandez from Progenika Biopharma in Spain for his great advice and all the time and patience he spent on writing emails to a newbie to the HER2 topic.

I gratefully thank Dr. Seta Küpcü and Mehmet Hikmet Ücisik from the University of Natural Resources and Life Sciences in Vienna for providing access to the Zetasizer instrument.

I want to thank all my colleagues at the Austrian Institute of Technology in Vienna for the great and inspiring atmosphere, which can only be created by a group of people, who do not only share their scientific interests. Thanks for all the interpersonal contacts, which could be created throughout my time within this group, and for all the "evening discussions" that ended up in the middle of the night at some Würstelstand in the city center. Stephan Steinhauer deserves big thanks for sharing the passion for coffee, tennis, squash and the after-sport beer (I hope that after finishing the thesis I will be able to find more time for giving you a squash lesson). For their scientific input at many different occasions, I especially thank Eva Melnik, Paul Müllner, Roman Bruck, Nadja Kataeva, Rainer Hainberger, Giorgio Mutinati, Toni Köck, Theo Dimopoulos, Moritz Eggeling, Astrit Shoshi, Antun Peic, Jakub Dostalek, Rudi Heer, Thomas Maier, Xenia Descovich, Ivo Bachler and Stephanie Parragh. Furthermore, I would like to thank Kerstin Formanek, Shweta Kumar and Viktoria Vasalik for undertaking the effort to support me in daily administrative issues.

Leoni Breth did a great proof read of the thesis. This also included a couple of unpleasant questions that resulted in some extra work, but it helped a lot in improving both the language and the science of this thesis. But still, I do not want to marry her.

I want to thank Michael Richter for his support and all the effort he spent on the nanorod synthesis together with me. Moreover, I am very grateful to have a landlord like him. So, I still want to marry him.

I want to thank all my friends not already mentioned yet for all the time we spent together during the last years, and for the distraction I got whenever I needed it.

Furthermore, I want to thank the porters of the Techgate Vienna, Walter and Stefan, and the cleaning ladies, Aische and Mira, for the daily small talks and the warm comments on the state of my desk and my hair. A big thank you especially goes to Stefan, who shared his DVD library and supplied me with the entire work of the Coen brothers.

Last and least, I want to thank my parents Kir and Runz, my brother Zepparinix and my sister Maddalena for supporting me independently of whatever happens in my life and for providing the strong backbone I can always rely on.

Bibliography

[1] Ferlay, J.; Steliarova-Foucher, E.; Lortet-Tieulent, J.; Rosso, S.; Coebergh, J. W. W.; Comber, H.; Forman, D.; Bray, F. Cancer Incidence and Mortality Patterns in Europe: Estimates for 40 Countries in 2012. *Eur. J. Cancer*, 49:1374–1403, 2013.

[2] Cardoso, F.; Loibl, S.; Pagani, O.; Graziottin, A.; Panizza, P.; Martincich, L.; Gentilini, O.; Peccatori, F.; Fourquet, A.; Delaloge, S.; Marotti, L.; Penault-Llorca, F.; Kotti-Kitromilidou, A. M.; Rodger, A.; Harbeck, N. The European Society of Breast Cancer Specialists Recommendations for the Management of Young Women with Breast Cancer. *Eur. J. Cancer*, 48:3355–3377, 2012.

[3] Yager, P; Domingo, G. J.; Gerdes, J. Point-of-Care Diagnostics for Global Health. *Annu. Rev. Biomed. Eng.*, 10:107–144, 2008.

[4] eBioscience Inc. Product number BMS213HS.

[5] Liu, X.; Dai, Q.; Austin, L.; Coutts, J.; Knowles, G.; Zou, J.; Chen, H.; Huo, Q. A One-Step Homogeneous Immunoassay for Cancer Biomarker Detection Using Gold Nanoparticle Probes Coupled with Dynamic Light Scattering. *J. Am. Chem. Soc.*, 130:2780–2782, 2008.

[6] Diamandis, E. P.; Christopoulos, T. K. *Immunoassay.* Academic Press, San Diego, CA, 1996.

[7] Rowe, L.; Deo, S.; Shofner, J.; Ensor,M.; Daunert, S. Aequorin-Based Homogeneous Cortisol Immunoassay for Analysis of Saliva Samples. *Bioconjugate Chem.*, 18:1772–1777, 2007.

[8] Schotter, J.; Bethge, O.; Maier, T.; Brueckl, H. Optische Messverfahren zur molekularen Detektion anhand von Relaxationsmessungen in optisch anisotropen Nanopartikeln. Austrian patent number 503.845, 2007, PCT application number WO/2008/124853.

[9] Schrittwieser, S.; Schotter, J.; Maier, T.; Bruck, R.; Muellner, P.; Kataeva, N.; Soulantika, K.; Ludwig, F.; Huetten, A.; Brueckl, H. Homogeneous Biosensor Based on Optical Detection of the Rotational Dynamics of Anisotropic Nanoparticles. *Procedia Eng.*, 5:1107–1110, 2010.

[10] Schrittwieser, S.; Ludwig, F.; Dieckhoff, J.; Soulantica, K.; Viau, G.; Lacroix, L.-M.; Lentijo, S. M.; Boubekri, R.; Maynadié, J.; Huetten, A.; Brueckl, H.; Schotter, J. Modeling and Development of a Biosensor Based on Optical Relaxation Measurements of Hybrid Nanoparticles. *ACS Nano*, 6:791–801, 2012.

[11] Schrittwieser, S.; Ludwig, F.; Dieckhoff, J.; Tschoepe, A.; Guenther, A.; Richter, M.; Huetten, A.; Brueckl, H.; Schotter, J. Direct Protein Detection in the Sample Solution by Monitoring Rotational Dynamics of Nickel Nanorods. *SMALL*, 10:407–411, 2014.

[12] Liz-Marzan, L. M. Tailoring Surface Plasmons through the Morphology and Assembly of Metal Nanoparticles. *Langmuir*, 22:32–41, 2006.

[13] Heim, E.; Ludwig, F.; Schilling, M. Binding Assays with Streptavidin-Functionalized Superparamagnetic Nanoparticles and Biotinylated Analytes Using Fluxgate Magnetorelaxometry. *J. Magn. Magn. Mater.*, 321:1628–1631, 2009.

[14] Enpuku, K.; Tamai, Y.; Mitake, T.; Yoshida, T.; Matsuo, M. AC Susceptibility Measurement of Magnetic Markers in Suspension for Liquid Phase Immunoassay. *J. Appl. Phys.*, 108:034701, 2010.

[15] Oeisjoeen, F.; Schneiderman, J.; Astalan, A. P.; Kalabukhov, A.; Johansson, C.; Winkler, D. A New Approach for Bioassays Based on Frequency- and Time-Domain Measurements of Magnetic Nanoparticles. *Biosens. Bioelectron.*, 25:1008–1013, 2010.

[16] Lange, J.; Koetitz, R.; Haller, A.; Trahms, L.; Semmler, W.; Weitschies, W. Magnetorelaxometry - A New Binding Specific Detection Method Based on Magnetic Nanoparticles. *J. Magn. Magn. Mater.*, 252:381–383, 2002.

[17] Chieh, J. J.;Yang,S.Y.;Horng, H. E.;Yu,C.Y.;Lee,C.L.;Wu,H.L.;Hong, C. Y.; Yang, H. C. Immunomagnetic Reduction Assay Using High-Tc Superconducting-Quantum-Interference-Device-Based Magnetosusceptometry. *J. Appl. Phys.*, 107:074903, 2010.

[18] Aurich, K.; Nagel, S.; Gloeckl, G.; Weitschies, W. Determination of the Magneto-Optical Relaxation of Magnetic Nanoparticles as a Homogeneous Immunoassay. *Anal. Chem.*, 79:580–586, 2007.

[19] Buettner, M.; Weber, P.; Schmidl, F.; Seidel, P.; Roeder, M.; Schnabelrauch, M.; Wagner, K.; Goernert, P.; Gloeckl, G.; Weitschies, W. Investigation of Magnetic Active Core Sizes and Hydrodynamic Diameters of a Magnetically Fractionated Ferrofluid. *J. Nanopart. Res.*, 13:165–173, 2011.

[20] Ranzoni, A.; Schleipen, J. J. H. B.; van Ijzendoorn, L. J.; Prins, M. W. J. Frequency-Selective Rotation of Two-Particle Nanoactuators for Rapid and Sensitive Detection of Biomolecules. *Nano Letters*, 11:2017–2022, 2011.

[21] Anfossi, L.; Baggiani, C.; Giovannoli, C.; Giraudi, G. Homogeneous Immunoassay Based on Gold Nanoparticles and Visible Absorption Detection. *Anal. Bioanal. Chem.*, 394:507–512, 2009.

[22] Hirsch, L. R.; Jackson, J. B.; Lee, A.; Halas, N. J.; West, J. L. A Whole Blood Immunoassay Using Gold Nanoshells. *Anal. Chem.*, 75:2377–2381, 2003.

[23] Tse, C.; Gauchez, A.-S.; Jacot, W.; Lamy, P.-J. HER2 Shedding and Serum HER2 Extracellular Domain: Biology and Clinical Utility in Breast Cancer. *Cancer Treat. Rev.*, 38:133–142, 2012.

[24] Rexer, B. N.;Arteaga, C. L. Intrinsic and Acquired Resistance to HER2-Targeted Therapies in HER2 Gene-Amplified Breast Cancer: Mechanisms and Clinical Implications. *Crit. Rev. Oncog.*, 17:1–16, 2012.

[25] Siemens Medical Solutions Diagnostics. Understanding the Clinical Utility of Serum HER-2/neu. http://www.medical.siemens.com/siemens/it_IT/rg_marcom_FBAs/files/news/Understanding_clinical_utility_HER2.pdf, 2007. Immunoassay Serum HER-2/neu.

[26] Siemens Healthcare Diagnostics Inc. ADVIA Centaur Serum HER-2/neu Assay Specifications. http://www.healthcare.siemens.com/siemens_hwem-hwem_ssxa_websites-context-root/wcm/idc/groups/public/@global /documents/download/mdaw/mtyz/ edisp/0700113-00020142.pdf, 2009. Immunoassay Serum HER-2/neu.

[27] Official Website of the United States National Nanotechnology Initiative. http://nano.gov/nanotech-101/special.

[28] Askeland, D. R. *The Science and Engineering of Materials*. SI Edtion Van Nostrand Reinhold (International) Co. Ltd., Hong Kong, 1988.

[29] Ortega, D. Structure and Magnetism in Magnetic Nanoparticles. In Than, N. T. K., editor, *Magnetic Nanoparticles: From Fabrication to Clinical Applications*, pages 3–44, Boca Raton, FL, 2012. CRC Press Taylor & Francis Group.

[30] Oberdoerster, G.; Oberdoerster, E.; Oberdoerster, J. Nanotoxicology: An Emerging Discipline Evolving from Studies of Ultrafine Particles. *Environ. Health Perspect.*, 113:823–839, 2005.

[31] Coey, J. M. D. *Magnetism and Magnetic Materials.* Cambridge University Press, Cambridge, United Kindgom, 2010.

[32] Sundaresan, A.; Rao, C. N. R. Ferromagnetism as a Universal Feature of Inorganic Nanoparticles. *Nano Today*, 4:96–106, 2009.

[33] Cullity, B. D.; Graham, C. D. *Introduction to Magnetic Materials.* John Wiley & Sons, Inc., Hoboken, NJ, 2009.

[34] Blums, E.; Cebers, A.; Maiorov, M. M. *Magnetic Fluids.* Walter de Gruyter & Co., Berlin, Germany, 1996.

[35] Bishop, K. J. M.; Wilmer, C. E.; Soh, S.; Grzybowski, B. A. Nanoscale Forces and Their Uses in Self-Assembly. *Small*, 5:1600–1630, 2009.

[36] Sharifi, I.; Shokrollahi, H.; Amiri, S. Ferrite-based Magnetic Nanofluids Used in Hyperthermia Applications. *J. Magn. Magn. Mater.*, 324:903–915, 2012.

[37] Hunter, R. J. *Zeta Potential in Colloid Science: Principles and Applications.* Academic Press Inc. (London) Ltd., London, 1981.

[38] Cao, G. *Nanostructures & Nanomaterials: Synthesis, Properties & Applications.* Imperial College Press, London, 2007.

[39] Elimelech, M.; Gregory, J.; Jia, X.; Williams, R. A. *Particle Deposition & Aggregation: Measurement, Modelling and Simulation.* Colloid & Surface Engineering Series. Butterworth-Heinemann Ltd., Oxford, United Kingdom, 1995.

[40] Steed, J. W.; Atwood, J. L. *Supramolecular Chemistry.* John Wiley & Sons, Ltd., Chichester, United Kingdom, 2000.

[41] Hobza, P.; Zahradnik, R. *Intermolecular Complexes: The Role of van der Waals Systems in Physical Chemistry and in the Biodisciplines*, volume 52 of *Studies in Physical and Theoretical Chemistry.* Elsevier, Amsterdam, 1988.

[42] Napper, D. H. Steric Stabilization. *J. Colloid Interface Sci.*, 58:390–407, 1977.

[43] Shchukin, E. D.; Yaminsky, V. V. Thermodynamic Factors of the Sol-Gel Transition. 1. Reversible Coagulation of Organophilic and Hydrophilic Colloids. *Colloids Surf.*, 32:19–32, 1988.

[44] Jain, N.; Wang, Y.; Jones, S. K.; Hawkett, B. S.; Warr, G. G. Optimized Steric Stabilization of Aqueous Ferrofluids and Magnetic Nanoparticles. *Langmuir*, 26:4465–4472, 2010.

[45] Lourenco, C.; Teixeira, M.; Simoes, S.; Gaspar, R. Steric Stabilization of Nanoparticles: Size and Surface Properties. *Int. J. Pharm.*, 138:1–12, 1996.

[46] Feigin, R. I.; Napper, D. H. Depletion Stabilization and Depletion Flocculation. *J. Colloid Interface Sci.*, 75:525–541, 1980.

[47] Romero-Cano, M. S.; Martin-Rodriguez, A.; de las Nieves, F. J. Electrosteric Stabilization of Polymer Colloids with Different Functionality. *Langmuir*, 17:3505–3511, 2001.

[48] Lu, A.-H.; Salabas, E. L.; Schueth, F. Magnetic Nanoparticles: Synthesis, Protection, Functionalization, and Application. *Angew. Chem. Int. Ed.*, 46:1222–1244, 2007.

[49] Gubin, S. P.; Koksharov, Y. A.; Khomutov, G. B.; Yurkov, G. Y. Magnetic Nanoparticles: Preparation, Structure and Properties. *Russ. Chem. Rev.*, 74:489–520, 2005.

[50] Huczko, A. Template-based Synthesis of Nanomaterials. *Appl. Phys. A*, 70:365–376, 2000.

[51] Hyeon, T. Chemical Synthesis of Magnetic Nanoparticles. *Chem. Commun.*, pages 927–934, 2003.

[52] Tartaj, P.; del Puerto Morales, M.; Veintemillas-Verdaguer, S.; Gonzalez-Carreno, T.; Serna, C. J. The Preparation of Magnetic Nanoparticles for Applications in Biomedicine. *J. Phys. D: Appl. Phys.*, 36:R182–R197, 2003.

[53] Hao, R.; Xing, R.; Xu, Z.; Hou, Y.; Gao, S.; Sun, S. Synthesis, Functionalization, and Biomedical Applications of Multifunctional Magnetic Nanoparticles. *Adv. Mater.*, 22:2729–2742, 2010.

[54] Neuberger, T.; Schoepf, B.; Hofmann, H.; Hofmann, M.; von Rechenberg, B. Superparamagnetic Nanoparticles for Biomedical Applications: Possibilities and Limitations of a New Drug Delivery System. *J. Magn. Magn. Mater*, 293:483–496, 2005.

[55] Cao, G.; Liu, D. Template-based Synthesis of Nanorod, Nanowire, and Nanotube Arrays. *Adv. Colloid Interface Sci.*, 136:45–64, 2007.

[56] Martin, C. R. Nanomaterials - A Membrane-based Synthetic Approach. *Science*, 266:1961–1966, 1994.

[57] Whitney, T. M.; Searson, P. C.; Jiang, J. S.; Chien, C. L. Fabrication and Magnetic Properties of Arrays of Metallic Nanowires. *Science*, 261:1316–1319, 1993.

[58] Bicelli, L. P.; Bozzini, B.; Mele, C.; D'Urzo, L. A Review of Nanostructural Aspects of Metal Electrodeposition. *Int. J. Electrochem. Sci.*, 3:356–408, 2008.

[59] Puntes, V. F.; Krishnan, K. M.; Alivisatos, A. P. Colloidal Nanocrystal Shape and Size Control: The Case of Cobalt. *Science*, 291:2115–2117, 2001.

[60] Dumestre, F.; Chaudret, B.; Amiens, C.; Respaud, M.; Fejes, P.; Renaud, P.; Zurcher, P. Unprecedent Crystalline Super-Lattices of Monodisperse Cobalt Nanorods. *Angew. Chem.*, 42:5213–5216, 2003.

[61] Cordente, N.; Respaud, M.; Senocq, F.; Casanove, M.-J.; Amiens, C.; Chaudret, B. Synthesis and Magnetic Properties of Nickel Nanorods. *Nano Letters*, 1:565–568, 2001.

[62] Park, S.-J.; Kim, S.; Lee, S.; Khim, Z. G.; Char, K.; Hyeon, T. Synthesis and Magnetic Studies of Uniform Iron Nanorods and Nanospheres. *J. Am. Chem. Soc.*, 122:8581–8582, 2000.

[63] Shubayev, V. I.; Pisanic, T. R.; Jin, S. Magnetic Nanoparticles for Theragnostics. *Adv. Drug Delivery Rev.*, 61:467–477, 2009.

[64] Jain, K. K. Nanotechnology in Clinical Laboratory Diagnostics. *Clin. Chim. Acta.*, 358:37–54, 2005.

[65] Pankhurst, Q. A.; Connolly, J.; Jones, S. K.; Dobson, J. Applications of Magnetic Nanoparticles in Biomedicine. *J. Phys. D: Appl. Phys.*, 36:R167–R181, 2003.

[66] Gupta, A. K.; Gupta, M. Synthesis and Surface Engineering of Iron Oxide Nanoparticles for Biomedical Applications. *Biomaterials*, 26:3995–4021, 2005.

[67] Na, H. B.; Song, I. C.; Hyeon, T. Inorganic Nanoparticles for MRI Contrast Agents. *Adv. Mater.*, 21:2133–2148, 2009.

[68] Xiao, L.; Li, J.; Brougham, D. F.; Fox, E. K.; Feliu, N.; Bushmelev, A.; Schmidt, A.; Mertens, N.; Kiessling, F.; Valldor, M.; et al. Water-Soluble Superparamagnetic Magnetite Nanoparticles with Biocompatible Coating for Enhanced Magnetic Resonance Imaging. *ACS Nano*, 5:6315–6324, 2011.

[69] Liong, M.; Lu, J.; Kovochich, M.; Xia, T.; Ruehm, S. G.; Nel, A. E.; Tamanoi, F.; Zink, J. I. Multifunctional Inorganic Nanoparticles for Imaging, Targeting, and Drug Delivery. *ACS Nano*, 2:889–896, 2008.

[70] Gijs, M. A. M. Magnetic Bead Handling On-Chip: New Opportunities for Analytical Applications. *Microfluid. Nanofluid.*, 1:22–40, 2004.

[71] Lewin, M.; Carlesso, N.; Tung, C.-H.; Tang, X.-W.; Cory, D.; Scadden, D. T.; Weissleder, R. Tat Peptide-derivatized Magnetic Nanoparticles Allow in Vivo Tracking and Recovery of Progenitor Cells. *Nature Biotechnology*, 18:410–414, 2000.

[72] Barreto, J. A.; O'Malley, W.; Kubeil, M.; Graham, B.; Stephan, H.; Spiccia, L. Nanomaterials: Applications in Cancer Imaging and Therapy. *Adv. Mater.*, 23:H18–H40, 2011.

[73] Pankhurst, Q. A.; Thanh, N. K. T.; Jones, S. K.; Dobson, J. Progress in Applications of Magnetic Nanoparticles in Biomedicine. *J. Phys. D: Appl. Phys.*, 42:224001, 2009.

[74] Gleich, B.; Weizenecker, J. Tomographic Imaging Using the Nonlinear Response of Magnetic Particles. *Nature*, 435:1214–1217, 2005.

[75] Scherer, F.; Anton, M.; Schillinger, U.; Henke, J.; Bergemann, C.; Krueger, A.; Gaensbacher, B.; Plank, C. Magnetofection: Enhancing and Targeting Gene Delivery by Magnetic Force in Vitro and in Vivo. *Gene Therapy*, 9:102–109, 2002.

[76] Haun, J. B.; Yoon, T.-J.; Lee, H.; Weissleder, R. Magnetic Nanoparticle Biosensors. *Wiley Interdiscip. Rev. Nanomed.*, 2:291–304, 2010.

[77] Weddemann, A.; Albon, C.; Auge, A.; Wittbracht, F.; Hedwig, P.; Akemeier, D.; Rott, K.; Meissner, D.; Jutzi, P.; Huetten, A. How To Design Magneto-Based Total Analysis Systems for Biomedical Applications. *Biosens. Bioelectron.*, 26:1152–1163, 2010.

[78] Gao, J.; Gu, H.; Xu, B. Multifunctional Magnetic Nanoparticles: Design, Synthesis, and Biomedical Applications. *Acc. Chem. Res.*, 42:1097–1107, 2009.

[79] Simon de Dios, A.; Diaz-Garcia, M. E. Multifunctional Nanoparticles: Analytical Prospects. *Anal. Chim. Acta*, 666:1–22, 2010.

[80] Wang, S. X.; Li, G. Advances in Giant Magnetoresistance Biosensors with Magnetic Nanoparticle Tags: Review and Outlook. *IEEE Trans. Magn.*, 44:1687–1702, 2008.

[81] Llandro, J.; Palfreyman, J. J.; Ionescu, A.; Barnes, C. H. W. Magnetic Biosensor Technologies for Medical Applications: a Review. *Med. Biol. Eng. Comput.*, 48:977–998, 2010.

[82] Romanus, E.; Gross, C.; Koetitz, R.; Prass, S.; Lange, J.; Weber, P.; Weitschies, W. Monitoring of Biological Binding Reactions by Magneto-Optical Relaxation Measurements. *Magnetohydrodynamics*, 37:328–333, 2001.

[83] Cotton, A.; Mouton, H. New Optic Property (Magnetic Birefringence) of Some Non Colloidal Organic Liquids. *Comptes Rendus hebdomadaires des Seances de l'Academie des Sciences*, 145:229–230, 1907.

[84] van de Hulst, H. C. *Light Scattering by Small Particles*. Dover Publications, Inc., Mineola, NY, 1981.

[85] Mie, G. Articles on the Optical Characteristics of Turbid Tubes, Especially Colloidal Metal Solutions. *Ann. Phys.*, 25:377–445, 1908.

[86] Bohren, C. F.; Huffman, D. R. *Absorption and Scattering of Light by Small Particles*. Wiley-VCH, Weinheim, Germany, 2004.

[87] El-Sayed, M. A. Some Interesting Properties of Metals Confined in Time and Nanometer Space of Different Shapes. *Acc. Chem. Res.*, 34:257–264, 2001.

[88] Eustis, S.; El-Sayed, M. A. Why Gold Nanoparticles are More Precious Than Pretty Gold: Noble Metal Surface Plasmon Resonance and its Enhancement of the Radiative and Nonradiative Properties of Nanocrystals of Different Shapes. *Chem. Soc. Rev.*, 35:209–217, 2006.

[89] Willets, K. A.; van Duyne, R. P. Localized Surface Plasmon Resonance Spectroscopy and Sensing. *Annu. Rev. Phys. Chem.*, 58:267–297, 2007.

[90] Anker, J. N.; Hall, W. P.; Lyandres, O.; Shah, N. C.; Zhao, J.; van Duyne, R. P. Biosensing with Plasmonic Nanosensors. *Nat. Mater.*, 7:442–453, 2008.

[91] Greffet, J.-J. Introduction to Surface Plasmon Theory. In Enoch, S., Bonod, N., editor, *Plasmonics: From Basics to Advanced Topics*, Springer Series in Optical Sciences; 167, pages 105–148, Heidelberg, Germany, 2012. Springer.

[92] Aizpurua, J.; Hillenbrand, R. Localized Surface Plasmons: Basics and Applications in Field-Enhanced Spectroscopy. In Enoch, S., Bonod, N., editor, *Plasmonics: From Basics to Advanced Topics*, Springer Series in Optical Sciences; 167, pages 151–176, Heidelberg, Germany, 2012. Springer.

[93] Maystre, D. Localized Surface Plasmons: Basics and Applications in Field-Enhanced Spectroscopy. In Enoch, S., Bonod, N., editor, *Survey of Surface Plasmon Polariton History*, Springer Series in Optical Sciences; 167, pages 3–37, Heidelberg, Germany, 2012. Springer.

[94] Kreibig, U.; Vollmer, M. *Optical Properties of Metal Clusters*. Springer Series in Material Science. Springer, Berlin, 1995.

[95] Kelly, K. L.; Coronado, E.; Zhao, L. L.;Schatz, G. C. The Optical Properties of Metal Nanoparticles: The Influence of Size, Shape, and Dielectric Environment. *J Phys. Chem. B*, 107:668–677, 2003.

[96] Haes, A. J.; Haynes, C. L.; McFarland, A. D.; Schatz, G. C.; van Duyne, R. P.; Zou, S. Plasmonic Materials for Surface-Enhanced Sensing and Spectroscopy. *MRS Bull.*, 30:368–375, 2005.

[97] Klein, T.; Laptev, A.; Guenther., A.; Bender, P.; Tschoepe, A.; Birringer, R. Magnetic-Field-Dependent Optical Transmission of Nickel Nanorod Colloidal Dispersions. *J. Appl. Phys.*, 106:114301, 2009.

[98] Miller, M. M.; Lazarides, A. A. Sensitivity of Metal Nanoparticle Surface Plasmon Resonance to the Dielectric Environment. *J. Phys. Chem. B*, 109:21556–21565, 2005.

[99] Draine, B. T.; Flatau, P. J. Discrete-Dipole Approximation for Scattering Calculations. *J. Opt. Soc. Am. A*, 11:1491–1499, 1994.

[100] Purcell, E. M.; Pennypacker, C. R. Scattering and Absorption of Light by Nonspherical Dielectric Grains. *Astrophys. J.*, 186:705–714, 1973.

[101] Draine, B. T.; Flatau, P. J. *User Guide for the Discrete Dipole Approximation Code DDSCAT 6.1.* arXiv.org e-Print archive; http://arxiv.org/abs/astro-ph/0409262v2, arXiv:0409262v2, 2004.

[102] Draine, B. T.; Goodman, J. Beyond Clausius-Mosotti: Wave Propagation on a Polarizable Point Lattice and the Discrete Dipole Approximation. *Astrophys. J.*, 186:685–697, 1993.

[103] DeVoe, H. Optical Properties of Molecular Aggregates. I. Classical Model of Electronic Absorption and Refraction. *J. Chem. Phys.*, 41:393–400, 1964.

[104] DeVoe, H. Optical Properties of Molecular Aggregates. II. Classical Theory of the Refraction, Absorption, and Optical Activity of Solutions and Crystals. *J. Chem. Phys.*, 43:3199–3208, 1966.

[105] Draine, B. T. The Discrete Dipole Approximation and Its Application to Interstellar Graphite Grains. *Astrophys. J.*, 333:848–872, 1988.

[106] Jensen, T. R.; Schatz, G. C.; van Duyne, R. P. Nanosphere Lithography: Surface Plasmon Resonance Spectrum of a Periodic Array of Silver Nanoparticles by Ultraviolet-Visible Extinction Spectroscopy and Electrodynamic Modeling. *J. Phys. Chem. B*, 103:2394–2401, 1999.

[107] Draine, B. T. The Discrete Dipole Approximation for Light Scattering by Irregular Targets. In Mishchenko, M. I.; Hovenier, J. W.; Travis, L. D., editor, *Light Scattering by Nonspherical Particles: Theory, Measurements, and Applications*, pages 131–145, San Diego, CA, 2000. Academic Press.

[108] Szunerits, S.; Boukherroub, R. Sensing Using Localized Surface Plasmon Resonance Sensors. *Chem. Commun.*, 48:8999–9010, 2012.

[109] Hamamoto, K.; Micheletto, R.; Oyama, M.; Umar, A. A.; Kawai, S.; Kawakami, Y. An Original Planar Multireflection System for Sensing Using the Local Surface Plasmon Resonance of Gold Nanospheres. *J. Opt. A: Pure Appl. Opt.*, 8:268–271, 2006.

[110] Haes, A. J.; Haynes, van Duyne, R. P. A Nanoscale Optical Biosensor: Sensitivity and Selectivity of an Approach Based on the Localized Surface Plasmon Resonance Spectroscopy of Triangular Silver Nanoparticles. *J. Am. Chem. Soc.*, 124:10596–10604, 2002.

[111] Haes, A. J.; Hall, W. P.; Chang, L.; Klein, W. L.; van Duyne, R. P. A Localized Surface Plasmon Resonance Biosensor: First Steps toward an Assay for Alzheimer's Disease. *Nano Lett.*, 4:1029–1034, 2004.

[112] Song, H. D.; Choi, I.; Yang, Y. I.; Hong, S.; Lee, S.; Kang, T.; Yi, J. Picomolar Selective Detection of Mercuric Ion (Hg^{2+}) Using a Functionalized Single Plasmonic Gold Nanoparticle. *Nanotechnology*, 21:145501, 2010.

[113] Choi, Y.; Kang, T.; Lee, L. P. Plasmon Resonance Energy Transfer (PRET)-based Molecular Imaging of Cytochrome c in Living Cells. *Nano Lett.*, 9:85–90, 2009.

[114] Quinten, M.; Kreibig, U. Optical Properties of Aggregates of Small Metal Particles. *Surf. Sci.*, 172:557–577, 1986.

[115] Elghanian, R; Storhoff, J. J.; Mucic, R. C.; Letsinger, R. L.; Mirkin, C. A. Selective Colorimetric Detection of Polynucleotides Based on the Distance-Dependent Optical Properties of Gold Nanoparticles. *Science*, 277:1078–1081, 1997.

[116] Storhoff, J. J.; Lazarides, A. A.; Mucic, R. C.; Mirkin, C. A.; Letsinger, R. L.; Schatz, G. C. What Controls the Optical Properties of DNA-Linked Gold Nanoparticle Assemblies? *J. Am. Chem. Soc.*, 122:4640–4650, 2000.

[117] Englebienne, P. Use of Colloidal Gold Surface Plasmon Resonance Peak Shift to Infer Affinity Constants from the Interactions Between Protein Antigens and Antibodies Specific for Single or Multiple Epitopes. *Analyst*, 123:1599–1603, 1998.

[118] Yu, C.; Irudayaraj, J. Multiplex Biosensor Using Gold Nanorods. *Anal. Chem.*, 79:572–579, 2007.

[119] Wang, C.; Irudayaraj, J. Gold Nanorod Probes for the Detection of Multiple Pathogens. *Small*, 4:2204–2208, 2008.

[120] Kneipp, K.; Kneipp, H.; Iztkan, I.; Dasari, R. R.; Feld, M. S. Ultrasensitive Chemical Analysis by Raman Spectroscopy. *Chem. Rev.*, 99:2957–2975, 1999.

[121] Wang, H.; Brandl, D. W.; Le, F.; Nordlander, P.; Halas, N. J. Nanorice: A Hybrid Plasmonic Nanostructure. *Nano Lett.*, 6:827–832, 2006.

[122] Shliomis, M. I.; Raikher, Y. L. Experimental Investigations of Magnetic Fluids. *IEEE Trans. Magn.*, 16:237–250, 1980.

[123] Fannin, P. C.; Charles, S. W. The Study of a Ferrofluid Exhibiting Both Brownian and Néel Relaxation. *J. Phys. D: Appl. Phys.*, 22:187–191, 1989.

[124] Debye, P. J. W. *Polar Molecules.* The Chemical Catalog Company Inc., New York, 1929.

[125] Tirado, M. M.; Garcia de la Torre, J. Rotational Dynamics of Rigid, Symmetric Top Macromolecules. Application to Circular Cylinders. *J. Chem. Phys.*, 73:1986–1993, 1980.

[126] Coffey, W. T.; Cregg, P. J.; Kalmykov, Yu. P. On the Theory of Debye and Néel Relaxation of Single Domain Ferromagnetic Particles. *Adv. Chem. Phys.*, 83:263–464, 1993.

[127] Shliomis, M. I. Ferrohydrodynamics: Retrospectives and Issues. In Odenbach, S., editor, *Ferrofluids. Magnetically Controllable Fluids and Their Applications*, Lecture Notes in Physics; 594, pages 85–111, Berlin, 2002. Springer.

[128] Raikher, Y. L.; Shliomis, M. I. The Effective Field Method in the Orientational Kinetics of Magnetic Fluids and Liquid Crystals. In Coffey, W., editor, *Relaxation Phenomena in Condensed Matter*, Advances in Chemical Physics Series; 87, pages 595–751. John Wiley & Sons, Inc, 1994.

[129] Rosensweig, R. E. *Ferrohydrodynamics.* Cambridge University Press., Cambridge, 1985.

[130] Yoshida, T.; Enpuku, K.; Dieckhoff, J.; Ludwig, F. Magnetic Fluid Dynamics in a Rotating Magnetic Field. *J. Appl. Phys.*, 111:053901, 2012.

[131] Urban, C.; Schurtenberger, P. Characterization of Turbid Colloidal Suspensions Using Light Scattering Techniques Combined with Cross-Correlation Methods. *J. Colloid Interface Sci.*, 207:150–158, 1998.

[132] Khlebtsov, N.; Bogatyrev, V.; Dykman, L.; Khlebtsov, B.; Staroverov, S.; Shirokov, A.; Matora, L.; Khanadeev, V.; Pylaev, T.; Tsyganova, N.; Terentyuk, G. Analytical and Theranostic Applications of Gold Nanoparticles and Multifunctional Nanocomposites. *Theranostics*, 3:167–180, 2013.

[133] NanoSight Ltd. Minton Park, London Road, Amesbury, Wiltshire, SP4 7RT, UK. http://www.nanosight.com.

[134] Neville, F.; Pchelintsev, N. A.; Broderick, M. J. F.; Gibson, T.; Millner, P. A. Novel One-pot Synthesis and Characterization of Bioactive Thiol-silicate Nanoparticles for Biocatalytic and Biosensor Applications. *Nanotechnology*, 20:055612, 2009.

[135] Calo, A.; Sanmarti-Espinal, M.; Iavicoli, P.; Persuy, M.-A.; Pajot-Augy, E.; Gomila, G.; Samitier, J. Diffusion-controlled Deposition of Natural Nanovesicles Containing G-protein Coupled Receptors for Biosensing Platforms. *Soft Matter*, 8:11632, 2012.

[136] Wetz, F.; Soulantica, K.; Respaud, M.; Falqui, A.; Chaudret, B. Synthesis and Magnetic Properties of Co Nanorod Superlattices. *Mater. Sci. Eng., C*, 27:1162–1166, 2007.

[137] Braidy, N.; Purdy, G. R.; Botton, G. A. Equilibrium and Stability of Phase-Separating Au-Pt Nanoparticles. *Acta Mater.*, 56:5972–5983, 2008.

[138] Lin, C.-A. J.; Sperling, R. A., Li, J. K., Yang, T.-Y., Li, P.-Y., Zanella, M., Chang, W. H., Parak, W. J. Design of an Amphiphilic Polymer for Nanoparticle Coating and Functionalization. *Small*, 4:334–341, 2008.

[139] Pellegrino, T.; Manna, L.; Kudera, S.; Liedl, T.; Koktysh, D.; Rogach, A. L.; Keller, S.; Raedler, J.; Natile, G.; Parak, W. J. Hydrophobic Nanocrystals Coated with an Amphiphilic Polymer Shell: A General Route to Water Soluble Nanocrystals. *Nano Letters*, 4:703–707, 2004.

[140] Hermanson, G. T. *Bioconjugate Techniques*. Elsevier, London, 2008.

[141] Roche Pharma AG. Herceptin® 150mg Pulver zur Herstellung eines Infusionslösungskonzentrats, 2012. Gebrauchsinformation: Information für den Anwender.

[142] Guenther, A.; Bender, P.; Tschoepe, A.; Birringer, R. Rotational Diffusion of Magnetic Nickel Nanorods in Colloidal Dispersions. *J. Phys.: Condens. Matter*, 23:325103, 2011.

[143] Kuenstner, J. T.; Norris, K. H. Spectrophotometry of Human Hemoglobin in the Near Infrared Region from 1000 to 2500 nm. *J. Near Infrared Spectrosc.*, 2:59–65, 1994.

[144] Roggan, A.; Friebel, M.; Doerschel, K.; Hahn, A.; Mueller, G. Optical Properties of Circulating Human Blood in the Wavelength Range 400-2500 nm. *J. Biomed. Opt.*, 4:36–46, 1999.

[145] Prime, K. L.; Whitesides, G. M. Self-Assembled Organic Monolayers: Model Systems for Studying Adsorption of Proteins at Surfaces. *Science*, 252:1164–1167, 1991.

[146] Liu, L.-F.; Zhou, W.-Y.; Xie, S.-S.; Albrecht, O.; Nielsch, K. Microstructure and Temperature-dependent Magnetic Properties of Co/Pt Multilayered Nanowires. *Chem. Phys. Lett.*, 466:165–169, 2008.

[147] Vega, V.; Boehnert, T.; Martens, S.; Waleczek, M.; Montero-Moreno, J. M.; Goerlitz, D.; Prida, V. M.; Nielsch, K. Tuning the Magnetic Anisotropy of Co-Ni Nanowires: Comparison between Single Nanowires and Nanowire Arrays in Hard-anodic Aluminum Oxide Membranes. *Nanotechnology*, 23:465709, 2012.

[148] Prida, V. M.; Garcia, J.; Iglesias, L.; Vega, V.; Goerlitz, D.; Nielsch, K.; Diaz Barriga-Castro, E.; Mendoza-Resendez, R.; Ponce, A.; Luna, C. Electroplating and Magnetostructural Characterization of Multisegmented $Co_{54}Ni_{46}/Co_{85}Ni_{15}$ Nanowires from Single Electrochemical Bath in Anodic Alumina Templates. *Nanoscale Res. Lett.*, 8:263, 2013.

[149] Wetz, F.; Soulantica, K.; Falqui, A.; Respaud, M.; Snoeck; Chaudret, B. Hybrid Co-Au Nanorods: Controlling Au Nucleation and Location. *Angew. Chem. Int. Ed.*, 46:7079–7081, 2007.

[150] Zierold, R.; Wu, Z.; Biskupek, J.; Kaiser, U.; Bachmann, J.; Krill, C. E.; Nielsch, K. Magnetic, Multilayered Nanotubes of Low Aspect Ratios for Liquid Suspensions. *Adv. Funct. Mater.*, 21:226–232, 2011.

[151] Soulantica, K.; Wetz, F.; Maynadie, J.; Falqui, A.; Tan, R. P.; Blon, T.; Chaudret, B.; Respaud, M. Magnetism of Single-Crystalline Co Nanorods. *Appl. Phys. Lett.*, 95:152504, 2009.

[152] Peters, T. Serum Albumin. *Adv. Protein Chem.*, 37:161–245, 1985.

[153] Payne, B. P.; Biesinger, M. C.; McIntyre, N. S. The Study of Polycrystalline Nickel Metal Oxidation by Water Vapour. *J. Electron Spectrosc. Rel. Phenom.*, 175:55–65, 2009.

[154] Kramer, H.; Graf, C.; Hagenbuechle, M.; Johner, C.; Schwind, P.; Weber, R. Electro-Optic Effects of Aqueous fd-Virus Suspensions at Very Low Ionic Strength. *J. Phys. II France*, 4:1061–1074, 1994.

[155] Ohshima, H. Henry's Function for Electrophoresis of a Cylindrical Colloidal Particle. *J. Colloid Interface Sci.*, 180:299–301, 1996.

[156] Henry, D. C. The Cataphoresis of Suspended Particles. Part I. The Equation of Cataphoresis. *Proc. R. Soc. Lond. A*, 133:106–129, 1931.

[157] van der Drift, W. P. J. T.; de Keizer, A.; Overbeek, J. Th. G. Electrophoretic Mobility of a Cylinder with High Surface Charge Density. *J. Colloid Interface Sci.*, 71:67–78, 1979.

[158] de Keizer, A.; van der Drift, W. P. J. T.; Overbeek, J. Th. G. Electrophoresis of Randomly Oriented Cylindrical Particles. *Biophys. Chem.*, 3:107–108, 1975.

[159] Mahmood, T.; Saddique, M. T.; Naeem, A.; Westerhoff, P.; Mustafa, P.; Alum, A. Comparison of Different Methods for the Point of Zero Charge Determination of NiO. *Ind. Eng. Chem. Res.*, 50:10017–10023, 2011.

[160] Ohshima, H. Surface Charge Density/Surface Potential Relationship for a Cylindrical Particle in an Electrolyte Solution. *J. Colloid Interface Sci.*, 200:291–297, 1998.

[161] Salis, A.; Bostroem, M.; Medda, L.; Cugia, F.; Barse, B.; Parsons, D. F.; Ninham, B. W.; Monduzzi, M. Measurements and Theoretical Interpretation of Points of Zero Charge/Potential of BSA Protein. *Langmuir*, 27:11597–11604, 2011.

[162] Fan, C.Y.; Kurabayashi, K.; Meyhoefer, E.;. Protein Pattern Assembly by Active Control of a Triblock Copolymer Monolayer. *Nano Letters*, 6:2763–2767, 2006.

[163] Ombelli, M.; Costello, L.; Postle, C.; Anantharaman, V.; Meng, Q. C.; Composto, R. J.; Eckmann, D. M. Competitive Protein Adsorption on Polysaccharide and Hyaluronate Modified Surfaces. *Biofouling*, 27:505–518, 2011.

[164] Bartell, L. S. On the Length of the Carbon-Carbon Single Bond. *J. Am. Chem. Soc.*, 81:3497–3498, 1959.

[165] Mathejczyk, J. E. Innovative NIR Fluorescent Probes for an Improved Tumor Detection in vivo. Doctoral Thesis at the Georg-August University Goettingen, 2011.

[166] Human HER-2, Recombinant Protein. eBioscience datasheet. Cat. No. BMS362.

[167] Sarma; V. R.; Silverton, E. W.; Davies, D. R.; Terry, W. D. The Three-Dimensional Structure at 6A Resolution of a Human γG1 Immunoglobulin Molecule. *J. Biol. Chem.*, 246:3753–3759, 1971.

[168] Jung, Y.; Jeong, J. Y.; Chung, B. H. Recent Advances in Immobilization Methods of Antibodies on Solid Supports. *Analyst*, 133:697–701, 2008.

[169] Ashish; Solanki, A. K.; Boone, C. D.; Krueger, J. K. Global Structure of HIV-1 Neutralizing Antibody IgG1 b12 is Asymmetric. *Biochem. Biophys. Res. Commun.*, 391:947–951, 2010.

[170] Bjoerhall, K.; Miliotis, T.; Davidsson, P. Comparison of Different Depletion Strategies for Improved Resolution in Proteomic Analysis of Human Serum Samples. *Proteomics*, 5:307–317, 2005.

[171] Kusnezow, W.; Pulli, T.; Witt, O.; Hoheisel, J. D. Solid Supports for Protein Microarrays and Related Devices. In Schena, M., editor, *Protein Microarrays*, pages 247–283, Sudbury, MA, 2005. Jones and Bartlett Publishers.

[172] Zhang, N.; Liu, L.; Dumitru, C. D.; Cummings, N. R. H.; Cukan, M.; Jiang, Y.; Li, Y.; Li, F.; Mitchell, T.; Mallem, M. R.; Ou, Y.; Patel, R. N.; Vo, K.; Wang, H.; Burnina, I.; Choi, B.-K.; Huber, H.; Stadheim, T. A.; Zha, D. Glycoengineered Pichia Produced Anti-HER2 is Comparable to Trastuzumab in Preclinical Study. *MABS*, 3:289–298, 2011.

[173] Dieckhoff, J. Messaufbau zur Untersuchung magnetischer Nanopartikel im rotierenden Magnetfeld. Diploma Thesis at the TU Braunschweig, 2011.

[174] Yang, Z.; Wang, G.; Liu, W. Analytical Calculation of the Self-Resonant Frequency of Biomedical Telemetry Coils. In *Proceedings of the 28th IEEE EMBS Annual International Conference*, pages 5880–5883, 2006.

[175] Reich, D. H.; Tanase, M.; Hultgren, A; Bauer, L. A.; Chen, C. S.; Meyer, G. J. Biological Applications of Multifunctional Magnetic Nanowires. *J. Appl. Phys.*, 93:7275–7280, 2003.

Publications

- Schrittwieser, S.; Schotter, J.; Maier, T.; Bruck, R.; Muellner, P.; Kataeva, N.; Soulantika, K.; Ludwig, F.; Huetten, A.; Brueckl, H. Homogeneous Biosensor Based on Optical Detection of the Rotational Dynamics of Anisotropic Nanoparticles. *Procedia Eng.* 5:1107-1110, 2010.

- Schrittwieser, S.; Ludwig, F.; Dieckhoff, J.; Soulantica, K.; Viau, G.; Lacroix, L.-M.; Lentijo, S. M.; Boubekri, R.; Maynadié, J.; Huetten, A.; Brueckl, H.; Schotter, J. Modeling and Development of a Biosensor Based on Optical Relaxation Measurements of Hybrid Nanoparticles. *ACS Nano* 6:791-801, 2012.

- Schrittwieser, S.; Ludwig, F.; Dieckhoff, J.; Tschoepe, A.; Guenther, A.; Richter, M.; Huetten, A.; Brueckl, H.; Schotter, J. Direct Protein Detection in the Sample Solution by Monitoring Rotational Dynamics of Nickel Nanorods *Small* 10:407-411, 2014.

Awards

- Poster Prize awarded by the Royal Sociey of Chemistry
  NanoBioTech Montreux 2009, Montreux, Switzerland
  November 16th-18th, 2009
  Development of a Biosensor Based on Optical Relaxation Measurements of Hybrid Nanoparticles

- Poster Prize (1^{st} place)
  December 2nd-3rd, 2010
  NANOSENS 2010, Vienna, Austria
  Optical Monitoring of Rotational Dynamics of Anisotropic Nanoparticles for Homogeneous Biosensing

- Poster Prize awarded by the Erwin Schrödinger Society (1^{st} place)
  March 13th-15th, 2013
  BioNanoMed 2013, Krems, Austria
  Homogeneous Biosensor Protein Detection by Monitoring Changes in the Rotational Dynamics of Nickel Nanorods

Participation in International Conferences

Talks

- September 5th-8th, 2010
  Eurosensors XXIV 2010, Linz, Austria
  Homogeneous Biosensor Based on Optical Detection of the Rotational Dynamics of Anisotropic Nanoparticles

- March 13th-18th, 2011
  DPG Spring Meeting Dresden 2011, Dresden, Germany
  Optical Detection of the Rotational Dynamics of Anisotropic Magnetic Nanoparticles

- September 27th-30th, 2011
  Biomedizinische Technik 2011, Freiburg, Germany
  Optical Detection of Nanoparticle Rotational Dynamics for Application in Homogeneous Biosensing

- September 28th-30th, 2011
  11th German Ferrofluid Workshop, Benediktbeuren, Germany
  Optically Detected Hydrodynamic Properties of Anisotropic Magnetic Nanoparticles for Real Time Biosensing
  held by Jörg Schotter

- March 1st-2nd, 2012
  BioNanoMed 2012, Krems, Austria
  Optical Detection of Nanoparticle Rotational Dynamics as a New Approach to Homogeneous Biosensing

- May 15th-18th, 2012
  Biosensors 2012, Cancun, Mexico
  Optically Detected Rotational Dynamics of Magnetic Nanoparticles for Homogeneous Immunodiagnostics

- September 26th-28th, 2012
  12th German Ferrofluid Workshop, Benediktbeuren, Germany
  Optical Detection of the Rotational Dynamics of Anisotropic Magnetic Nickel Nanorods

- March 10th-15th, 2013
  DPG Spring Meeting Regensburg 2013, Regensburg, Germany
  Direct Protein Detection in the Sample Solution by Monitoring Rotational Dynamics of Nickel Nanorods held by Jörg Schotter

- May 12th-15th, 2013
  3rd International Conference on Bio-Sensing Technology 2013, Sitges, Spain

Direct Protein Detection in the Sample Solution by Monitoring Rotational Dynamics of Nickel Nanorods held by Jörg Schotter

Poster Presentations

- September 29th-30th, 2008
  NANOSENS 2008, Vienna, Austria
  Detection of Biomolecules by Optical Relaxation Measurements of Hybrid Nanoparticles

- January 26th-27th, 2009
  BioNanoMed 2009, Krems, Austria
  Detection of Biomolecules by Optical Relaxation Measurements of Hybrid Nanoparticles

- July 1st, 2009
  ARGE Sensorik PhD-Summit, Vienna University of Technology, Vienna, Austria
  Biomolecular Detection by Optical Relaxation Measurements of Hybrid Nanoparticles

- November 16th-18th, 2009
  NanoBioTech Montreux 2009, Montreux, Switzerland
  Development of a Biosensor Based on Optical Relaxation Measurements of Hybrid Nanoparticles

- May 25th-29th, 2010
  8th International Conference on the Scientific and Clinical Applications of Magnetic Carriers, Rostock, Germany
  Optical Relaxation Measurements of Novel Hybrid Nanoparticles for Homogeneous Biosensing

- November 15th-17th, 2010
  NanoBioTech Montreux 2010, Montreux, Switzerland
  Optical Detection of the Rotational Dynamics of Anisotropic Hybrid Nanoparticles for Homogeneous Biosensing

- December 2nd-3rd, 2010
  NANOSENS 2010, Vienna, Austria
  Optical Monitoring of Rotational Dynamics of Anisotropic Nanoparticles for Homogeneous Biosensing

- March 3rd-6th, 2013
  NAMDIATREAM Winter School, Villars-sur-Ollon, Switzerland
  Homogeneous Biosensor Protein Detection by Monitoring Changes in the Rotational Dynamics of Nickel Nanorods

- March 13th-15th, 2013
  BioNanoMed 2013, Krems, Austria
  Homogeneous Biosensor Protein Detection by Monitoring Changes in the Rotational Dynamics of Nickel Nanorods

- May 12th-15th, 2013
  3rd International Conference on Bio-Sensing Technology 2013, Sitges, Spain
  Direct Protein Detection in the Sample Solution by Monitoring Rotational Dynamics of Nickel Nanorods